FINAL REPORT

Assessing Kuujjuaq's (Nunavik, Canada) deep geothermal energy potential

Core analysis, thermal properties characterization and surface heat flux estimation of a 234 m deep geothermal exploration well

Mafalda M. Miranda[1]

Jasmin Raymond[1]

[1]**Institut national de la recherche scientifique (INRS), Centre Eau Terre Environnement**

Rapport de recherche R2109

Prepared for the account of:

CanmetENERGY-Ottawa

Natural Resources Canada | Ressources naturelles Canada

Canada

CanmetENERGY / CanmetÉNERGIE

April 29, 2022

INRS Institut national de la recherche scientifique

ISBN : 978-2-89146-973-9 (version électronique)

Dépôt légal - Bibliothèque et Archives nationales du Québec, 2023
Dépôt légal - Bibliothèque et Archives Canada, 2023

ACKNOWLEDGEMENTS

This report was written and prepared by the Institut national de la recherche scientifique (INRS). It was produced with financial support of Natural Resources Canada (NRCan). Andrew Wigston, of NRCan's CanmetENERGY-Ottawa laboratory provided input and assistance. The authors are also grateful to Jason Aitchison (Kuujjuamiut Inc) and Charlie Watt (Avataa Explorations Logistics Inc) for their help with core logistics (drilling, transportation and storage). Acknowledgements are extended to Anne-Aurélie Sapin (Geological Survey of Canada) and Isabelle Lafrance (Ministère de l'Énergie et des Ressources naturelles) for the helpful discussions that aided to better identify and define the lithologies and geological units. Rénald Gauthier from the Fédération des coopératives du Nouveau-Québec is also acknowledged for insights that helped oriented this project.

FOREWORD

Kuujjuaq, the regional capital of Nunavik (Quebec, Canada) and located above the 55 ºparallel, is one of the hundreds Canadian off-grid communities solely relying on diesel for electricity and space heating. Deep geothermal energy systems, such as Enhanced Geothermal Systems (EGS), can be a game changer to decrease this excessive diesel consumption in the Canadian off-grid, remote and northern communities.

However, the imperfect knowledge of the subsurface geology, thermal properties of the deep-seated rocks and surface heat flux motivated by the lack of deep geothermal exploration wells nearby the remote communities impose important constraints in assessing the geothermal energy potential at a community-scale and the technical feasibility of deep geothermal energy systems. Therefore, advancing geothermal exploration in remote northern regions is an important step to be taken.

In this context, the present study reports results obtained from the core analysis, thermal properties characterization and surface heat flux estimation of a 234 m deep geothermal exploration well drilled in Kuujjuaq, which is the deepest well drilled in this community so far. Significant scientific contributions were made to improve the knowledge of the subsurface lithology, thermal properties of the geological materials and surface heat flux estimation and, in this way, move towards a more accurate assessment of Kuujjuaq's deep geothermal energy potential.

EXECUTIVE SUMMARY

A well with 234 m of core recovered was drilled near Kuujjuaq's (Nunavik, Canada) Forum building as part of the Kuujjuaq Clean Energy Plan to install a 150 m deep vertical closed-loop ground source heat pump system. This study thus aimed at analyzing the well core in the scope of deep geothermal resource assessment and was divided into three main tasks:

1) **Geological core logging** – Identification and description of the lithologies and of the natural and induced fractures and qualitative interpretation of the stress regime. Estimation of core recovery parameters (total core recovery, solid core recovery and rock quality designation) to describe the quality of the core recovered from the borehole.

2) **Laboratory thermal analyses** – Thermal conductivity evaluation with the Thermal Conductivity Scanning (TCS) technique.

3) **Surface heat flux** – Correction of a temperature profile measured by Géotherma solutions inc. for drilling- and paleoclimate-induced thermal disturbances and estimation of terrestrial heat flux. A standard analytical approach was followed, and a Monte Carlo-based sensitivity analysis was undertaken to deal with paleoclimate uncertainty.

The geological core logging revealed that the paragneiss of False Suite is the main lithological unit. Minor mafic and felsic intrusions were also detected. The mafic intrusions correspond to gabbro/diorite of Kaslac Complex and Ralleau Suite. The felsic intrusions are mostly tonalite/granite/granitoids of Aveneau and Dancelou suites and Kaslac Complex. Natural and non-natural fractures were distinguished. Within the natural fractures, inclined fractures are predominant followed by horizontal fractures. Some vertical fractures were also observed. Within the non-natural fractures, coring- and handling-induced fractures prevailed compared to drilling-induced fractures. The natural fractures observed suggest a reverse/strike-slip stress regime typical for the Canadian Shield. The estimated density is 0.96 natural fractures per meter with a random distribution and clustering. The calculated total core recovery is greater than 90%, the solid core recovery is about 90% and the rock quality designation is 80% indicating good rock quality.

A total of 15 representative core samples (8 paragneiss samples and 7 gabbro/diorite samples) were selected for the laboratory thermal analyses. The thermal conductivity of the paragneiss samples was found to vary between 2.5 and 2.9 W m^{-1} K^{-1}. Per contra, the diorite/gabbro samples have lower thermal conductivity values, evaluated to range between 1.9 and 2.4 W m^{-1} K^{-1}. Thermal diffusivity analyses and volumetric heat capacity estimates were planned but the diameter of the core samples (about 45 mm) is smaller than the minimum diameter recommended by the TCS manufacturer (60 mm). This makes thermal diffusivity results unreliable and therefore only thermal conductivity could be evaluated. Laboratory analyses to obtain the concentration of radiogenic elements (U, Th and K) have been planned and are still underway.

The geothermal gradient corrected for thermal disturbances due to drilling- and paleoclimates was estimated to range between 20.4 and 21.8 ºC km^{-1} (50% probability interval), with a most probable value of 20.9 ºC km^{-1}. The extreme and least probable geothermal gradient values are 19.3 and 23.3 ºC km^{-1}. Thus, the surface heat flux was evaluated varying between 55.2 and 59.0 mW m^{-2} (50% probability

interval), with a most probable value of 57.2 mW m^{-2}. The extreme and least probable surface heat flux values are 49.5 and 65.5 mW m^{-2}.

The information gathered in this work is essential to reduce some of the geological uncertainties identified by previous studies and, hence, moving towards a more accurate assessment of Kuujjuaq's deep geothermal energy source potential. In fact, the new geothermal gradient and heat flux assessments carried out indicate favourable geothermal development for direct use applications (i.e., space heating) at depths of 3-4 km. Electricity generation may be possible at depths greater than 7 km. Bearing these thrilling results in mind, if the community of Kuujjuaq decides to proceed with further deep geothermal exploration, the next logical step will be the drilling of a 1000 m deep exploratory borehole. This borehole should aim at collecting further information on the thermal and hydrogeological subsurface state and properties of the deep-seated rocks but also on the structural and stress regime prevailing at depth.

Table of Contents

List of figures

List of tables

1. INTRODUCTION

Nunavik is a region in the Province of Quebec located above the 55° parallel and home to 14 Inuit communities spread along its coast (**Figure 1.1**). These communities are disconnected from the provincial grid, depending on autonomous diesel-based energy systems. In fact, the 14 Inuit communities of Nunavik rely exclusively on diesel for electricity and space heating. Electricity in each of these communities is supplied by a diesel generator operated by Hydro-Quebec – Quebec public energy company. Due to the low efficiency and high generation costs, space heating and domestic hot water are provided directly by oil furnaces.

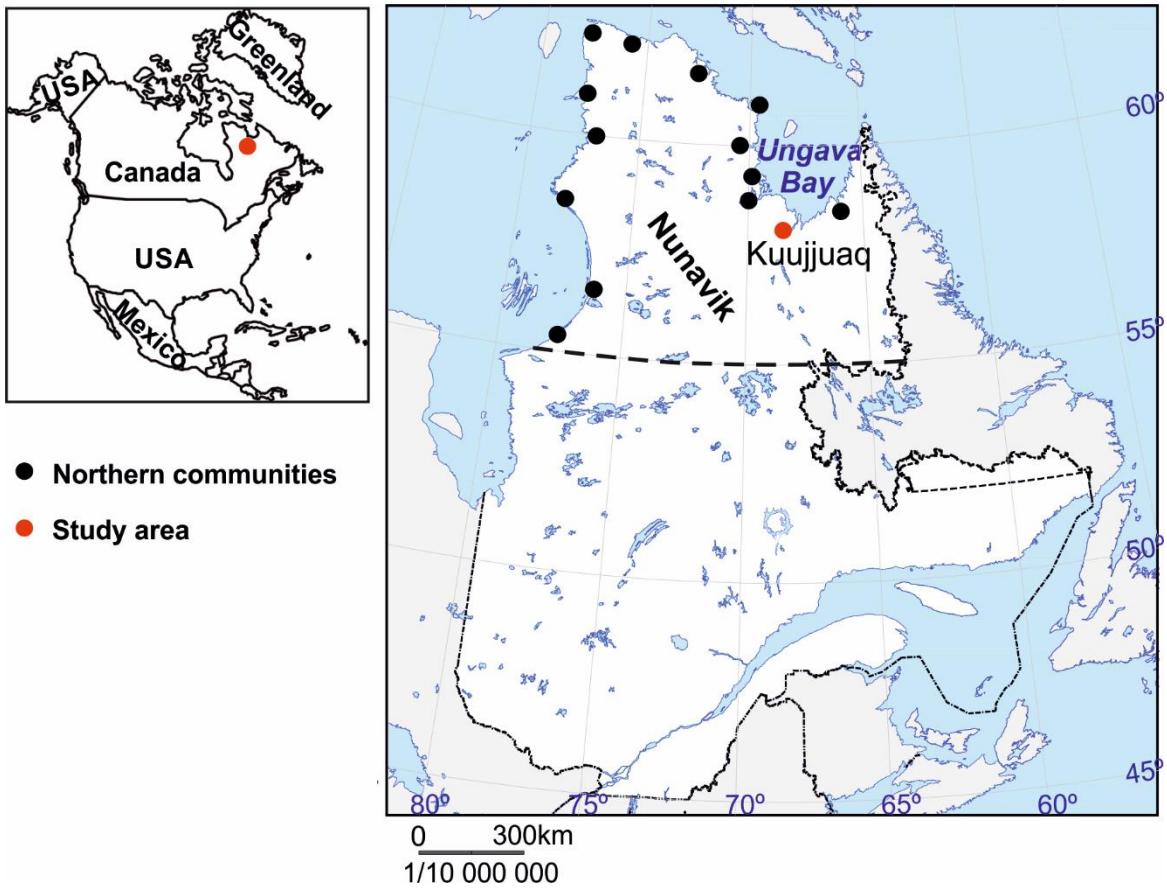

Figure 1.1. Geographical location of the remote communities in Nunavik (Quebec, Canada).

This energetic framework entails several socio-economic problems namely related with energy cost, diesel consumption, energy insecurity and adverse environmental impacts. The price of fuel oil in 2018 was CAD 2.03$/L, subsidized by the local government to CAD 1.63$/L (Makivik Corporation, 2018). The electricity rate structure for the households is twofold in Nunavik: the first tier (up to 40 kWh) is identical to the rate in southern Quebec (6 ¢/kWh), but the second tier increases to near 42 ¢/kWh (Rate DN; Hydro Québec, 2021). However, for businesses, Hydro-Québec charges the real production cost to the company, meaning an energy cost four times higher than in southern Quebec and thus a barrier to creating private businesses in a region where economic development rate is very low (Rodon et al., 2021). Data for 2013 indicate a total electricity cost in Nunavik ranging from 65 ¢/kWh in Salluit to 132.4 ¢/kWh in Ivujivik (Karanasios and Parker, 2016). The heating energy cost, per contra, has been evaluated

as 19 ¢/kWh (Giordano et al., 2018). For comparison purposes, in southern Quebec, space heating is provided by electric systems at about 8 ¢/kWh.

Nunavik has a harsh climate, experiencing annual average temperature of -6 ºC and an annual average of 8 000 heating degree days below 18 ºC. Heating degree days are a measure of how much heating is required in a year. 18 °C is the temperature below which heating is required to maintain a comfortable temperature inside buildings. A place that gets many days with average temperatures below 18 °C or that gets mean temperatures much below 18 °C will require a relatively large amount of energy to heat buildings for comfort and safety (Climate Atlas of Canada, 2019). Although the residential dwellings are built to meet certain regulatory standards of insulation, the harsh climate results in high building heating requirements. The annual average fuel consumption for electricity is about 25 million liters with additional 28 million liters for space heating purposes (for 2008; KRG and Makivik Corporation, 2010). In Kuujjuaq, for example, the annual average fuel consumption of a typical residential dwelling has been estimated about 3 100 to 8 180 liters (Yan et al., 2019; Gunawan et al., 2020). This represents around 28 to 32 L m^{-2} with respect to the floor area. Yan et al. (2019) considered a heated floor area of 110.9 m^2 while Gunawan et al. (2020) assumed 252 m^2. Such floor area difference also impacts the annual heating energy demand, which for Yan et al. (2019) is 21.6 MWh and for Gunawan et al. (2020) is 71 MWh.

There are currently about 973 residential dwellings in Kuujjuaq (Statistics Canada, 2021), indicating a total yearly consumption of 3 to 8 million liters of oil for space heating, that is expected to increase as the population grows. Since the communities in Nunavik are off grid and relying on only one source of energy, the energy security is very low. In case of a malfunction, the community would be threatened as what happened in Pangnirtung (Rodon et al., 2021). The exclusive reliance on fossil fuels has negative environmental impacts namely related to the greenhouse gas emissions associated to electricity generation and space heating, but also connected with the increasing risk of spills during diesel transportation and long-term storage.

Thus, this combination of high fuel consumption and cost, high electricity and building heating requirements, increasing demand and adverse environmental impact of fossil fuel combustion calls for the development of new approaches, specifically via renewable energy sources to supply clean, locally generated, and reliable energy in these off-grid communities. One of such options is geothermal energy sources[1] harvested by deep unconventional geothermal systems.

A first step to assess the deep geothermal potential of a region is related with the evaluation of the surface heat flux. Such estimates are dependent on the thermal conductivity of the geological materials and of the geothermal gradient. The latter is measured in deeper than 200 m slim-holes or geothermal exploration wells by continuous temperature logging or bottom-hole temperature measurements. However, temperature logs measured after drilling are affected by drilling-induced thermal disturbances that need to be corrected. Furthermore, temperature logs are often affected by climate surface temperature changes with larger amplitudes and duration than daily or annual cycles. Examples of climate events strongly affecting temperature logs are the Quaternary glacial periods and Holocene climate events such as the Holocene Thermal Maximum, the Roman and Medieval warm periods, the Little Ice Age, the pre-Industrial and Industrial Revolution and the nowadays global warming. Thus, paleoclimate corrections need to be undertaken to obtain an undisturbed temperature log for heat flux assessments. In fact,

[1] Geothermal energy source – *"thermal energy contained in a body of rock, sediment and/or soil, including any contained fluids, which is available for extraction and conversion into energy products. (...) The Geothermal Energy Source results from any influx to outflux from or internal generation of energy within the system over a specified period of time"* (UNECE, 2016).

neglecting the effects of paleoclimate can lead to an underestimation of heat flux by 10% or more (Jessop, 1971).

Thermal conductivity of geological materials is often evaluated in the laboratory using samples from the recovered core. Laboratory methods to infer thermal conductivity from drill core samples are divided into two categories – transient and steady state methods. Transient methods encompass the optical scanning technique (e.g., Popov et al., 2016), the transient plane source technique (e.g., Miranda, 2014) and the transient line source technique (e.g., Popov et al., 2016). Steady state methods include the divided bar technique (e.g., Popov et al., 2016) and the guarded heat flow meter technique (e.g., Miranda et al., 2020a). The ISRM suggested methods to evaluate thermal properties are the optical scanning technique, the divided bar technique and the line-source technique (Popov et al., 2016).

Once thermal conductivity and geothermal gradient are evaluated, the terrestrial heat flux can be estimated. Several methods have been proposed in the literature to combine the temperature and thermal conductivity data to give the heat flux (Jessop, 1990). Essentially, surface heat flux can be analytically estimated based on Fourier's law (**Eq. 1.1**) or based on the analytical solution of the heat conduction equation (**Eq. 1.2**):

$$q_0 = -\lambda \times \nabla T \quad (\mathbf{1.1})$$

$$q_0 = \nabla T \times \lambda + \frac{RHP}{2} \quad (\mathbf{1.2})$$

where q_0 (W m^{-2}) is the surface heat flux, λ (W m^{-1} K^{-1}) is thermal conductivity, ∇T (°C km^{-1}) is the geothermal gradient and *RHP* (W m^{-3}) is the radiogenic heat production. This last parameter is related with the concentration of heat-producing radiogenic elements (i.e., uranium, thorium and potassium) in the geological materials which can be evaluated in the laboratory by mass or gamma-ray spectrometry techniques (e.g., Miranda et al., 2020a).

Bearing in mind the importance of surface heat flux for assessing the deep geothermal potential of a site, this report aims at characterizing the core pieces recovered from the well drilled in Kuujjuaq in terms of lithology, evaluating the thermal conductivity of representative core samples and estimating the surface heat flux after carrying out corrections for drilling- and paleoclimate-induced thermal disturbances.

This report is organized in the following manner: section 2 presents a description of the well, namely who, where and when the well was drilled and how much energy is expected to be extracted from the surface by the shallow geothermal systems. Section 3 describes the geology of Kuujjuaq, and section 4 describes the core pieces in terms of lithology, geological units and fractures (induced and natural). This helped to define the representative samples for the thermal conductivity analyzes that are present in section 5. A detailed description of the laboratory technique and of the experimental setup used is provided together with the results obtained and a discussion of these results. Section 6 presents the surface heat flux estimates. First, it is discussed the geothermal gradient correction for the drilling-induced thermal disturbances and for paleoclimate disturbances and then the assessment of the surface heat flux taking into account the thermal conductivity and corrected geothermal gradient previously estimated. This report finishes with a general discussion of the results obtained and how they can help to better assess the deep geothermal potential of Kuujjuaq (section 7).

2. FORUM WELL

A well with 234 m depth (hereafter defined as Forum well) was drilled near the community's Forum building (**Figure 2.1**). The Forum well was drilled as part of a drilling training class supported by Avataa Explorations Logistiscs Inc. A 150 m deep vertical closed-loop ground source heat pump system will be installed in the Forum well as part of the Kuujjuaq Clean Energy Plan to offset the diesel consumption in this community building. The Kuujjuaq Forum was inaugurated in 1992 and is operated by Kuujjuamiut Inc and features three main facilities that continue to operate on a daily schedule, an ice arena, gymnasium, and fitness center. The main heating fuel used in this building is diesel and the shallow geothermal system is expected to extract 9.4 ± 0.8 MWh of energy annually (Géotherma solutions inc, 2022).

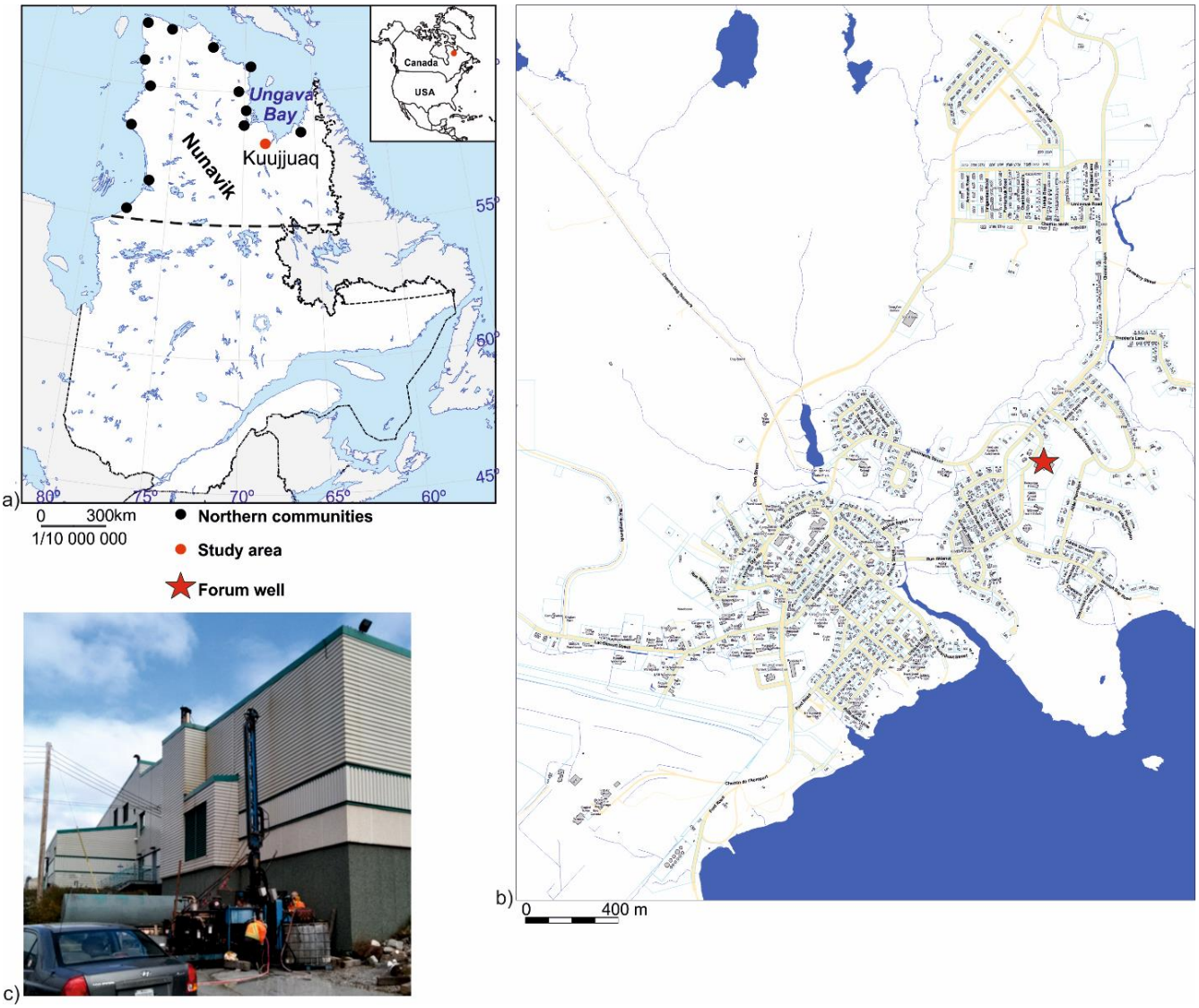

Figure 2.1. a) Geographical location of Kuujjuaq, b) Kuujjuaq community map (KRG, 2021) and location of Forum well and c) drilling site.

The drilling started September 15, 2021, and finished September 26, 2021. Despite the well has a total length of 240 m, only 234 m of core was recovered. For this reason, the well was assumed to be 234 m

deep. The first 6 m of the well are HQ size, and the rest is NQ. The casing is 6 m. **Table 2.1** contains information of the metres drilled per day. An average of about 25 m per day were drilled in a total of 99 hours of drilling.

Table 2.1. Drilling report of the Forum well.

Production (drilling days)	From (m)	To (m)	Total (m)	Comments
September 15, 2021	0	6	6	Casing HQ
September 16, 2021	6	21	15	NQ
September 17, 2021	21	42	21	NQ
September 18, 2021	42	72	30	NQ
September 20, 2021	72	99	27	NQ
September 21, 2021	99	126	27	NQ
September 22, 2021	126	153	27	NQ
September 23, 2021	153	183	30	NQ
September 24, 2021	183	207	24	NQ
September 25, 2021	207	225	18	NQ
September 26, 2021	225	240	15	NQ

3. GEOLOGY OVERVIEW OF KUUJJUAQ

The community of Kuujjuaq is located on the Canadian Shield, more specifically on the northern section of the Baleine lithotectonic domain of the Southeastern Churchill Province. Five main geological units have been identified in Kuujjuaq area, the Kaslac Complex, the False Suite, the Dancelou Suite, the Aveneau Suite and the Ralleau Suite (**Figure 3.1**; MERN, 2020). Each of these units is described in the following subsections and is based on the MERN (Énergie et ressources naturelles Québec) SIGÉOM (Systéme d'information géominière du Québec) stratigraphic vocabulary.

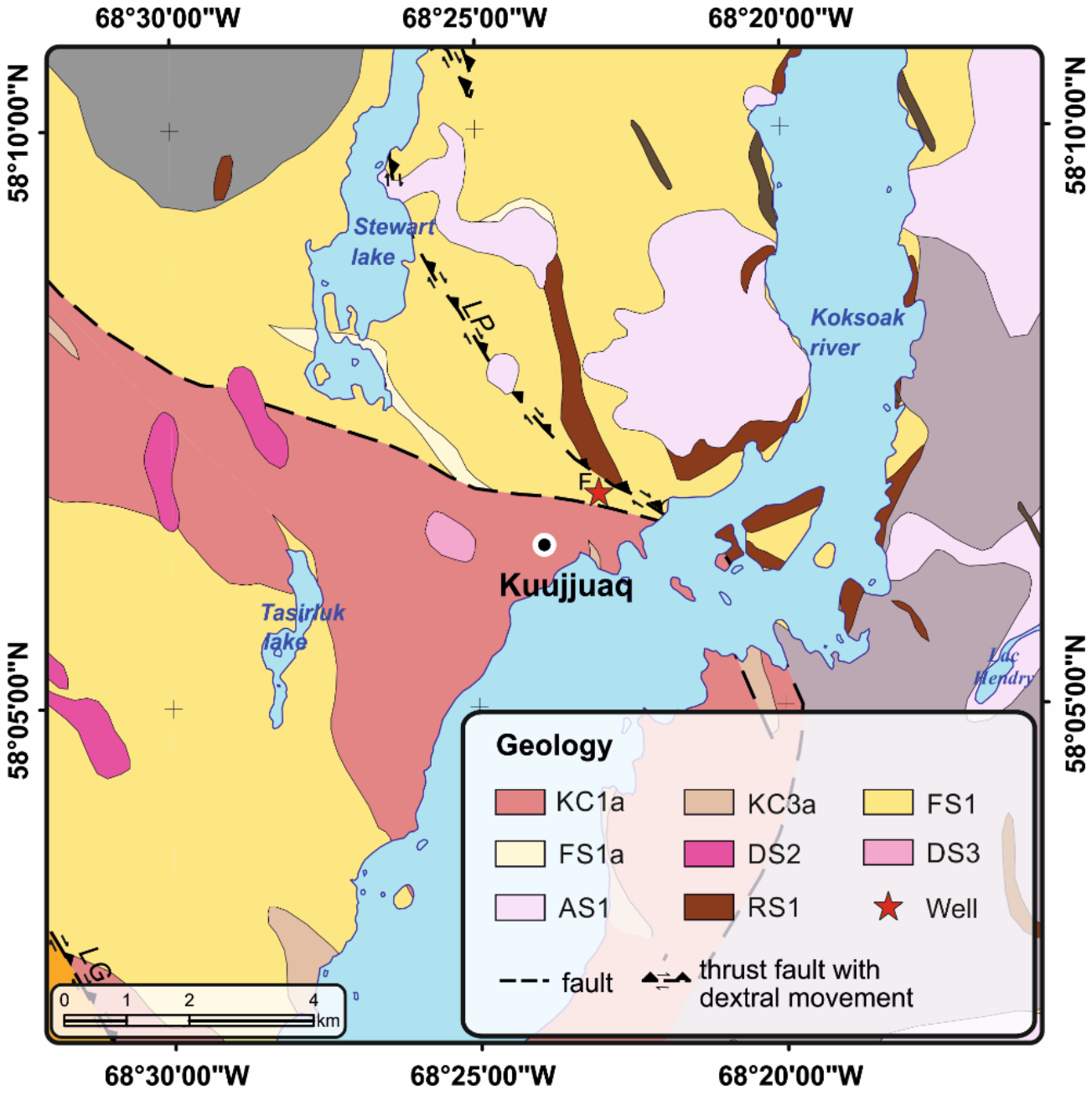

Figure 3.1. Geological map of Kuujjuaq area (adapted from MERN, 2020). F – forum well, LP – Lac Pingiajjulik fault, LG – Lac Gabriel fault, KC – Kaslac Complex, FS – False Suite, DS – Dancelou Suite, AS – Aveneau Suite, RS – Ralleau suite.

The spatial and chronological arrangement of the different geological units was proposed by Lafrance et al. (2020; **Figure 3.2**). The False Suite (3335-2678 Ma) is an extensive cover of Neoarchean metasedimentary rocks lying in discordance on top of the Archean gneiss bedrock formed by the Ungava Complex (2.7-2.9 Ga). Outcrops of the Ungava Complex are observed on the other bank of the Koksoak River (dark grey lithology in **Figure 3.1**). The gneissic and migmatitic bedrock contain enclaves, levels and boudins of mafic and ultramafic intrusive rocks assigned to the Ralleau Suite. The age of this unit is unknown, but field observations suggest that it may in part represent ancient mafic dykes that have been boudinaged or transposed into gneissosity. The intrusive units of the Kaslac Complex (1832-1837 Ma) were emplaced within the gneisses of the Ungava Complex or the paragneisses of the False Suite. The Aveneau Suite (1817-1811 Ma) is the largest Paleoproterozoic intrusive unit. These rocks are interpreted by Simard et al. (2013) as partly representing the final fusion product of the gneisses of the Ungava Complex. Davis et al. (2015) proposed that this unit results either from crystallization that stretched over a long period of metamorphism, possibly in the deep crust, or from the remobilization of slightly older Proterozoic rocks in association with an Archean component. The Aveneau Suite contains enclaves of older units, particularly the Ungava and Qurlutuq complexes and the Ralleau and False suites. In several places, the intrusions of the Aveneau Suite intrude in the form of decimetric to decametric sills in the older rocks. Finally, the Dancelou Suite (1793-1748 Ma) represents the youngest Paleoproterozoic unit of the Baleine lithotectonic domain. It is made up of slightly deformed granitic intrusions that form well-circumscribed kilometric plutons scattered throughout the domain or that intruded in the form of dykes into older units. Like the Aveneau Suite, the Dancelou Suite commonly contains enclaves of surrounding units.

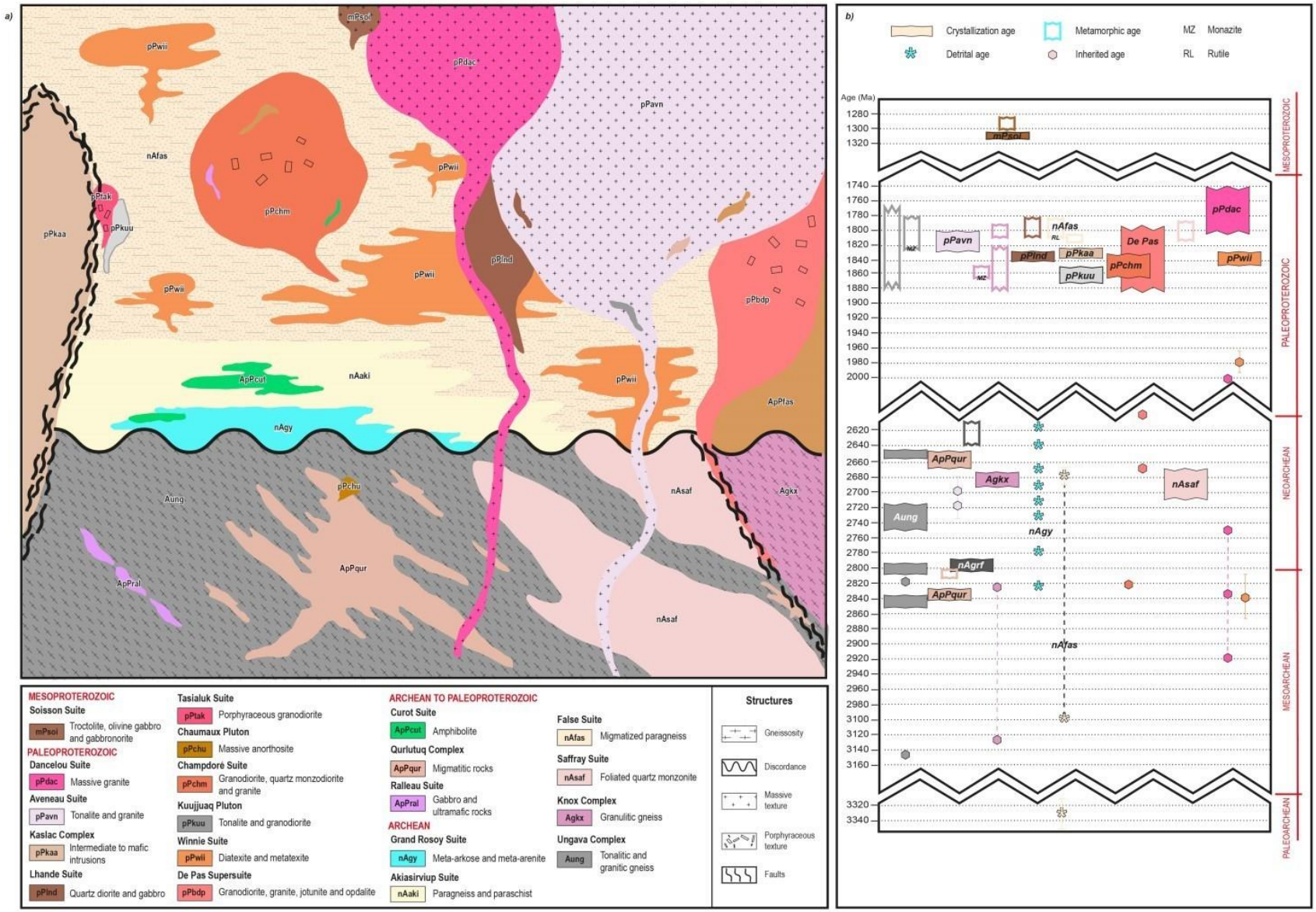

Figure 3.2. Stratigraphic and chronological relationships observed in the Baleine lithotectonic domain (Lafrance et al., 2020): (a) diagram illustrating the main intersecting relationships between stratigraphic units, (b) time scale illustrating the chronology of major geological events. The reader is referred to the original source for further details.

2.1 False suite

The False Suite was introduced by Lafrance et al. (2014) and corresponds to the Baleine Suite in Simard et al. (2013) report. An updated description of this unit can be in MERN's stratigraphic vocabulary webpage: https://gq.mines.gouv.qc.ca/lexique-stratigraphique/province-de-churchill/suite-de-false_en/. This unit groups migmatized metasedimentary rocks, namely migmatized paragneiss, calcosilicate rocks, iron formation and quartzite. The informal unit nAfas1 (migmatized paragneiss) was observed outcropping in Kuujjuaq (FS1; **Figure 3.1**). The informal subunit nAfas1a (migmatized garnet paragneiss) can also be found outcropping in Kuujjuaq (FS1a; **Figure 3.1**).

2.1.1 Texture and mineralogy

The paragneiss rocks of nAfas1 informal unit are characterized by 15-35% discontinuous, millimetric to centimetric-wide, whitish mobilisate usually tonalitic in composition. Alternating bands containing varying amounts of ferromagnesian minerals (10-30%) causing banding as well. The paragneiss is grey in fresh exposure taking a brownish tone when altered. The rock is fine to medium grained with a well-developed granoblastic texture.

The paragneiss is generally poor in microcline and contains very variable amount of quartz (10-35%). The ferromagnesian minerals include brown to red biotite flakes aligned or in millimetric clusters locally associated with hornblende. Apatite, zircon as inclusion in biotite, opaque minerals and allanite are ubiquitous. Muscovite is not ubiquitous but can represent up to 15% of the rock. Other accessory minerals observed are sphene, chlorite, epidote, garnet and sillimanite.

In deformation zones, the rock is schistose and consists of granoblastic plagioclase-quartz lenses circumvented by micas and deformation micro-corridors forming an anastomosed texture. Non-migmatized paragneiss outcrops rich in microcline (20-35%) and poorer in ferromagnesian minerals can also be observed.

The nAfas1a informal subunit occurs in areas where paragneiss and mobilisate contain >5% pink or red garnet in disseminated millimetric grains, in centimetric clusters or as poikiloblasts.

2.1.2 Age

A sample of migmatized biotite-sillimanite-garnet paragneiss yielded detrital U-Pb ages on zircons ranging from 3335 Ma to 2678 Ma (Godet et al., 2020). This age distribution indicates that sediments originate from erosion of Archean rocks of the Baleine lithotectonic domain. The Lu-Hf age of garnet around 1959 Ma allows to estimate the age of metamorphism. Crystallization of the anatectic liquid at 1807 Ma is indicated by the U-Pb metamorphic age of zircons. The U-Pb age of rutile at ~1798 Ma demonstrates rapid cooling after the metamorphic peak (Godet et al., 2020).

2.2 Ralleau suite

The Ralleau Suite is Archean to Paleoproterozoic in age and was identified by Simard et al. (2013). An updated description of this unit can be in MERN's stratigraphic vocabulary webpage: https://gq.mines.gouv.qc.ca/lexique-stratigraphique/province-de-churchill/suite-de-ralleau_en/. This suite is divided into two units: ApPral1 – amphibolitized gabbro and diorite and

ApPral2 – amphibolitized pyroxenite and peridotite. Outcrops of the unit ApPral1 can be found in Kuujjuaq (RS1; **Figure 3.1**).

2.2.1 Unit ApPral1 – amphibolitized gabbro and diorite

This unit consists mainly of amphibolitized gabbro and diorite, locally gabbronorite and quartz gabbro. The rocks of this unit are homogeneous, even grained, granoblastic, medium to fine-grained, and massive to foliated. In fresh exposure, they are dark grey to black, locally greenish. In altered platina, they present a black-an-white-speckled. The rocks of unit ApPral1 are injected by a whitish intrusive phase with a leucosome appearance (<15%). Gabbro and diorite contain 35-65% ferromagnesian minerals mostly represented by green to brown hornblende accompanied by clinopyroxene (1-20%) and brown biotite (1-10%). Accessory minerals are relatively abundant and include opaque minerals, apatite, sphene and epidote accompanied locally by quartz (<5%), garnet, chlorite, carbonate and zircon. Subunit ApPral1a groups amphibolitized garnet gabbro and diorite with decametric to kilometric layers or enclaves contain millimetric to centimetric garnet poikiloblasts in variable amounts (2-35%).

2.2.2 Unit ApPral2 – amphibolitized pyroxenite and peridotite

Unit ApPral2 consists mainly of massive fine to medium-grained dark green pyroxenite. Pyroxenite is locally injected by a whitish granite giving a brecciated appearance. In places, melanocratic olivine gabbro and norite (>85% ferromagnesian minerals) were also assigned to this unit. Pyroxenite is mainly composed of clinopyroxene and green hornblende, but the presence of 30% altered orthopyroxene crystals having a cumulate texture was observed on an outcrop in the Henrietta Lake area. In thin sections, there also are actinolite-rich zones, as well as opaque minerals, apatite and epidote in small amounts. Subunit ApPral2a (Tremolite-Augite-Fuchsite-Plagioclase Schist) corresponds to ultramafic, highly altered and sheared rocks. They are completely transformed into tremolite-augite-fuchsite-plagioclase schists, and likely represent an alteration zone related to the Gabriel Fault. Subunit ApPral2b (Tremolite ultramafic rocks) is bottle green to snow white and contains relics of oikocristic textures (Girard, 1995). It is composed of acicular, radial fibrous or diablastic tremolite, with variable amounts of carbonate, Mg-chlorite and opaque minerals. Intergrowth of tremolite needles gives the rock a massive appearance and great resistance to fracturing. Subunit ApPral2c (Amphibole-Serprentine-Talc Schist) is an ultramafic schist composed of acicular amphibole, talc and serpentine (Girard, 1995).

2.3 Kaslac Complex

The Kaslac Complex was first introduced by Simard et al. (2013). An updated description of this unit can be in MERN's stratigraphic vocabulary webpage: https://gq.mines.gouv.qc.ca/lexique-stratigraphique/province-de-churchill/complexe-de-kaslac_en/. Dating felsic to intermediate intrusive rock samples indicate crystallization ages between 1835 and 1827 Ma.

The Kaslac Complex is described as a complex package of gneissic to mylonitic, primarily intermediate intrusive rocks. This Complex consists of four units: pPkaa1 – gneissic, banded or homogeneous diorite and quartz diorite, pPkaa2 – garnet-magnetite-rich metagabbro, pPkaa3 – mafic and ultramafic intrusions and pPkaa4 – quartz-rich granitoid. The unit pPkaa1, and more specifically the subunit pPkaa1a (amphibole diorite and quartz diorite with absent pyroxene minerals) was identified as the main outcropping in Kuujjuaq (KC1a; **Figure 3.1**). Moreover, rocks of this subunit alternate regularly with millimetric to metric layers of other units of the Kaslac Complex, such as unit pPkaa3 (gabbro and

leucogabbro) and unit pPkaa4 (quartz-rich granitoids). In fact, small outcrops of subunit pPkaa3a (gabbro, gabbronorite and clinopyroxenite) were identified in Kuujjuaq (KC3a; **Figure 3.1**).

2.3.1 Unit pPkaa1 – gneissic, banded or homogeneous diorite and quartz diorite

Unit pPkaa1 is divided into two main subunits based on the absence (pPkaa1a) or presence (pPkaa1b) of pyroxenes. The subunit pPkaa1a is described as amphibole diorite and quartz diorite. The rocks of this subunit include diorite and quartz diorite, locally tonalite, granoblastic and medium-grained, having gneissic, banded or homogeneous appearance. A protomylonitic texture characterized by 5-20% millimetric quartz bands can be observed and is referred to be caused by the intense deformation experienced by these rocks. The banded facies consist of alternating light grey to dark grey millimetric to centimetric bands. Lenticular whitish bands likely corresponding to leucosome or boudinaged injections can also be observed. The homogeneous facies consist of light grey to brown and well foliated to mylonitic diorite. The ferromagnesian minerals (10-30%) form submillimetric clusters stretched parallel to the foliation and consist of amphiboles and dark brown to red biotite. Epidote, garnet, chlorite, muscovite, tourmaline, allanite, sphene, magnetite and ilmenite are accessory minerals that can be observed in the rocks of subunit pPkaa1a. Rocks of this subunit alternate regularly with millimetric to metric layers of gabbro and leucogabbro of unit pPkaa3 and quartz-rich granitoids of unit pPkaa4.

Subunit pPkaa1b comprises orthopyroxene diorite and diorite and the rocks from this unit have a brown sugar or greenish-grey color. They form alternating fine-grained and coarser-grained bands that could represent leucosome or injections transposed during deformation. Coarser-grained bands commonly contain millimetric to centimetric grains of garnet and orthopyroxene. Both types of bands include ferromagnesian mineral clusters mostly consisting of fibrous actinolite and red biotite flakes. These clusters also contain a certain amount of highly serpentinized orthopyroxene and clinopyroxene, the latter in the center of actinolite clusters. Small millimetric grains of garnet were also observed in several places. Accessory minerals are magnetite, apatite, ilmenite and chlorite.

2.3.2 Unit pPkaa2 – garnet-magnetite-rich metagabbro

Unit pPkaa2 consists of different facies of heavily recrystallized gabbro. The main facies consists of garnet porphyroblastic iron oxide gabbro. Secondary facies include garnet-free gabbro and a facies whose composition changes from anorthosite to melanocratic gabbro. A few rare metric websterite and peridotite lenses can also be interstratified with rocks of the previous facies. The presence of a significant number of garnet porphyroblasts in the main facies of the pPkaa2 unit gives the rock a characteristic reddish colour in altered surface. These porphyroblasts are poikilitic, coronitic and represent up to 50% of the rock. Black coronas are well developed and consist of hornblende and plagioclase. The matrix is composed of a generally heterogeneous plagioclase-hornblende ± clinopyroxene ± magnetite ± ilmenite assemblage. Garnet contains clinopyroxene ± hornblende ± plagioclase ± magnetite ± ilmenite inclusions. Some samples are also rich in Fe-Ti oxides. In more deformed areas, the fabric becomes locally gneissic and the modal proportions of ferromagnesian minerals and garnet vary with the bands. Rocks are locally characterized by the presence of garnet-clinopyroxene-hornblende melanosome spatially associated with a small amount of plagioclase-rich leucosome resulting from partial melting. These migmatized rocks occur as metric to decametric layers interstratified with unmelted facies. The garnet-free gabbro facies is more abundant at the edges of intrusions. It consists of gabbro, gabbronorite and norite, locally containing Fe-Ti oxides. Pyroxenes are mostly retromorphosed to amphiboles. Rocks are typically greenish grey in patina and granoblastic. The layered facies, which changes from anorthosite to melanocratic gabbro, is composed of varying amounts of plagioclase and clinopyroxene generally

replaced by hornblende. It also locally contains garnet. Rocks are usually foliated, granoblastic or speckled. They form metric layers interstratified in other facies of the pPkaa2 unit. Contacts are diffuse, with modal proportions of ferromagnesian minerals and garnet gradually changing. There are also layers several tens of metres thick displaying alternating leucocratic to melanocratic wavy centimetric bands, interpreted as primary magmatic layering. Garnet forms porphyroblasts associated with ferromagnesian minerals. In highly foliated areas, garnet form fragmented polycrystalline aggregates or appear as a diffuse rim around ferromagnesian minerals. These mafic facies contain a few rare metric lenses of rusty websterite and peridotite. At the outcrop scale, these rocks define decimetric layers of magmatic origin composed of an orthopyroxene-olivine-clinopyroxene-spinel-magnetite assemblage. Pyroxene and olivine are serpentinized.

2.3.3 Unit pPkaa3 – mafic and ultramafic intrusions

Mafic and ultramafic intrusions of unit pPkaa3 mainly consist of two subunits based on the proportion of ferromagnesian minerals. The first (pPkka3a) consists of variably amphibolitized gabbro, gabbronorite and clinopyroxenite. The second (pPkaa3b) consists of more leucocratic rocks consisting of leucogabbro, leuconorite, diorite, monzonite and anorthosite. A third subunit of amphibolite (pPkaa3c) is also associated with these intrusions.

Subunit pPkaa3a contain 50% to 70% ferromagnesian minerals, a proportion that can reach 90% in some decimetric to metric layers. These rocks are black or dark green, well foliated and medium to fine-grained. Ferromagnesian minerals consist of clinopyroxene and brown or green amphiboles, especially hornblende and fibrous actinolite. Orthopyroxene was also observed locally. Clinopyroxene is partially replaced by amphiboles, so it is possible that the majority of amphiboles present are caused by the alteration of pyroxene. These rocks are highly recrystallized, although locally some of the coarser pyroxene or amphibole crystals have been partially preserved in the granoblastic matrix. Plagioclase-hornblende symplectites are observed around these grains. Accessory minerals are biotite, magnetite, sphene, ilmenite, apatite and carbonate.

Subunit pPkaa3b consists of highly deformed (mylonitic) leucogabbro, leuconorite, diorite, monzonite and anorthosite. These rocks contain 5% to 30% ferromagnesian minerals and have a characteristic speckled appearance formed by a whitish granoblastic plagioclase matrix containing millimetric to centimetric lenticular clusters of black or green ferromagnesian minerals. The rock may also contain up to 12% quartz as discontinuous millimetric bands. In several places, a porphyroclastic texture is defined by the presence of 5-20% centimetric plagioclase crystals contained in a fine-grained granoblastic matrix. Although the porphyroclasts' shape has been preserved, they are completely recrystallized. K-feldspar porphyroclasts are also observed locally. Ferromagnesian minerals (5-30%) are composed of varying amounts of green hornblende, dark brown to red biotite, clinopyroxene, apatite, opaque minerals and some sphene. Ferromagnesian mineral clusters are well stretched in foliation. Within clusters, however, minerals are finely recrystallized and randomly oriented, intergrown with each other or with silicate minerals, taking on a shattered appearance possibly associated with metamorphism or intense deformation. Some coronitic textures are observed. They are formed from a core of clinopyroxene surrounded by hornblende and biotite.

At the north end of the Baleine Domain, potentially intrusive amphibolites were also associated with the Kaslac Complex. Amphibolite is black, granular and mostly composed of hornblende with lesser amounts of quartz, plagioclase and garnet. The rock is locally schistose and represents metamorphosed intrusive or effusive rocks according to Gold (1962).

2.3.4 Unit pPkaa4 – quartz-rich granitoid

Unit pPkaa4 groups quartz-rich intrusive rocks that form a few klippes thick enough to be mapped. It usually occurs in centimetre to metre-wide layers interstratified in lithological assemblages of other units of the Kaslac Complex. The rock of unit pPkaa4 is white, beige or light grey. It is well foliated to mylonitic, fine to medium grained and entirely granoblastic. It contains 50-85% quartz in millimetric bands, variably sericitized plagioclase and some accessory minerals including garnet, biotite, muscovite, tourmaline, epidote, chlorite and rutile.

2.4 Aveneau Suite

The Aveneau Suite was identified by Simard et al. (2013). An updated description of this unit can be in MERN's stratigraphic vocabulary webpage: https://gq.mines.gouv.qc.ca/lexique-stratigraphique/province-de-churchill/suite-aveneau_en/. This unit was defined to group whitish intrusive rocks. The informal unit pPavn1 has been identified outcropping in Kuujjuaq (AS1; **Figure 3.1**). This informal unit consists of whitish tonalite and granite with significant grain size variation, containing fine to coarse-grained rock piles. The rocks belonging to the Aveneau Suite are massive to foliated caused by the alignment of biotite schlierens, which are main ferromagnesian minerals presented in small percentage (1-8%). Muscovite is ubiquitous (1-5%) and accessory minerals observed consisting of opaque minerals, sphene, epidote and zircon, garnet, sericite and carbonate.

Informal subunit pPavn1a corresponds to areas where whitish intrusions of the Aveneau Suite are more heterogeneous, mainly due to many partially assimilated enclaves and 10-30% biotite schlierens in the rock. Enclaves are mostly composed of diorite, gneiss (e.g., paragneiss) and migmatite. In these areas where geology is heterogeneous, samples of the suite resemble migmatitic rocks of the Qurlutuq Complex; however, continuous banding is neither observed on outcrops nor in fresh exposure. Biotite schlierens are commonly aligned with foliation.

The two crystallization ages of the Aveneau Suite are Paleoproterozoic and contemporaneous to the crystallization period of the Winnie Suite anatectic liquid (1838-1807 Ma) derived from melting of False Suite paragneiss. The dating also gave ancient inherited ages indicating that the Aveneau Suite originated from melting of Archean rocks. The Aveneau Suite has been interpreted as the final melting product of Ungava Complex gneiss (Simard et al., 2013). However, geochronological results from migmatites of the Qurlutuq Complex, which are derived from partial melting of gneiss, do not adequately limit partial melting age to the Paleoproterozoic.

ID-TIMS analyses of three Proterozoic zircon groups that are representative of a distinct population, with no evidence of Archean nuclei, yielded very precise and consistent results, but have a significant value range of 40 Ma, i.e., between 1832 Ma and 1792 Ma (Davis et al., 2015). According to Davis et al. (2015), tonalite would result from either remobilization of slightly older Proterozoic rocks in association with an Archean component, or from crystallization that has stretched over a long period of time, possibly in the deep crust, during a period of metamorphism. The presence of monazite in one of the samples could also indicate a sedimentary component in the source (Davis et al., 2014).

2.5 Dancelou Suite

The Dancelou Suite was described by Simard et al. (2013). An updated description of this unit can be in MERN's stratigraphic vocabulary webpage: https://gq.mines.gouv.qc.ca/lexique-stratigraphique/province-de-churchill/suite-de-dancelou_en/. This unit groups poorly deformed and late tectonic granitic intrusions that cut older units. It consists of homogeneous and massive biotite granite forming well-circumscribed kilometric plutons or dykes intruding older units. Three informal units have been identified: pPdac1 – fine-grained grey granite, pPdac2 – massive pink granite and pPdac3 – massive pegmatitc granitic. The two last informal units have been recognized outcropping in Kuujjuaq (DS2 and DS3; **Figure 3.1**).

2.5.1 Age

Paleoproterozoic ages obtained in the Dancelou Suite are consistent with field observations indicating late tectonic emplacement. Dating suggests that the pegmatitic granite unit (pPdac3) would be older than the granite unit (pPdac2); however, field relationships indicate the opposite. Samples collected in different units come from different areas, hence it is possible that different pegmatitic phases intruded at different times.

2.5.2 Unit pPdac1 – fine-grained grey granite

The granite of informal unit pPdac1 is homogeneous, weakly foliated or massive and fine to medium grained. The grey colour is characteristic, giving it the appearance of tonalite on outcrops. However, feldspar staining, and thin-section observation highlight a significant amount of K-feldspar (30-45% of the rock). Granite contains 4-10% brownish biotite flakes. These flakes contain small zircon grains surrounded by a very clear dark brown pleochroic aureole. The rock also contains 1-5% muscovite as disseminated flakes or altering plagioclase (sericite), as well as minor accessory minerals including epidote, allanite, apatite and opaque minerals. Myrmekitic textures are commonly observed in thin sections.

2.5.3 Unit pPdac2 – massive pink granite

The informal unit pPdac2 granite has a pinkish color and a medium grain size with decametric coarse to pegmatitic clusters. This granite is also distinguished by its low ferromagnesian mineral content (<5%) and when presented, these minerals consist of small flakes of brown biotite and chlorite containing small zircon grains. Muscovite (up to 2%) and low amount of hematite, epidote and apatite are also observed.

2.5.4 Unit pPdac3 – massive pegmatitic granite

The pegmatitic granite of informal unit pPdac3 intrudes into the other informal units of the Dancelou Suite. The granite is light pink and contains <5% of ferromagnesian minerals, mainly brown-red biotite flakes and muscovite is ubiquitous (<5%). This intrusive rock shows slight recrystallization along feldspar grains, while quartz zones form subgrains having undulatory extinction. Plagioclase is weakly sericitized and the accessory minerals are sparse and include epidote, hematite, apatite, garnet and zircon.

4. CORE LOGGING

Knowing the subsurface geology is important for deep geothermal potential assessments. This knowledge can be gain by studying the recovered core pieces from geothermal exploration wells. This was done in this report and is discussed in this section. The objective of this section is to characterize the core pieces recovered in terms of lithology, geological unit, structures present (induced and natural fractures) and core recovery parameters. The methodology followed, the results obtained, and a discussion and interpretation of these results is provided below.

4.1 Methodology

4.1.1 Core description

The 234 m of core recovered from the Forum well was studied, and a graphic log was produced to reflect information on the lithological succession. The different lithologies were identified on a literature-based comparison approach. Grain/crystal size, texture (i.e., size, shape and arrangement of the crystals) and other important features were described for each lithology identified. Additional observations were carried out in an attempt to distinguish natural from induced fractures in the cores. Differentiating natural from induced fractures, although not always obvious, is meaningful since the latter contribute nothing to reservoir permeability and should not be included in fracture-permeability models (Lorenz and Cooper, 2018). Drilling-induced fractures can, however, provide clues to in situ stress directions and magnitudes (Schmitt et al., 2012). Kulander et al. (1990) and Lorenz and Cooper (2018), for instance, present several criteria useful for distinguishing natural from induced fractures in core that were followed in this work. According to these authors, induced fractures are commonly rough, unmineralized and are fresh breaks. These also have lips at the core edge. The plumes (i.e., feather-like markings on the fracture walls; **Figure 4.1**) usually interact with the core edge and follow the core axis. The induced fracture planes are consistently normal or parallel to the core axis. Natural fractures, in contrast, present mineralization, and if unmineralized, their orientation and geometries are similar to the mineralized fractures. Natural fractures do not interact with the core surface. The plumes, steps, or slickenlines have axes that are unrelated to the core axes. Natural fractures are also generally more planar and more systematic than induced fractures (i.e., natural fractures tend to be more planar, parallel and evenly spaced than induced fractures, which tend to be more irregular in terms of spacing and orientation).

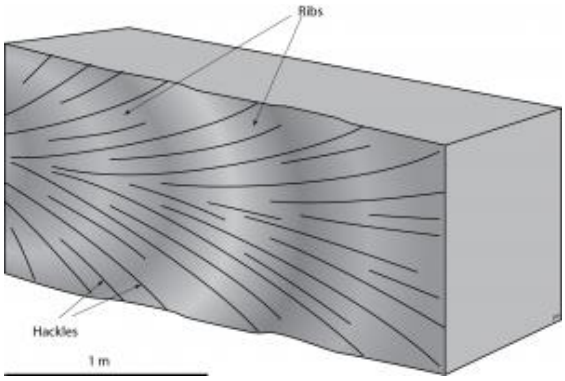

Figure 4.1. Example of the geometry of plume structures on a fracture surface (Waldron and Snyder, 2020).

The fracture analysis was carried out using the scanline sampling method to collect fracture information and to make stick plots, histogram of frequencies, cumulative frequency diagrams and statistical

measures to analyze the data sampled and evaluate the fractures spatial arrangement (Sanderson and Peacock, 2019). The scanline sampling method is based on data collection from all fractures that intersect a scanline (Zeeb et al., 2013 and references therein). In the scanline sampling method, a tape is laid down on top of the rock mass and the fractures intersecting the scanline are written down (**Figure 4.2**).

Figure 4.2. Example of the application of the scanline sampling method to acquire fracture geometrical information on an outcrop surface.

The scanline sampling method is a quick method and widely used in outcrops to collect information about the geometrical properties of fractures (i.e., orientation, dip, aperture, length, spacing, infilling), providing 1D information on fracture networks, and is the main method used for the analysis of cores (Zeeb et al., 2013). In the context of this work, the scanline sampling method was applied to locate each fracture intersecting the tape and their depth along the borehole (**Figure 4.3**). The fractures intersecting the tape were then distinguished between natural and induced fractures following the aforementioned criteria. One disadvantage of the scanline sampling method is that vertical fractures are unrepresented since these structures are parallel to the tape and therefore do not intercept it (**Figure 4.3**).

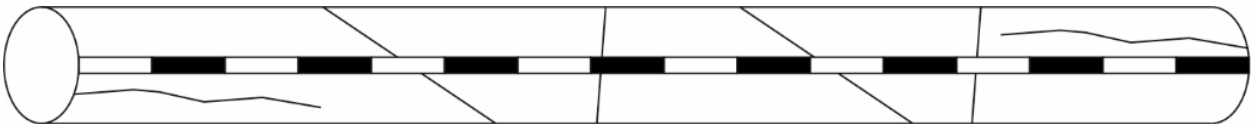

Figure 4.3. Sketch exemplifying the application of the scanline sampling method to acquire fracture spatial information on a core piece.

The stick plot is a simple log that shows the location (i.e., depth) of each fracture intersected by the scanline. The stick plot allows a qualitative interpretation of the spatial arrangement of the fractures, enabling to qualitatively identify fracture clustering (**Figure 4.4**). Stick plots were produced in this work for both natural and induced fractures.

Figure 4.4. Example of stick plots representing different fracture spatial distributions (Sanderson and Peacock, 2019): (a) equally spaced fractures (uniform distribution), (b) random distributed fractures, (c) fracture corridor in the central section of the scanline, (d) fractal clustering of fractures.

4.1.2 Core description

The quality of the 234 m core recovered from the Forum well was described based on core recovery parameters. These include total core recovery, solid core recovery and rock quality designation and, despite playing no role in geothermal studies, these are important geotechnical parameters to describe the quality of the rock mass. The total core recovery (TCR) is the borehole core recovery percentage and is defined as:

$$TCR = \frac{l_{\text{sum of pieces}}}{l_{\text{total core run}}} \times 100\% \quad (\mathbf{4.1})$$

where $l_{\text{sum of pieces}}$ (m) is the sum of length of core pieces and $l_{\text{total core run}}$ (m) is the total length of core run.

The solid core recovery (SCR) is the borehole core recovery percentage of solid, cylindrical, pieces of rock core and is defined as:

$$SCR = \frac{l_{\text{total length of core in pieces>core diameter}}}{l_{\text{total core run}}} \times 100\% \quad (\mathbf{4.2})$$

where $l_{\text{total length of core in pieces > core diameter}}$ (m) is the sum of length of solid, cylindrical, core pieces greater than the diameter of the core.

Finally, rock quality designation (RQD) is the borehole core recovery percentage incorporating only pieces of solid core that are longer than 10 cm in length measured along the centerline of the core. The RQD is defined as:

$$RQD = \frac{l_{\text{sum of length of core pieces>100mm}}}{l_{\text{total core run}}} \times 100\% \quad (\mathbf{4.3})$$

where $l_{\text{sum of length of core pieces > 100 mm}}$ (m) is the sum of length of core pieces greater than 10 cm measured along the centerline. The quality of the rock mass can then be defined according to the RQD index (**Table 4.1**).

Table 4.1. Classification table.

RQD	Rock mass quality
<25%	Very poor
25-50%	Poor
51-75%	Fair
76-90%	Good
91-100%	Excellent

4.2 Results

4.2.1 Core description

The core recovered (**Appendix II – Core**) was analyzed and the lithologies defined according to the literature description in **section 3. Geology** to produce the graphical well log (**Appendix I – Well log**). The core was photographed on an outside area and under natural light, at different parts of the day (morning and afternoon) and different atmospheric conditions (sunny and cloudy days). The color differences observed on the photographs in **Appendix II – Core** are mostly due to the different light and atmospheric conditions.

The core pieces identified as belonging to the paragneiss lithology (assigned to the False Suite geological unit; **Appendix III – Paragneiss**) are characterized by alternating bands of leucocratic and ferromagnesian minerals that cause banding (**Figure 4.5a**). This rock is generally medium grained with a granoblastic texture, but some core pieces present porphyroclasts (**Figure 4.5b**). The feldspar minerals present a pink to reddish tone. A tonalitic mobilisate can be observed in some of the core pieces (**Figure 4.5c**).

The core pieces classified as diorite/gabbro (**Appendix IV – Diorite/Gabbro**) were assigned to the Kaslac Complex geological unit, but some of these pieces may belong to the Ralleau Suite. The distinction between rocks of these units is not clear at hand sample scale. The core pieces recovered are majority black, well foliated and medium to fine-grained. A protomylonitic texture characterized by quartz bands can be observed (**Figure 4.6a, b**). The content of ferromagnesian minerals is greater than leucocratic minerals. Boudinage injections or leucosome (**Figure 4.6c**) and clusters of garnet minerals (**Figure 4.6d**) are also present in some rock samples. Metagabbro core pieces can also be observed (**Figure 4.6e**).

Finally, some of the core pieces recovered reveal similarities with tonalite/granite lithologies of Aveneau Suite and/or Dancelou Suite but these can also belong to the quartz-rich granitoid subunit of the Kaslac Complex (**Appendix V – Tonalite/Granite/Granitoids**). These core pieces vary from a white to a reddish tone. They are medium to coarse grained with a pegmatitic texture in some core samples and with low content of ferromagnesian minerals. Some samples show alignment of biotite schlieren (**Figure 4.7a**). At the top of the core, pieces classified as tonalite/granite are highly fractured and these structures show infillings (**Figure 4.7b**).

Figure 4.5. Features of the paragneiss core samples: a) banding caused by alternating bands of leucocratic and ferromagnesian minerals, b) porphyroclast (highlighted by the green square), c) tonalitic mobilisate (highlighted by the green square).

Figure 4.6. Features of the diorite/quartz diorite/gabbro core samples: a) and b) protomylonitic texture, c) boudinage injection or leucosome, d) clusters of garnet minerals (highlighted by the green square), e) metagabbro facies.

a)

b)

Figure 4.7. Features of the tonalite/granite core samples: a) alignment of biotite schlieren, b) fissures and veins.

An attempt to distinguish natural from non-natural fractures was made (**Appendix I – Well log**). The distinction between natural and induced fractures took into account the presence of mineralization, lips at the core edge and fracture shape. Two main groups of natural fractures were observed, inclined and horizontal. Fractures cutting the core at an angle might be inclined extension fractures or high- (>65º) to intermediate-angle (35º-65º) shear fractures (**Figure 4.8**). Features such as slickensides, slickenlines and steps were not well preserved (**Figure 4.8**). Some of the inclined fractures observed may also be related to foliation.

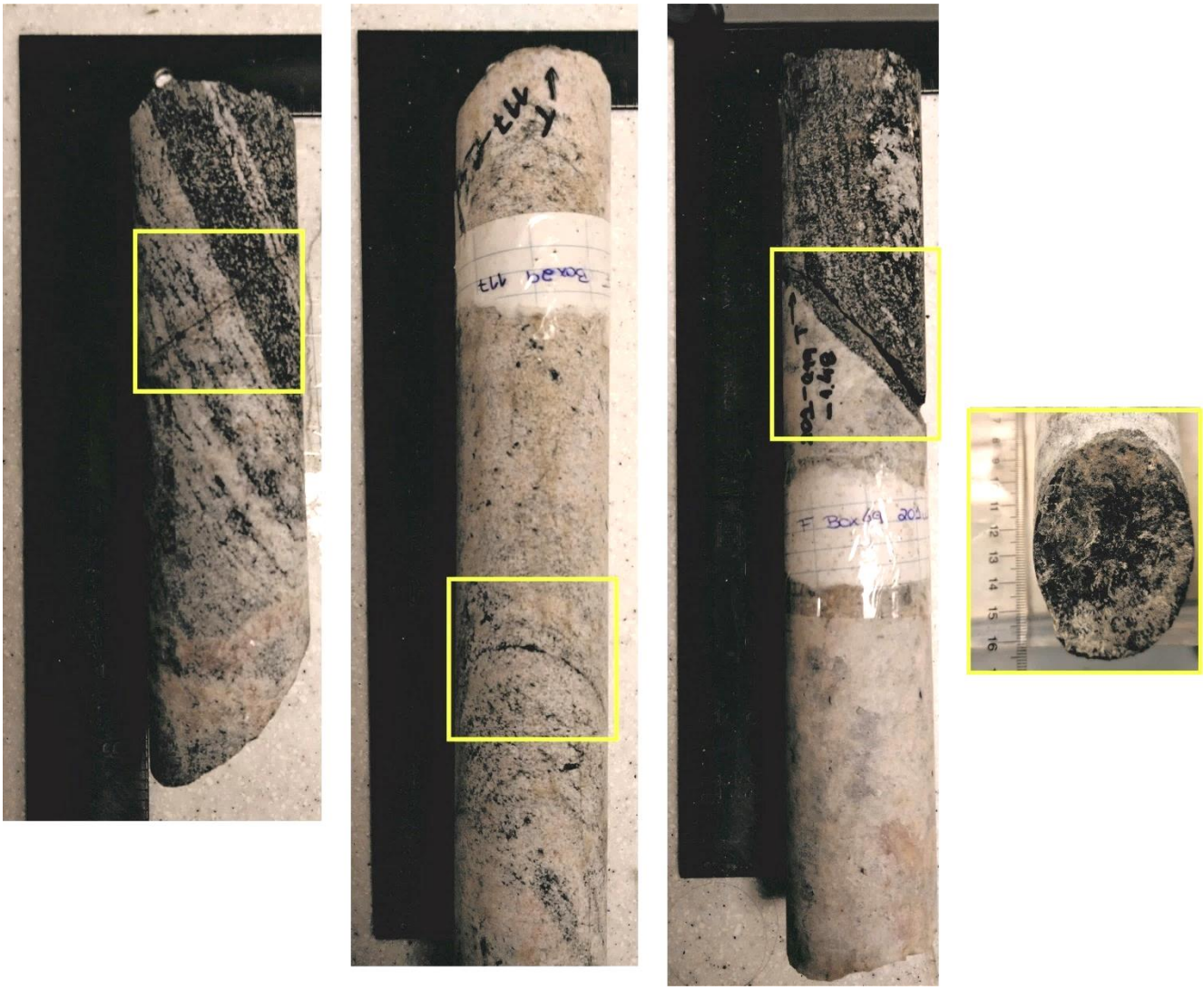

Figure 4.8. Example of inclined fractures (highlighted by the green square) observed along the core.

Horizontal fractures presenting a smooth surface and in which the two walls perfectly matched might be extension fractures (**Figure 4.9**). Some of these structures show mineralization (**Figure 4.9**). Horizontal fractures with lips at the core edge, with rough walls and in which the two fracture walls do not perfectly match were considered induced fractures (**Figure 4.10**). Fissures, veins and expulsion structures were detected (**Figure 4.11**). Vertical fractures (**Figure 4.12**) were also observed but these did not intersect the scanline.

Figure 4.9. Example of horizontal natural fractures (highlighted by the green square) observed along the core.

Figure 4.10. Example of horizontal induced fractures (highlighted by the green square) observed along the core.

Figure 4.11. Example of fissures (right), veins (center) and expulsion structures (left) observed along the core.

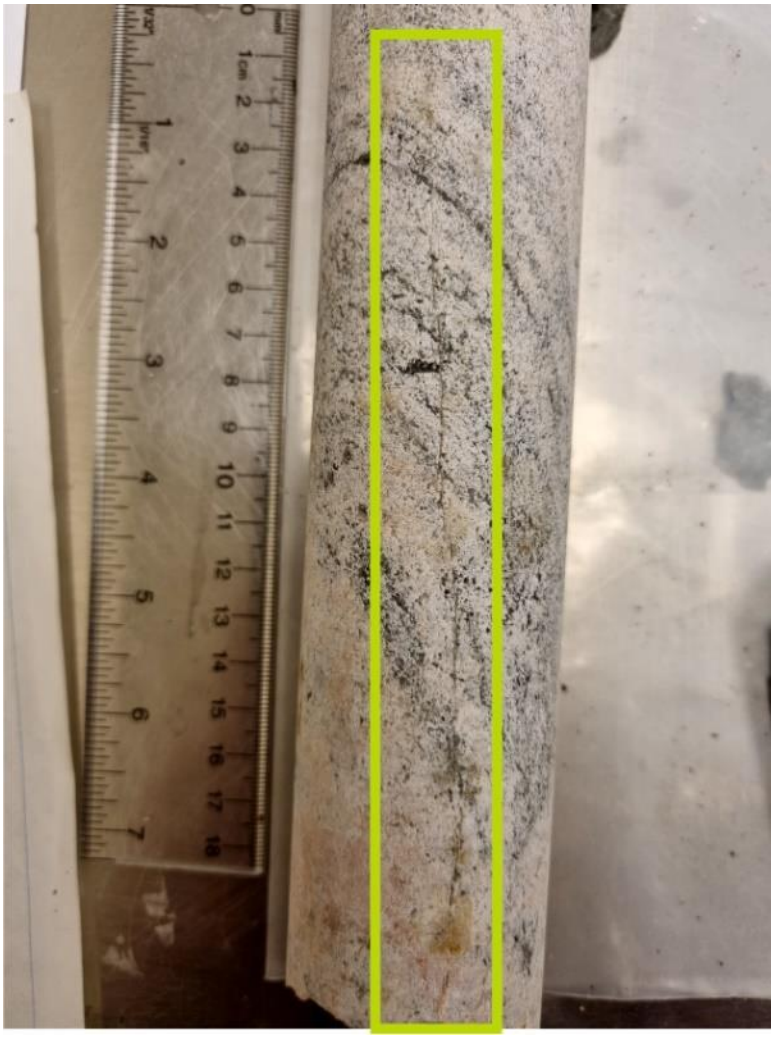

Figure 4.12. Example of a vertical natural fracture (highlighted by the green square) observed along the core.

Non-natural fractures can be grouped into three categories, drilling-induced, coring-induced and handling-induced (Kulander et al., 1990). Drilling-induced fractures propagate in the rock ahead of the bit during drilling (Kulander et al., 1990). Coring-induced fractures can develop anywhere in the core barrel, but generally form near the bit and before, or at, the scribe knives (Kulander et al., 1990). Handling-fractures form primarily during removal of the core from the core barrel, or during the plugging and slabbing process. These fractures may also be induced when the core is transported or when core lengths are sized to permit boxing for shipment and storage (Kulander et al., 1990). Within the non-natural fractures observed, the majority seems to be coring- and handling-induced. While coring-induced disc fractures, for example, are observed in several sections of the core (**Figure 4.13**), few drilling-induced fractures (centerline, petal-centerline) were recognized (**Figure 4.14**). Artifacts, such as core top and core base, tip polish and scratches or core-catcher drag (**Figure 4.15**), can also be observed along the core. A blasted zone was detected in the first 27 meters of core (**Appendix II - Core**). This might be a result of geotechnical operations during the construction of the Forum building. Another zone of highly damaged core is visible between 144 and 153 meters deep (**Appendix II - Core**).

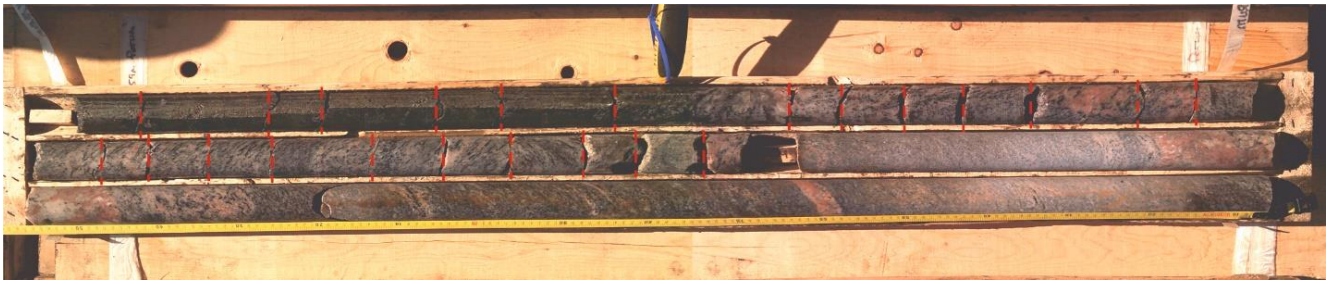

Figure 4.13. Example of coring-induced disc fractures (highlighted by the dashed red lines) observed in a section of the core (180 m depth).

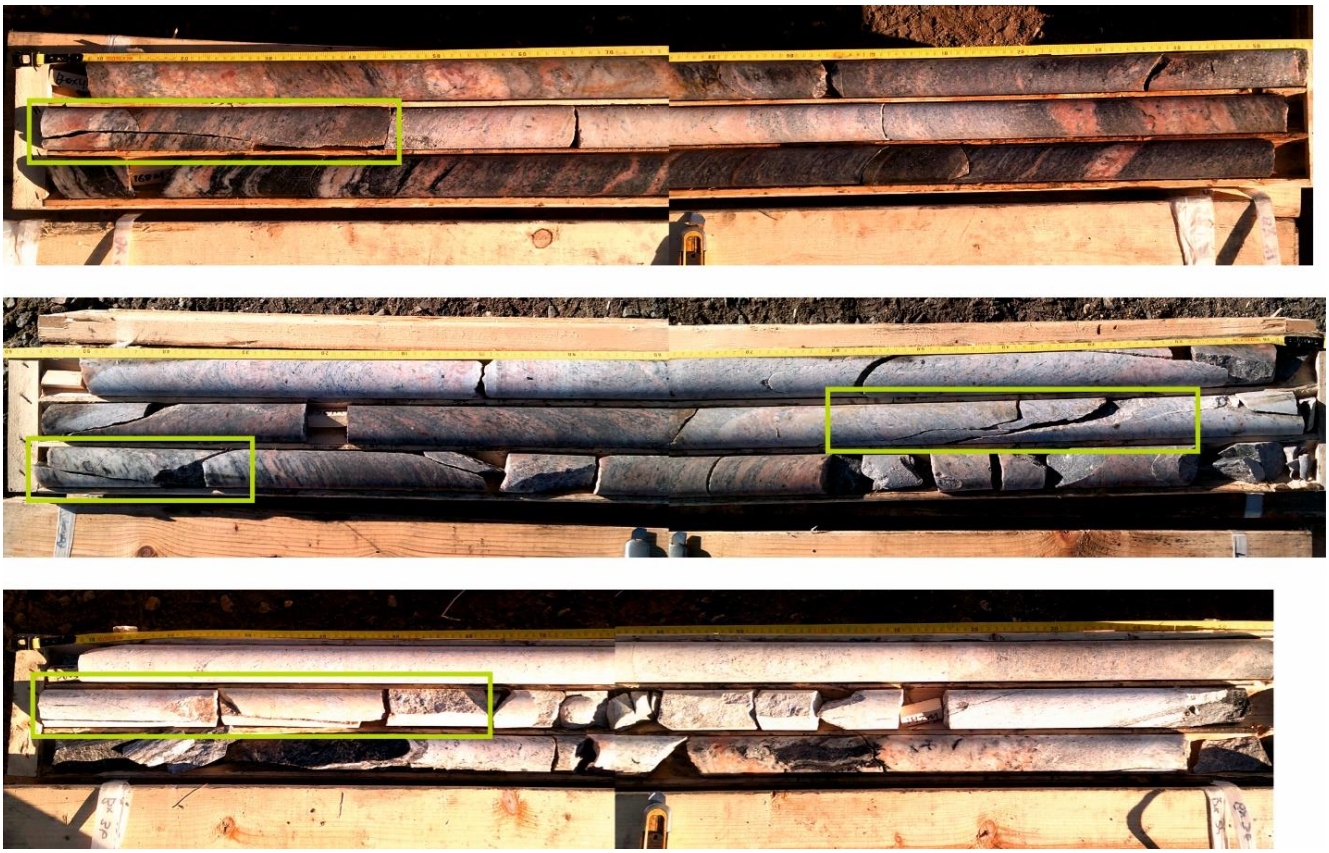

Figure 4.14. Example of drilling-induced centerline and petal-centerline fractures (highlighted by the green squares) observed in several sections of the core (top – 168 m depth; center – 150 m depth; bottom – 147 m depth).

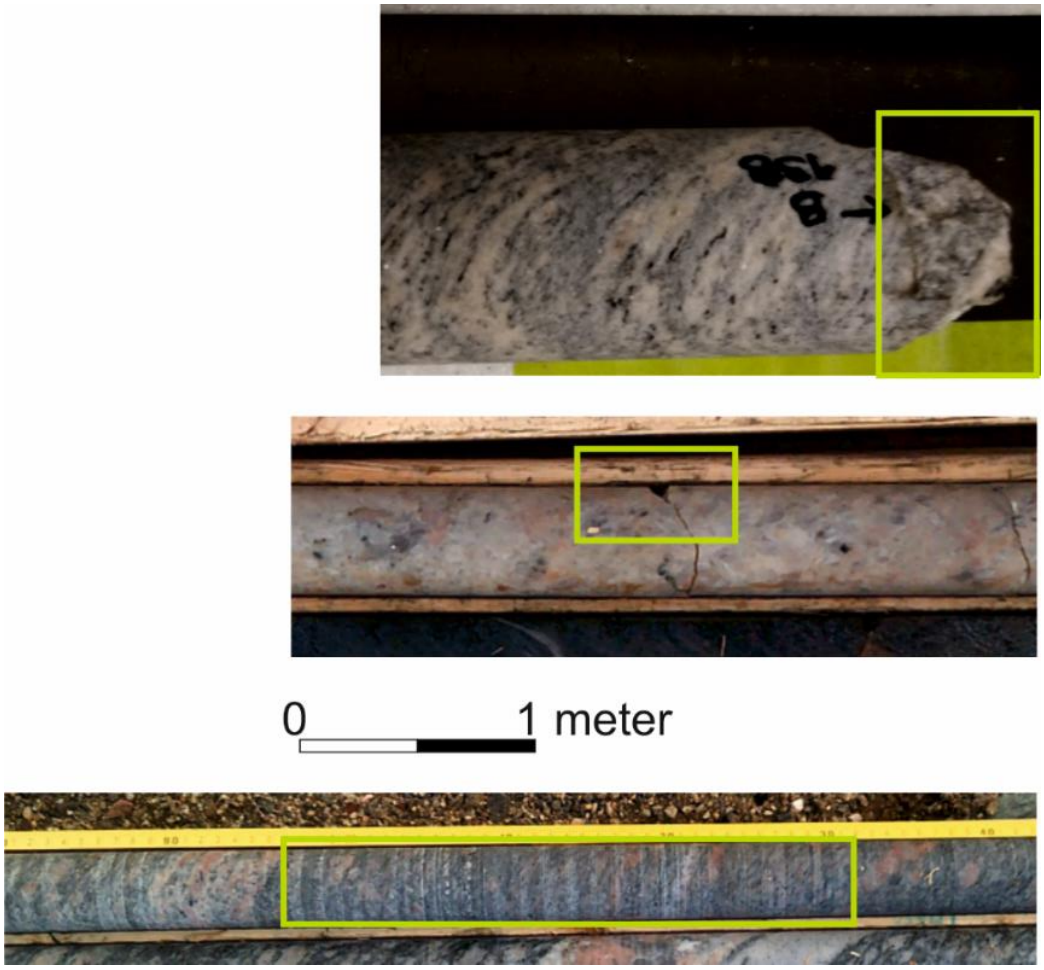

Figure 4.15. Example of artifacts (highlighted by the green squares) observed along the core (top – core base, center – tip polish, bottom – scratch/core catcher drag).

4.2.2 Core recovery parameters

The total core recovery (**Eq. 4.1**) was estimated greater than 90% and the solid core recovery (**Eq. 4.2**) between 80 and 90%. The rock quality designation index (**Eq. 4.3**) was estimated about 80% indicating a good rock mass quality (**Table 4.1**).

4.3 Discussion

The 234 m core recovered from the Forum well was analyzed and several lithologies and geological units identified. However, some doubt still exists in regard to some of the lithologies encountered. Analytical techniques, such as X-ray powder diffraction, are planned to identify minerals and thus improve the lithological classification. Nevertheless, based on this first-order analysis, the paragneiss seems the dominant lithology, and is intersected by minor intrusions of mafic (diorite/gabbro) and felsic (tonalite/granite/granitoid) intrusive rocks (**Appendix I – Well log**).

Opening-mode fractures and faults are the most important structures in fractured-dominated geothermal systems, providing permeability and preferential fluid flow pathways (e.g., Dezayes et al., 2021). An attempt was made to distinguish natural from non-natural fractures. The stick plot produced for the

natural fractures intersecting the scanline (**Appendix I – Well log**) seems to suggest a non-uniform distribution with randomly distributed fractures and fracture clustering at certain depth intervals. Analysis of the fractures suggest two main groups of natural fractures, inclined and horizontal. The inclined fractures encountered can be extension fractures (i.e., Mode I fractures; opening-mode fractures; **Figure 4.16a**) or intermediate- to high-angle shear fractures (i.e., Mode II fractures; sliding-mode fractures; **Figure 4.16b**). Modes of fracture refers to the decomposition of crack tip stresses into three loadings (Zehnder, 2013). In Mode I the stress is orthogonal to the local plane of the crack surface, in Mode II the stress is parallel to the crack surface but orthogonal to the crack front, and in Mode III stress is parallel to the crack surface and to the crack front (Zehnder, 2013).

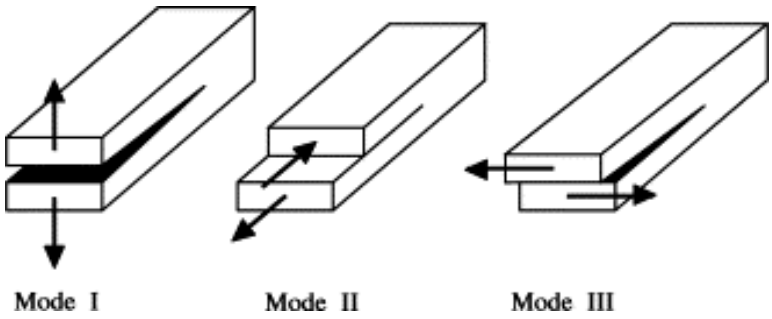

Figure 4.16. Three basic modes of crack propagation (Chang et al., 2002).

Fracture wall features to distinguish between extension and shear fractures were not well preserved. Extension fractures (or, Mode I) tend to form normal to the minimum principal stress since it is the least energy configuration (Lorenz and Cooper, 2018). Inclined extension fractures can probably be the result of a strike-slip faulting regime, where the maximum and minimum principal stresses are horizontal, and the vertical stress is intermediate. Intermediate- to high-angle shear fractures (or Mode II) are formed in a strike-slip regime (Lorenz and Cooper, 2018). Horizontal fractures may be indicators of a reverse faulting regime, where the minimum principal stress is vertical. The presence of both inclined and horizontal natural fractures may suggest a reverse/strike-slip stress regime, which agrees with published stress data for the Canadian Shield and lends support to the theoretical stress estimates carried out by Miranda et al. (submitted).

Cores are also useful stress indicators (Schmitt et al., 2012). Drilling-induced fractures, such as petals, centerline, petal-centerline and saddles, are created during drilling operations and their shapes and spacing contain clues to in situ stress directions and magnitudes. However, since the core is not oriented and these features were not common along the core, little information can be extracted about the stress field beyond the possible reverse/strike-slip faulting regime. Coring-induced fractures, such as disc fractures, were observed in several portions of the core. These induced fractures form primarily in response to a vertically acting principal tension. The primary stress responsible for discing may be attributed to in-situ stresses, unloading and bit pressure assisted by torsional stresses and vibrations that accompany drilling and coring (Kulander et al., 1990).

As previously mentioned, the core recovered is unfortunately not oriented and thus no further information could be retrieved about fracture orientation and principal stresses direction. It is important to highlight, however, the data analyst subjective bias (e.g., Andrews et al., 2019). Studies have shown that fracture gathering and interpretation are subject to the geologists' own subjective biases which introduce scientific uncertainty and have implications on the geothermal system design.

5. THERMAL CONDUCTIVITY

Assessing the terrestrial heat flux requires a knowledge of the geothermal gradient and of the thermal conductivity of the geological materials. This section is focused on the evaluation of the thermal conductivity of representative core samples. The method used, the results obtained, and their interpretation are provided below.

5.1 Methodology

5.1.1 Theoretical background

The Thermal Conductivity Scanner (TCS also known as Optical Scanning Instrument, OSI) is a laboratory device to measure thermal conductivity and thermal diffusivity on rock and drill core samples. The instrument used in this work was produced by TCS – Lippmann and Rauen and its specifications are given in **Table 5.1**. The advantages of the optical scanning method include high speed of operation and short measuring time, contactless mode of operation and measurement, the ability to measure directly on a core sample and to estimate the thermal anisotropy and inhomogeneity of rocks, the simultaneous determination of thermal conductivity (measured of the ability of a material to conduct heat) and thermal diffusivity (rate of heat transfer of a material) from one experiment, the ability for continuous profiling of thermal properties to investigate thermal heterogeneity related to structural and textural characteristics of the samples and flexibility in spatial resolution and penetration depth of measurements by changing the scanning velocity and heater-sensor separation (Popov et al., 1999, 2016). Thermal conductivity and thermal diffusivity are related by the following expression:

$$\alpha = \frac{\lambda}{\rho c} \qquad (\mathbf{5.1})$$

where α ($m^2\ s^{-1}$) is the thermal diffusivity, λ ($W\ m^{-1}\ K^{-1}$) is the thermal conductivity and ρc ($J\ m^{-3}\ K^{-1}$) is the heat capacity.

Table 5.1. TCS instrument specifications.

	Specifications
Measurement range	TC: 0.2 – 25 $W\ m^{-1}\ K^{-1}$ TD: 0.6×10^{-6} to $3.0 \times 10^{-6}\ m^2\ s^{-1}$
Accuracy and precision	TC: 3% (for a confidential probability of 0.95) TD: 5%
Productivity	Up to 60 samples per hour (depending on sample length)
Sample dimensions	40 to ≈ 500 mm length with any given shape but with a flat or cylindrical surface ≥ 60 mm diameter for core samples
Maximum scanning length	620 mm
Scanning speed	5 $mm\ s^{-1}$
Sample preparation	No polishing or sawing necessary, preliminary painting (a paint strip with 25-40 micrometer thickness and width of appr. 20 mm) along the scanning line on flat or cylindrical surface is necessary
TCS software	Controlling software with intuitive user interface and manual

TC – thermal conductivity, TD – thermal diffusivity.

The TCS instrument comprises a focused optical heater (i.e., an electric lamp), three infrared sensors, a cradle to hold the optical head, a linear motion system, reference standards with known thermal properties and an electronic and power unit (**Figure 5.1**).

Figure 5.1. TCS instrument.

The principle behind the TCS is the optical scanning technology, which was developed by Yuri Popov in the 1980s and 1990s. Theoretical background of this methodology is provided by, for example, Popov et al. (1999, 2016 and references therein). Briefly, the theoretical model is based on scanning a sample surface with a focused, mobile and continuously operated constant heat source in combination with three infrared temperature sensors (**Figure 5.2**).

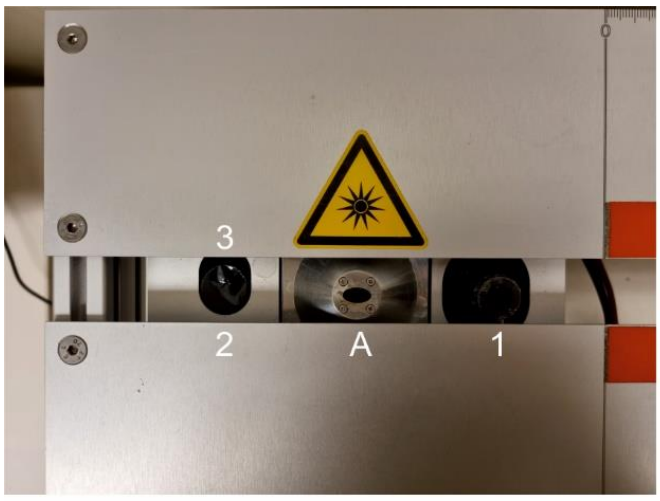

A - Optical heater

1 - Infrared temperature sensor (cold sensor)

2 - Infrared temperature sensor (hot sensor)

3 - Infrared temperature sensor (hot-y sensor)

Figure 5.2. Heat source and infrared temperature sensors.

The heat source (A) and sensors move with the same speed relative to the sample and at a constant distance of each other. Infrared temperature sensor 1 (or, cold sensor) records and displays the value of the unheated sample surface temperature. Infrared sensors 2 and 3 (or, hot and hot-y sensors), located

after the heat source, record and display the value of the maximum temperature rise (**Figure 5.3**). Sensors 2 and 3 are located a few mm apart. This 3-channel type of infrared temperature sensor allows the simultaneous measurement of thermal conductivity and thermal diffusivity from one single experiment.

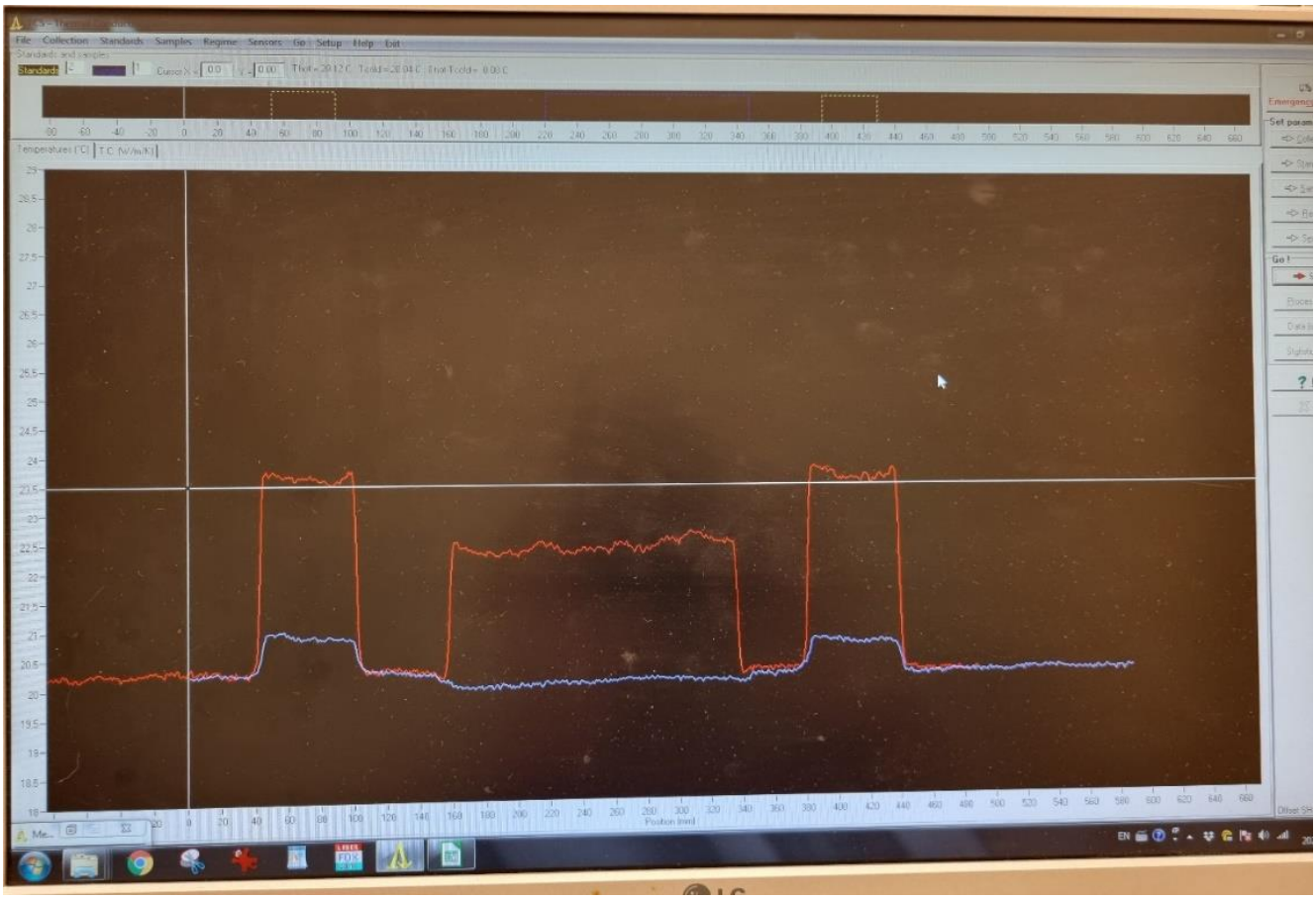

Figure 5.3. Example of the temperatures recorded by the cold (blue line) and hot (red line) sensors.

The optical scanning method is based on solutions of the thermal conduction equation for a quasi-stationary temperature field in a movable coordinate system OXYZ. The origin, O, of the coordinate system coincides with the location of the heat source on the surface of the sample. The axis OZ is perpendicular to the sample surface, and the axes OX and OY lie along the flat surface of the sample. When the heat source moves at a constant velocity in the direction of the OX axis, the excess temperatures ($T_2 - T_1$) and ($T_3 - T_1$), defined as differences between the temperatures T_2 and T_3 recorded with sensors 2 and 3 behind the heater and an initial sample surface temperature T_1 recorded with sensor 1 in front of the heater, are described by the equations (Popov et al., 2016 and references therein):

$$\begin{cases} T_2 - T_1 = \frac{q}{2\pi x_0 \lambda} \\ T_3 - T_1 = \frac{q}{2\pi\lambda R} exp\left[-\frac{v(R-x_0)}{2\alpha}\right] \end{cases} \quad (\mathbf{5.2})$$

where v (m s^{-1}) is the velocity of the heat source across the sample, q (W) is the heat source power, λ (W m^{-1} K^{-1}) is the thermal conductivity and α (m^2 s^{-1}) is the thermal diffusivity. $R^2 = (x_0^2 - y_0^2)$ is a distance related with the position of the heat source and sensors 2 and 3.

Thermal conductivity and thermal diffusivity of an isotropic rock sample are determined from Eq. (**5.3**) provided that two reference standards with known thermal conductivity and thermal diffusivity are scanned in series with the rock sample:

$$\begin{cases} \lambda = \frac{\lambda_{R1}\times(T_{2R1}-T_{1R1})+\lambda_{R2}\times(T_{2R2}-T_{1R2})}{2(T_2-T_1)} \\ \alpha = \frac{\alpha_{R1}\times ln\left(\frac{\lambda_{R1}\times(T_{3R1}-T_{1R1})}{\lambda_{R2}\times(T_{3R2}-T_{1R2})}\right)}{ln\left(\frac{\lambda_{R1}\times(T_{3R1}-T_{1R1})}{\lambda_{R2}\times(T_{3R2}-T_{1R2})}\right)+\frac{\alpha_{R2}-\alpha_{R1}}{\alpha_{R2}}\times\left(\frac{\lambda\times(T_3-T_1)}{\lambda_{R1}\times(T_{3R1}-T_{1R1})}\right)} \end{cases} \quad (\mathbf{5.3})$$

where the subscript R1 and R2 refer to the reference standards 1 and 2, respectively.

The following characteristics are determined from the thermal conductivity and thermal diffusivity profiles:

- Average value of thermal conductivity and thermal diffusivity (corresponding to heat flow direction in the rock sample along the scanning line)
- A set of local values of thermal conductivity and thermal diffusivity distributed along the scanning line
- Maximum and minimum values of thermal conductivity and thermal diffusivity along the scanning line
- Inhomogeneity factor

5.1.2 Experimental setup

Before the TCS analysis, a scanning line is painted on the rock surface using a black silicone paint (**Figure 5.4**). This is done for a complete absorption of infrared heating. The thermal conductivity of the selected samples was evaluated using the TC mode. Due to the small sample diameter (about 45 mm) only the TC mode could be used. The minimum sample diameter recommended from the TCS manufacturer is 60 mm. The small diameter of the samples made thermal diffusivity evaluation unreliable (i.e., in all the analyzes made, thermal diffusivity was constantly out of range) and therefore it was preferred not to evaluate this parameter. Two gabbro standards with thermal conductivity of 2.39 W m^{-1} K^{-1} were placed before and after the rock specimen (C1 and C2; **Figure 5.5**). The recommended heat source power for this set of standards was applied. This value is approximately 37.5 W. The default head velocity of 5 mm s^{-1} was used. The sampling was set for 1 mm. The temperature sensors (both hot and cold) were calibrated before each scan (i.e., continuous thermal conductivity evaluation along the core sample). Three scans were done for each rock sample to ensure reproducibility:

$$MRE = \frac{TCS_{n-1}-TCS_n}{TCS_{n-1}}\times 100 \quad (\mathbf{5.4})$$

where *MRE* (%) is the mean relative error used to evaluate the reproducibility. TCS (W m^{-1} K^{-1}) is the thermal conductivity evaluated at each scan (represented by the subscripts n-1 and n).

Figure 5.4. Black silicone painted on the samples surface.

Figure 5.5. Example of the experimental setup for thermal conductivity analysis.

The coefficient of variation is automatically calculated by the TCS software at the end of each scan as:

$$CV = \frac{\sigma}{\mu} \times 100 \quad \textbf{(5.5)}$$

where *CV* (%) is the coefficient of variation and σ (W m^{-1} K^{-1}) and μ (W m^{-1} K^{-1}) are respectively the standard deviation and the mean thermal conductivity. The mean and standard deviation are calculated based on the thermal conductivity values evaluated along the core sample. The *CV* displays the extent of thermal conductivity variability in relation to the mean value. The higher this value is, the greater the dispersion of the thermal conductivity along the core sample and a sign of a very heterogeneous and complex mineralogical arrangement.

An inhomogeneity factor is also automatically evaluated at the end of each scan. This factor provides a quantitative measure of the rock samples heterogeneous character. The inhomogeneity is calculated as:

$$I_{\text{factor}} = \frac{max-min}{\mu} \quad \textbf{(5.6)}$$

where max (W m^{-1} K^{-1}) and min (W m^{-1} K^{-1}) are the maximum and minimum thermal conductivity evaluated, respectively. Both *CV* and I_{factor} are a function of the core sample length.

The harmonic mean was used to evaluate the core thermal conductivity considering the lithological variations along the borehole:

$$\frac{1}{\lambda_{\text{core}}} = \frac{1}{z}\sum_{i=1}^{n}\frac{z_i}{\lambda_i} \quad \textbf{(5.7)}$$

5.2 Results

A thermal conductivity profile was constructed based on the laboratory analyzes (**Appendix I – Well log**). The paragneiss samples analyzed revealed an average thermal conductivity varying between 2.5 and 2.9 W m^{-1} K^{-1} while the diorite/gabbro samples have an average thermal conductivity ranging between 1.9 and 2.4 W m^{-1} K^{-1} (**Figure 5.6**; **Table 5.2**). Both paragneiss and diorite/gabbro revealed inhomogeneity factors ranging between 0.1 and 0.3, with exception of two samples with values of 0.6 and 0.7 (**Table 5.2**). Similarly, the coefficient of variation revealed low values, with exception of two samples with values near 20%, suggesting a lower dispersion of the thermal conductivity (**Table 5.2**).

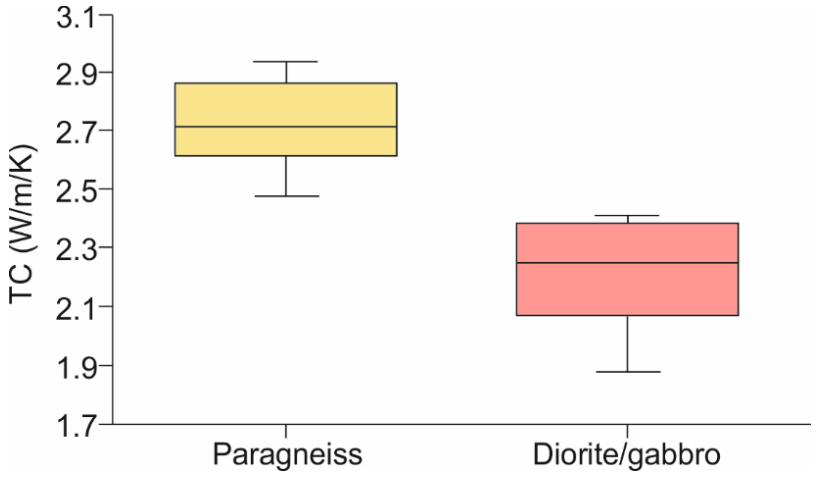

Figure 5.6. Thermal conductivity boxplot with whiskers from minimum to maximum. Paragneiss – n = 8, Diorite/gabbro – n = 7.

Table 5.2. Thermal conductivity results.

ID	Depth (m)	Lithology	TC ($W\ m^{-1}\ K^{-1}$)			CV (%)	I_{factor}	Relative error (%)
			Minimum	Mean	Maximum			
			2.599	2.795	3.047	3.442	0.161	---
F6	6	Paragneiss	2.627	2.788	3.000	2.920	0.134	0.25
			2.577	2.769	2.935	3.133	0.129	0.68
			2.137	2.378	2.750	7.560	0.258	---
F12	12	Diorite/Gabbro	2.109	2.393	2.792	7.673	0.285	-0.63
			2.092	2.378	2.757	7.691	0.280	0.63
			2.774	2.936	3.121	2.320	0.118	---
F33	33	Paragneiss	2.754	2.924	3.085	2.603	0.113	0.41
			2.755	2.939	3.122	2.974	0.125	-0.51
			1.778	1.901	2.013	3.080	0.123	---
F42	40.55	Diorite/Gabbro	1.734	1.860	1.969	3.109	0.127	2.16
			1.740	1.874	1.984	3.291	0.130	-0.75
			2.435	2.650	2.824	3.049	0.147	---
F48	46.35	Paragneiss	2.397	2.648	2.845	3.487	0.169	0.08
			2.415	2.625	2.776	2.652	0.138	0.87
			2.216	2.431	2.790	6.198	0.236	---
F54	54	Diorite/Gabbro	2.207	2.415	2.785	6.060	0.239	0.66
			2.172	2.379	2.715	6.323	0.228	1.45
			1.719	2.484	3.346	19.228	0.655	---
F108	108	Paragneiss	1.740	2.480	3.399	19.184	0.669	0.16
			1.742	2.462	3.209	18.676	0.596	0.73
			2.233	2.362	2.563	2.975	0.140	---
F117	114.88	Diorite/Gabbro	2.273	2.375	2.596	3.043	0.136	-0.55
			2.283	2.386	2.574	3.171	0.122	-0.46
			2.605	2.808	3.004	2.191	0.142	---
F138	138	Paragneiss	2.628	2.791	3.002	2.209	0.134	0.61
			2.645	2.795	3.008	2.357	0.130	-0.14
			1.870	2.249	2.581	8.474	0.316	---
F156	156	Diorite/Gabbro	1.864	2.256	2.586	8.436	0.320	-0.31
			1.873	2.247	2.578	8.570	0.313	0.40
			2.575	2.879	3.080	3.136	0.175	---
F183	183	Paragneiss	2.628	2.867	3.029	3.082	0.140	0.42
			2.617	2.894	3.144	3.236	0.182	-0.94
			1.910	2.070	2.302	3.950	0.189	---
F201	201	Diorite/Gabbro	1.936	2.076	2.349	4.296	0.199	-0.29
			1.951	2.069	2.389	4.142	0.212	0.34
			2.356	2.612	3.047	5.449	0.265	---
F210	210	Paragneiss	2.342	2.609	3.111	5.718	0.295	0.11
			2.352	2.613	3.154	5.796	0.307	-0.15
			1.685	2.102	3.032	18.207	0.641	---
F228	226	Diorite/Gabbro	1.676	2.086	3.041	18.293	0.654	0.76
			1.673	2.082	2.946	17.452	0.611	0.19
			2.195	2.619	3.087	8.091	0.340	---
F234	233.85	Paragneiss	2.230	2.622	3.071	7.967	0.321	-0.11
			2.247	2.654	3.074	7.716	0.312	-1.22

Furthermore, the core thermal conductivity is found to vary between 2.4 and 2.8 W m^{-1} K^{-1}, with a median value of 2.6 W m^{-1} K^{-1}. This distribution of thermal conductivity values is similar to the range found for the paragneiss, reflecting the predominance of paragneiss compared to diorite/gabbro lithology. Thus, assuming a homogeneous subsurface made of paragneiss is not an incorrect simplification. The minimum, median and maximum values used in the Monte Carlo simulations to evaluate heat flux assumed the thermal conductivity distribution of the paragneiss (i.e., 2.5, 2.7 and 2.9 W m^{-1} K^{-1}, respectively).

The TCS instrument was set to evaluate thermal conductivity at every 1 mm. This allows to map the thermal conductivity along the sample analyzed surface and obtain a first-order evaluation of the sample's thermal heterogeneity. The thermal conductivity profiles obtained for each sample are shown in **Appendix VI – Thermal conductivity**.

5.3 Discussion

Thermal conductivity of selected core pieces representative of the main lithologies encountered was analyzed with the optical scanning technique. The paragneiss samples analyzed revealed an average thermal conductivity varying between 2.5 and 2.9 W m^{-1} K^{-1}, while the diorite/gabbro samples have an average thermal conductivity ranging between 1.9 and 2.4 W m^{-1} K^{-1}. These values differ from a previous evaluation carried out using surficial samples and the same optical scanning technique (Miranda et al., 2020a). The surficial paragneiss samples revealed thermal conductivities ranging between 2.1 to 2.9 W m^{-1} K^{-1} (thermal conductivity evaluated with TCS). The thermal conductivity for the surficial diorite/gabbro varied between 2.3 to 3.5 W m^{-1} K^{-1} (thermal conductivity evaluated with TCS). Such variability may be caused by the more widespread spatial distribution of the surficial samples compared to the well core samples. In fact, the surficial paragneiss samples collected at a distance of 2-3 km from the well location have an average thermal conductivity of 2.6 W m^{-1} K^{-1} (evaluated with the TCS). The surficial gabbro samples collected at a distance of 1-2 km from the well reveal a thermal conductivity of 2.3 W m^{-1} K^{-1} (evaluated with the TCS; Miranda et al., 2020a).

Miranda et al. (2020a) also evaluated thermal conductivity of surficial samples using two methods, the optical scanning and the guarded heat flow meter. The latter is a steady-state method that is often considered more accurate since thermal conductivity is evaluated after the sample reached a thermal equilibrium state. Miranda et al. (2020a) results revealed a mean relative error of -15% for the paragneiss surficial samples and -2% for the gabbro/diorite surficial samples, with the guarded heat flow meter values at the denominator. The authors suggest that this variability can be caused by the intrinsic heterogeneity of the rock samples. In fact, the thermal conductivity profiles obtained for the core samples analyzed in this work with the optical scanning technique puts in evidence this sample thermal heterogeneity. Further work is envisioned to compare the thermal conductivity obtained with the optical scanning technique with the transient plane source and guarded heat flow meter techniques.

The evaluation of the heat flux considered a homogeneous subsurface made of paragneiss. This was justified by the similar thermal conductivity values obtained for the paragneiss and for the overall core (i.e., 2.5-2.9 W m^{-1} K^{-1} and 2.4-2.8 W m^{-1} K^{-1}, respectively). Furthermore, preliminary estimates of heat flux through numerical models undertaken by Miranda et al. (2021a) assumed a homogeneous subsurface made of paragneiss. Therefore, for comparison purposes it was preferred to estimate the heat flux assuming the same homogenous conditions.

6. SURFACE HEAT FLUX

Heat flux is a primary parameter to assess the geothermal potential of a target area. However, evaluating this parameter from temperature profiles implies that these need to be deep enough to observe the linear increase in temperature with depth and that the temperature profiles are corrected for both artificial and natural disturbances (e.g., drilling, true-vertical depth, free thermal convection, groundwater flow, topography, paleoclimate, etc.; e.g., Jessop, 1990). Neglecting the corrections for these features may lead to important misestimations of heat flux (e.g., Jessop, 1990). Thus, the temperature profile used in this work to evaluate heat flux was firstly corrected for the effects of drilling-induced thermal disturbances and then for the effects of paleoclimate events. **Figure 6.1** illustrates the impact of the drilling and paleoclimate corrections on measured temperature profiles. Carrying out these geothermal gradient corrections allows adjustment of the instantaneous gradient at all points of a temperature profile at depth to obtain the gradient in equilibrium. It is important to highlight that, in the case of the Forum well, the correction for drilling-induced thermal disturbances is applied to correct the warming effect caused by drilling operations thus opposite to what is shown in **Figure 6.1**. In other words, the corrected temperature from drilling operations (blue point in **Figure 6.1**) for the Forum well is lower than the measured temperature profile (green point in **Figure 6.1**).

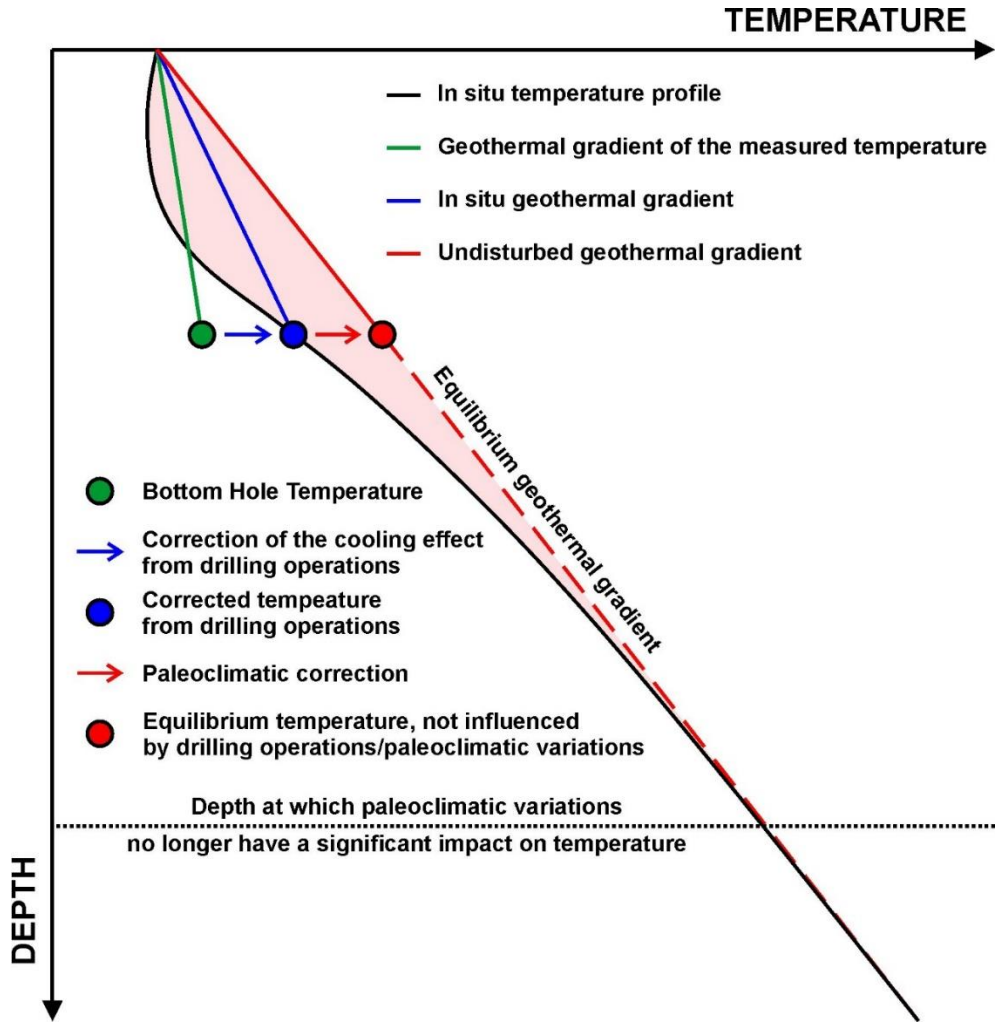

Figure 6.1. Impacts of the corrections applied to the temperatures measured in wells (modified from Bédard et al., 2016).

Topographic corrections were not considered since the well was drilled at an altitude of about 40 m above sea level and these were considered negligible. The temperature profile was measured by Géotherma solutions inc. shortly after the drilling operations were completed (Géotherma solutions inc, 2022). The temperature profile was acquired with a submersible temperature and pressure data logger (RBRduet), which has an accuracy of ± 0.002 ºC and ± 0.25 cm. The probe was inserted in the well about 10 min before the beginning of the recording to ensure the thermal equilibrium between the probe and the groundwater in the well. The temperatures were recorded in a continuous temperature logging pace of about 1 m per 10 s. Depth calibrations were made along the profile by correlating the pressure measurements with the exact depth measured with the wire.

6.1 Correction for drilling-induced thermal disturbance

6.1.1 Theory

The drilling process (i.e., the friction of drilling and the heat exchange with the drilling fluid) introduces temporary thermal disturbances to the surrounding rock (Jessop, 1990). Thus, temperature logs recorded shortly after drilling operations are influenced by these drilling-induced thermal disturbances and do not represent rock temperatures at equilibrium. Several methods have been developed over the years to correct log temperatures for drilling-induced thermal disturbances (e.g., Leblanc et al., 1982; Kutasov and Eppelbaum, 2005, 2010; Zschocke, 2005; Ascencio et al., 2006; Goutorbe et al., 2007; Schumacher and Moeck, 2020; Agemar, 2022). Among these, the analytical line source Horner method is widely applied. This correction method requires multiple measurements to be made at different times after the end of the drilling. This makes possible to determine the equilibrium temperature by plotting the observed temperature against a time function (**Figure 6.2**). The latter corresponds to the logarithmic function of the time elapsed since end of drilling and the time of duration of the drilling and is given by (Jessop, 1990):

$$t = \log\left(1 + \frac{t_{\text{drilling}}}{dt}\right) \quad \textbf{(6.1)}$$

where t (h) is the time function, t_{drilling} (h) is the duration of drilling and dt (h) is the time elapsed since completion. Most temperature logs corrected based on Horner's method use a mud circulation time (normally 3 to 24h) instead of the drilling duration time (e.g., Allis et al., 2018). This is done since the objective is to have the temperature of the fluid inside the well in equilibrium and evaluate if the temperature goal of the drilling campaign has been reached. On the other hand, if the goal is to have a continuous temperature profile where the fluid inside the well and the surrounding rock are in thermal equilibrium, then the drilling duration time is more appropriate. It is important to bear in mind that the drilling operations are not only influencing the most recent drilled part of the well but also disturbing the already drilled surficial part.

Therefore, in this work, the total drilling duration time (i.e., 99h; see section **2. Forum well**) was preferred in order to obtain not only the equilibrium temperature of the fluid inside the well but also of the rock around it (Jessop, 1990). No mud circulation time is available for the Forum well. The time function becomes zero when the time elapsed is very large and the intercept gives the equilibrium temperature (**Figure 6.2**).

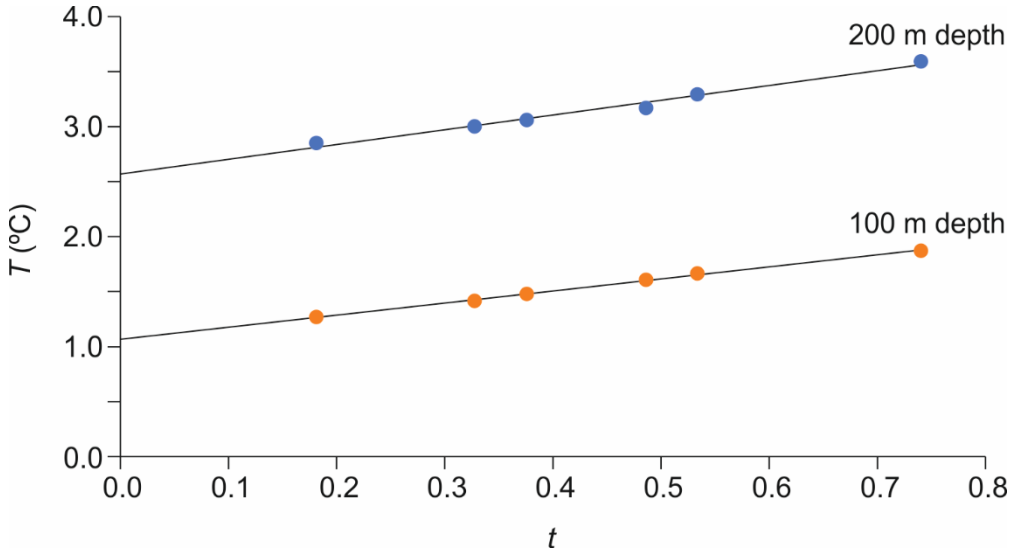

Figure 6.2. Example of a Horner plot with temperature data recorded in Kuujjuaq.

The Horner method was developed to correct bottom-hole temperature (bottom-hole temperature provides a single temperature point at the bottom of the well). Therefore, the application of the Horner method to continuous temperature logs requires correcting the temperature at every temperature-depth point. In a way of simplifying the application of the Horner method to continuous temperature logs, the following equation was applied:

$$T_{\text{corrected}}(z) = m \ln\left(\frac{dt}{t_{\text{drilling}}+dt}\right) + T_{\text{measured}} \quad \textbf{(6.2)}$$

where T (ºC) is the temperature and m (ºC h^{-1}) is the slope of the time function-temperature given by the Horner plot. T_{measured} (ºC) is the temperature profile measured. This equation was developed to extrapolate bottom-hole temperature after correction for drilling disturbances. In this work, the intercept and slope were estimated at every 1 m depth and used to calibrate **Eq.** (**6.2**) and verify if it could be applied to obtain the corrected continuous temperature profile instead of correcting every temperature-depth point.

Additionally, the resulting temperature profile corrected following Horner's method was compared with other correction methods (Leblanc et al., 1982; Schumacher and Moeck, 2020). Leblanc et al. (1982) use a cylinder source method to correct bottom-hole temperatures:

$$T_{\text{corrected}}(z) = \text{T}_{\text{measured}} - \Delta T\left(exp\left(\frac{-r^2}{4\alpha dt} - 1\right)\right) \quad \textbf{(6.3)}$$

where ΔT (ºC) is a temperature difference between the true formation temperature and the temperature of the contents of the well at t = 0, r (m) is the radius of the well and α (m^2 s^{-1}) is the thermal diffusivity of the contents of the well. The temperature difference factor ΔT, in this work, was assumed to be the difference between a temperature profile measured 1 day after the ending of the drilling and one measured 8 days after the drilling was finished. This correction method will be referred hereafter as Leblanc method.

Schumacher and Moeck (2020) proposed three new equations that can be used to correct continuous temperature logs and were developed based on an empirical approach. These correction equations use

two main parameters – the cross-over point and the thermal disturbance. The cross-over point corresponds to a depth-point at which the thermal disturbance due to mud circulation is zero and was empirically determined by Förster (2001) as:

$$z_{\mathrm{cp}} = 0.39 \times \mathrm{z_{total}} + 267 \quad \textbf{(6.4)}$$

where z_{cp} (m) is the cross-over point and z_{total} (m) is the total length of the temperature profile.

The thermal disturbance (ΔT; ºC) corresponds to the temperature difference between the surface temperature of the log (T_0; ºC) and the true surface temperature (T_s; ºC) as (Schumacher and Moeck, 2020):

$$\Delta T = \mathrm{T_0} - T_{\mathrm{s}} \quad \textbf{(6.5)}$$

The first correction equation (method A) proposed by Schumacher and Moeck (2020) is:

$$T_{\mathrm{corrected}}(z) = \mathrm{T_{measured}} - \left(\Delta T - \frac{\Delta T - z}{z_{\mathrm{cp}}}\right) \quad \textbf{(6.6)}$$

where z (m) is a depth-point.

The second correction equation (method B) proposed by Schumacher and Moeck (2020) is similar to the previous one with addition of a third term:

$$T_{\mathrm{corrected}}(z) = \mathrm{T_{measured}} - \left(\Delta T - \frac{\Delta T - z}{z_{\mathrm{cp}}}\right) \times \left(1 - \frac{z}{z_{\mathrm{total}} + 50}\right) \quad \textbf{(6.7)}$$

The third correction equation (method C) proposed by Schumacher and Moeck (2020) is similar to method A with addition of a term to correct temperature profiles that exceed the cross-over point:

$$T_{\mathrm{corrected}}(z) = \begin{cases} \mathrm{T_{measured}} - \left(\Delta T - \frac{\Delta T - z}{z_{\mathrm{cp}}}\right) & \text{for } z < z_{\mathrm{cp}} \\ \mathrm{T_{measured}} + \Delta T_2 \times \left(\frac{z - z_{\mathrm{cp}}}{z_{\mathrm{total}} - z_{\mathrm{cp}}}\right) & \text{for } z \geq z_{\mathrm{cp}} \end{cases} \quad \textbf{(6.8)}$$

where ΔT_2 (ºC) is a temperature difference between the lowermost log measurement and the corrected value by Förster (2001) for this depth. The temperature profile used in this work is shorter than the cross-over point depth and therefore only method A and method B were applied.

6.1.2 Results

The temperature profile corrected for drilling-induced thermal disturbance using Horner's method indicates that the equilibrium temperature is approximately 0.2 ºC lower than the temperature profile measured 8 days after the ending of drilling (**Figure 6.3a**). Furthermore, the application of **Eq.** (**6.2**) provides a good fit to the depth-point equilibrium temperature from Horner's plot (**Figure 6.3b**). The different temperature profiles measured at different times after drilling was completed highlighting that drilling operations disturbed the whole well temperature (**Figure 6.3a**). This supports the use of the total drilling duration time to correct the temperature profile for drilling-induced thermal disturbances.

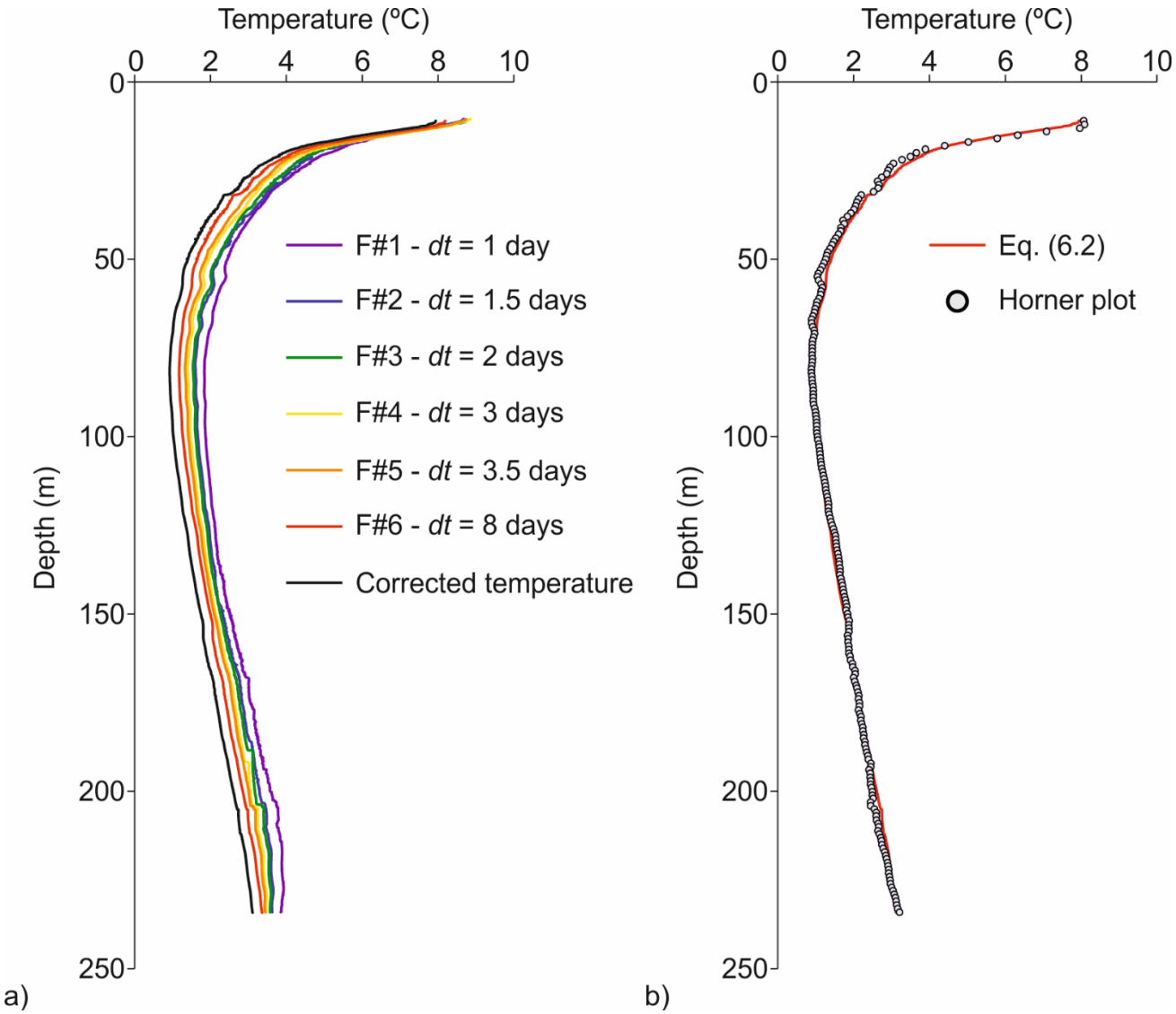

Figure 6.3. a) Measured (F#) and corrected temperature profiles and b) comparison between the equilibrium temperature retrieve from Horner's plot and **Eq.** (**6.2**).

A comparison of different drilling correction method was conducted (**Figure 6.4**) and it suggest that analytical methods such as line source (Horner method) or cylindrical source (Leblanc method) provide more reliable results than empirical methods (method A and method B) as results with analytical methods are well correlated. In fact, while the line source and cylindrical source methods only shift the profile to a cooler temperature not changing the geothermal gradient (16.5 ºC km^{-1}), the empirical methods tested increased the geothermal gradient by 10% (**Table 6.1**). Drilling correction should not alter the geothermal gradient of a temperature profile.

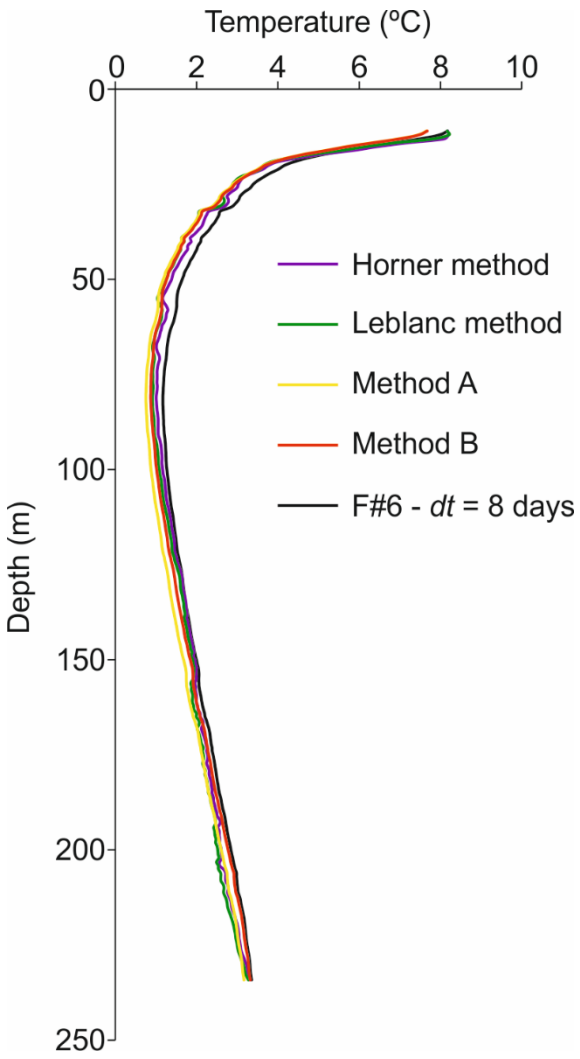

Figure 6.4. Comparison between different drilling-induced correction equations.

Table 6.1. Geothermal gradient estimated based on the different drilling-induced correction methods.

Correction method	Geothermal gradient (ºC km^{-1})
Temperature profile measured 8 days after end of drilling	16.5
Line source (Horner method)	16.5
Cylindrical source (Leblanc method)	16.5
Empirical method (method A)	18.0
Empirical method (method B)	18.1

6.2 Correction for paleoclimate-induced thermal disturbances

After correcting the temperature profile to drilling-induced thermal disturbances, it needs to be corrected for the effect of paleoclimate before the heat flux can be estimated. As **Figure 6.3a** illustrates, the temperature profile measured displayed a typical geothermal gradient inversion caused by climate variations.

6.2.1 Theory

Temperature logs are affected by paleoclimate events due to the downward diffusion of the surface temperature variations with larger amplitudes and duration than daily or annual cycles (e.g., Jessop, 1990). Birch (1948) developed an analytical method to correct temperature profiles for the effects of paleoclimate that was used in this work. The transient subsurface temperature disturbance resulting from a surface temperature variation in a semi-infinite solid is given by (Carslaw and Jaeger, 1959):

$$T(z,t) = \frac{z}{\sqrt{4\pi\alpha}} \int_0^t \Delta T(t') \, exp\left[-\frac{z^2}{4\alpha(t-t')}\right] (t-t')^{-\frac{3}{2}} dt' \quad \textbf{(6.9)}$$

where $\Delta T(t')$ represents the amplitude of the temperature variation and t' (s) the time interval elapsed since the disturbance. For several climate episodes, the integral in **Eq.** (**6.9**) can be break up into smaller time intervals (B_1, B_2, …, B_{n-1} and B_n) with constant amplitude, assuming a stepwise temperature change within each interval (Birch 1948). With this assumption, **Eq.** (**6.9**) becomes (Birch, 1948):

$$T(z,t) = \frac{z}{\sqrt{4\pi\alpha}} \left\{ B_1 \int_0^{t'_1} exp\left[-\frac{z^2}{4\alpha(t-t')}\right] (t-t')^{-\frac{3}{2}} dt' + \ldots + B_n \int_{t'_{n-1}}^{t'_n} exp\left[-\frac{z^2}{4\alpha(t-t')}\right] (t-t')^{-\frac{3}{2}} dt' \right\} \quad \textbf{(6.10)}$$

Considering the time of the events backward from the present and introducing the error function (*erf(x)*), then **Eq.** (**6.10**) can be simply represented by (Birch, 1948):

$$T(z,t) = B_1 \left[1 - erf\left(\frac{z}{2\sqrt{\alpha(t_2)}}\right)\right] + B_2 \left[erf\left(\frac{z}{2\sqrt{\alpha(t_1)}}\right) - erf\left(\frac{z}{2\sqrt{\alpha(t_2)}}\right)\right] + \ldots + B_n \left[erf\left(\frac{z}{2\sqrt{\alpha(t_{n-1})}}\right) - erf\left(\frac{z}{2\sqrt{\alpha(t_n)}}\right)\right] \quad \textbf{(6.11)}$$

where the subscripts 1 and 2 stand for the end and beginning of the climate episode. The effect of each climate episode is consequently added to evaluate the global temperature effect. The paleoclimate corrections consider the nowadays temperature given by climate normals as the baseline. For example, for Kuujjuaq, surface air climate normals from 1981 to 2010 transformed into ground surface climate normals suggest a baseline temperature of -1 ºC. Cold climate events such as the Quaternary glaciations and the Little Ice Age were colder than today's baseline while warm events such as the Holocene Thermal Maximum, the Roman and Medieval warm periods and the Industrial Revolution were warmer than today's baseline. Quaternary interglacial periods are assumed to have had the same temperature as today's baseline. The effect of the Quaternary glacial periods can be traced up to 10 km depth while the Holocene climatic changes can be traced up to 2 km depth (**Figure 6.5**). For this reason, shallower than 2 km depth temperature profiles should be corrected for both late Pleistocene and Holocene major climate episodes while deeper than 2 km profiles only need to be corrected for the effects of the Quaternary glaciations.

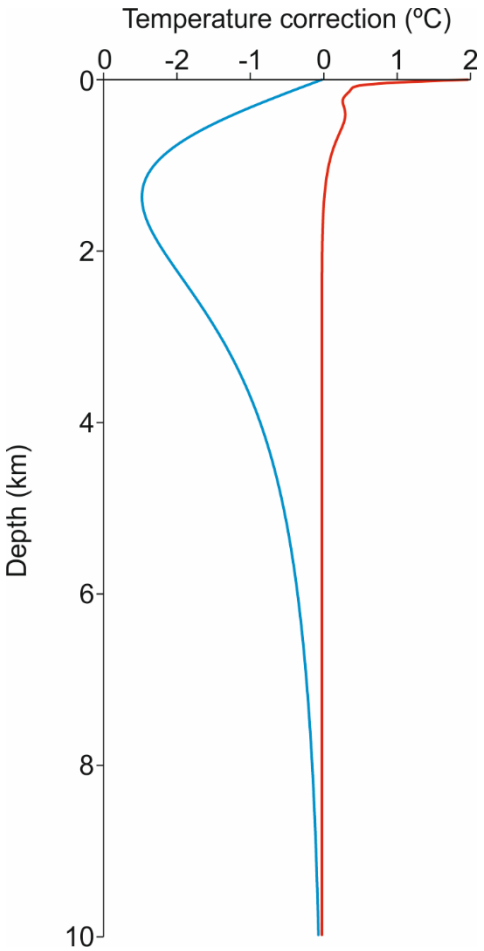

Figure 6.5. Example of subsurface temperature perturbation caused by Quaternary glacial periods (blue line) and Holocene climate events (red line).

6.2.1.1 Ground surface temperature history

The paleoclimate corrections undertaken in this work took into account not only the late Pleistocene (300-11.6 ka before present (B.P.)) climate events but the Holocene epoch (11.6-0 ka B.P.) climate substages as well. The ground surface temperature history used in this work was reconstructed on the basis of climate proxies literature information. The fourfold stratigraphic framework proposed by Flint (1947) and Emiliani (1955) to characterize the late Pleistocene glacial and interglacial episodes was assumed, i.e., Nebraskan glaciation occurred between 300 and 265 ka B.P., Aftonian interglacial between 265 and 200 ka B.P, Kansan glaciation between 200 and 175 ka B.P., Yarmouth interglacial between 175 and 125 ka B.P., Illinoian glaciation between 125 and 100 ka B.P., Sangamonian interglacial between 100 and 75 ka B.P. and Wisconsinan glaciation between 75 and 11.6 ka B.P. (**Figure 6.6**). The glacial episodes were assumed to have had the same average temperature colder than today's baseline while the interglacial periods were assumed to have had the same average temperature and equal to today's baseline (Birch, 1948; Jessop, 1990).

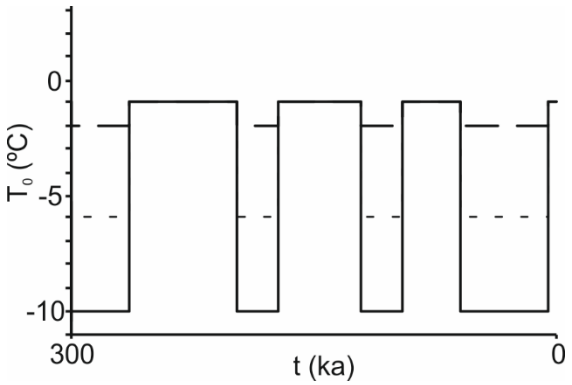

Figure 6.6. Timeline of late Pleistocene climate events (Flint, 1947; Emiliani, 1955) and temperature step (Birch, 1948; Jessop, 1990). Solid line – temperature during glacial episode assumed as 10 °C colder than today's baseline (-1 °C); pointed line – temperature during glacial episode assumed 5 °C colder than today's baseline; dashed line – temperature during glacial episode 1 °C colder than today's baseline.

Ground surface temperature history inversion from deep temperature profiles in Canada suggests an average temperature of -5 ºC during the Last Glacial Maximum (thus 5 ºC colder than today in the paleoclimate correction carried out), but lower temperatures (about -10 ºC, or 10 ºC colder than today for the paleoclimate correction) were found in eastern Canada (e.g., Sass et al., 1971; Sugden, 1977; Mareschal et al., 1999; Rolandone et al., 2003; Chouinard and Mareschal, 2009; Majorowicz et al., 2012; Majorowicz and Safanda, 2015; Pickler et al., 2016). Furthermore, during the Last Glacial Maximum, the Laurentide Ice Sheet reached a maximum thickness greater than 3 km (Peltier, 2002, 2004) and may suggest that under such thick ice the temperature was close to the freezing point (-1 to -2 ºC or 1 to 2 ºC colder than today for the paleoclimate correction; Jessop, 1971, 1990). This is supported by permafrost studies that also suggest that the base of the ice sheet above subarctic Quebec was roughly at the melting temperature (Allard and Seguin, 1987).

The Holocene epoch is composed by several substages that, contrarily to the late Pleistocene, were considered within the ground surface temperature history reconstruction. The interglacial Holocene Thermal Maximum (ca. 7-5.8 ka B.P.) is referred to have been 1-2 ºC warmer than the present-day temperature (Dahl-Jensen et al., 1998; Kaufman et al., 2004; Renssen et al., 2012; Gajewski, 2015; Richerol et al., 2016). The temperature during the interstadial Roman and Medieval warm periods (ca. 3.2-1 ka B.P.; Richerol et al., 2016) was estimated to have been 1-1.5 ºC warmer than at present (Dahl-Jensen et al., 1998). During the stadial Little Ice Age (ca. 500 – 270 years B.P.; Richerol et al., 2016), the temperature was estimated to have been 1 ºC cooler than today (Cermak, 1971; Dah-Jensen et al., 1998). Majorowicz et al. (2005) and Chouinard et al. (2007) identified a warming of about 1.4-2 ºC during the pre-Industrial and Industrial Revolution (ca. 270-80 years B.P.). This episode was followed by a short cooling period (80-30 years B.P.), where the temperature decreased around 0.4 ºC (Chouinard et al., 2007). Nowadays, atmospheric air temperature can be converted empirically to undisturbed ground surface temperature as (Ouzzane et al., 2015):

$$T_{\text{ground}} = 17.898 + 0.951 T_{\text{air}} \quad (\mathbf{6.12})$$

where temperature *T* is in K and the subscripts ground and air are used for ground surface and surface air temperature, respectively. The application of this empirical correlation to Kuujjuaq annual meteorological data (ECCC, 2022) suggests a sharp increase on the temperature of about 2 ºC for the last 30 years (**Figure 6.7**). The reference undisturbed ground surface temperature can also be inferred from the previous equation. Surface air temperature from climate normal of the 1981-2010 period (-6 ºC;

ECCC, 2022) suggests a reference ground surface temperature of -1 ºC (**Figure 6.7**). This is the temperature baseline to carry out the paleoclimate corrections.

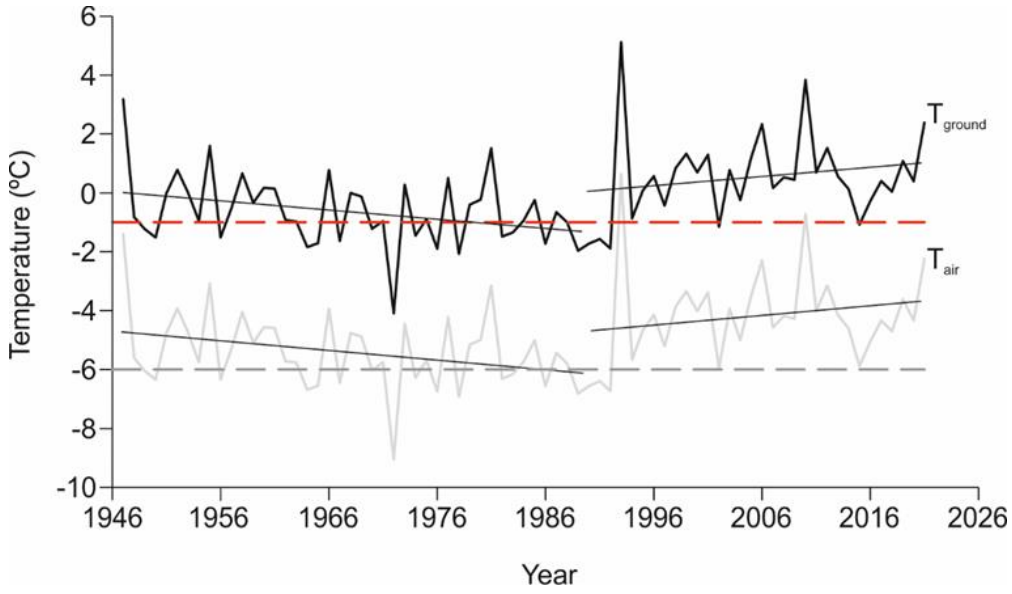

Figure 6.7. Annual average surface air and ground surface temperature in Kuujjuaq. Red dashed line – reference ground surface temperature, grey dashed line – average surface air temperature from climate normal of the 1981-2010 period.

6.2.1.2 Monte Carlo-based paleoclimate sensitivity analysis

Uncertainty is present when reconstructing ground surface temperature history and therefore paleoclimate uncertainty should be assimilated on estimates of surface heat flux (e.g., Mather et al., 2018). In this work, the global sampling and probabilistic approach were selected to account for the current uncertainty associated with climate events temperature and obtain several possible temperature profiles corrected for paleoclimate-induced thermal disturbances. A Monte Carlo-based sensitivity analysis was conducted to deal with the paleoclimate uncertainty (**Table 6.2**). This approach simulates the possible scenarios by random sampling the input variables jointly, within the defined span of the probability distribution functions. Continuous triangular probability distribution functions were used to describe the temperature distribution during glacial episodes since there is limited information about the temperature during the glacial periods (only three temperature hypotheses were found in literature). The application of a normal distribution would not make sense with such scarce temperature information (the average and standard deviation should be calculated for more than 3 temperature points). Furthermore, it is also assumed that the minimum and maximum temperature steps are the least probable and the mean value is the most probable value. This is justified by the literature information retrieved to reconstruct the ground surface temperature history. Continuous uniform probability distribution functions were used to describe the Holocene climate events assuming that the minimum and maximum values retrieved from literature have the same probability of occurrence. A single value was assumed for the interglacial periods, for the short colling period that followed the pre-Industrial and Industrial Revolution and for the present-day global warming based on the literature review. No range of possible values was found in the literature. The simulations were carried out with @RISK (Palisade, 2019) using Latin Hypercube sampling and the pseudorandom number generator Marsenne Twister. The Latin Hypercube sampling was chosen since it is referred to be more reliable and efficient than Monte Carlo sampling (Vose, 2008). A total of 1000 iterations (i.e., possible scenarios) were ran to assure output stability. This analysis allowed us to define the most likely geothermal gradient, the 50% range and the least probable values.

Table 6.2. Monte Carlo method input parameters and their uncertainty.

Epoch	Climate event	Time step (years B.P.)	Temperature step			Variable type	Distribution
			Min	Mean	Max		
Late Pleistocene	Nebraskan (glacial period)	300,000 – 265,000	-10	-5	-1	Continuous	Triang(min,mean,max)
	Aftonian (interglacial)	265,000 – 200,000		0			Single value
	Kansan (glacial period)	200,000 – 175,000	-10	-5	-1	Continuous	Triang(min,mean,max)
	Yarmouth (interglacial)	175,000 – 125,000		0			Single value
	Illinoian (glacial period)	125,000 – 100,000	-10	-5	-1	Continuous	Triang(min,mean,max)
	Sangamonian (interglacial)	100,000 – 75,000		0			Single value
	Wisconsinan (glacial period)	75,000 – 11,600	-10	-5	-1	Continuous	Triang(min,mean,max)
Holocene	Holocene (interglacial)	11,600 – 7,000		0			Single value
	Holocene Thermal Maximum	7,000 – 5,800	+1		+2	Continuous	Uniform(min,max)
	Holocene (interglacial)	5,800 – 3,200		0			Single value
	Roman & Medieval warm periods	3,200 – 1,000	+1		+1.5	Continuous	Uniform(min,max)
	Holocene (interglacial)	1,000 – 500		0			Single value
	Little Ice Age	500 – 270		-1			Single value
	Pre-Industrial & Industrial Revolution	270 – 80	+1.4		+2	Continuous	Uniform(min,max)
	Cooling period	80 – 30		-0.4			Single value
	Present-day global warming	30 – 0		+2			Single value

B.P. – before present. The temperature step is related to the nowadays ground surface temperature given by climate normals (-1 ºC for Kuujjuaq). This means that a temperature step of 0 is the same as today, -10 to -1 means 10 to 1 ºC colder than today's baseline and +1 to +2 means 1 to 2 ºC warmer than today. Glacial periods temperature from inversion of deep temperature profiles has been evaluated by Jessop (1971), Sass et al. (1971), Sugden (1977), Mareschal et al. (1999), Rolandone et al. (2003), Chouinard and Mareschal (2009), Majorowicz et al. (2012), Majorowicz and Safanda (2015) and Pickler et al. (2016). Surface temperature during the Holocene Thermal Maximum was estimated by Dahl-Jensen et al. (1998), Kaufman et al. (2004), Renssen et al. (2012), Gajewski (2015) and Richerol et al. (2016). Surface temperature during the Roman and Medieval warm periods was evaluated by Dahl-Jensen et al. (1998). Surface temperature during the Little Ice Age was estimated by Cermak (1971) and Dah-Jensen et al. (1998). Surface temperature during the pre-Industrial and Industrial Revolution was evaluated by Majorowicz et al. (2005) and Chouinard et al. (2007). The short cooling period that followed the pre-Industrial and Industrial Revolution was noted by Chouinard et al. (2007). The present-day global warming was estimated based on annual meteorological data (**Figure 6.5**).

6.2.2 Results

The paleoclimate corrections with Monte Carlo simulations applied to the temperature profile previously corrected for the drilling-induced thermal disturbances resulted in the temperature profiles displayed in **Figure 6.8**. The results indicate an increase of 15-29% of the geothermal gradient (**Table 6.3**). Furthermore, the geothermal gradient values within the 50% probability interval are found to range between 20.4 and 21.8 ºC km^{-1}, with a most probable value of 20.9 ºC km^{-1}. The extreme minimum and maximum values for the geothermal gradient are 19.3 and 23.3 ºC km^{-1}, respectively, corresponding to the least probable values.

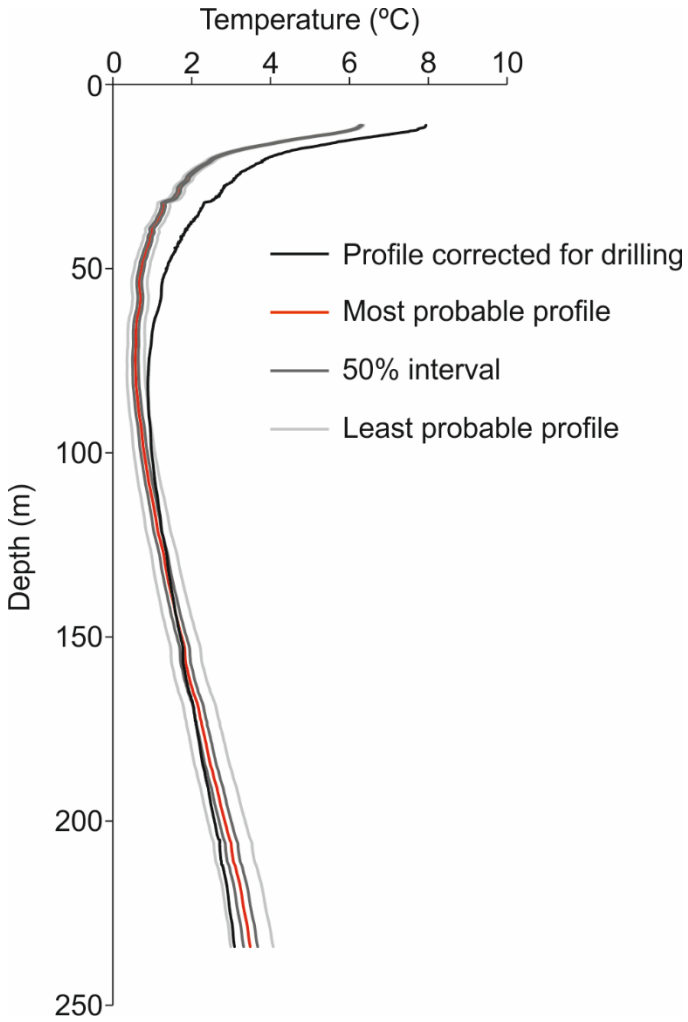

Figure 6.8. Temperature profile corrected for drilling- and paleoclimate-induced thermal disturbances.

Table 6.3. Geothermal gradient estimated for the different paleoclimate scenarios.

Correction method	Geothermal gradient (ºC km^{-1})
Temperature profile corrected for drilling-induced thermal disturbances	16.5
Most probable temperature profile	20.9
Temperature profiles within the 50% probability interval	20.4 – 21.8
Least probable temperature profile (minimum)	19.3
Least probable temperature profile (maximum)	23.3

6.3 Heat flux evaluation

6.3.1 Methodology

A linear increase of temperature with depth was observed for depths below 100 m and this part of the profile was used to evaluate the geothermal gradient after correcting the temperature profile for both drilling- and paleoclimate-induced thermal disturbances (**Figure 6.9**).

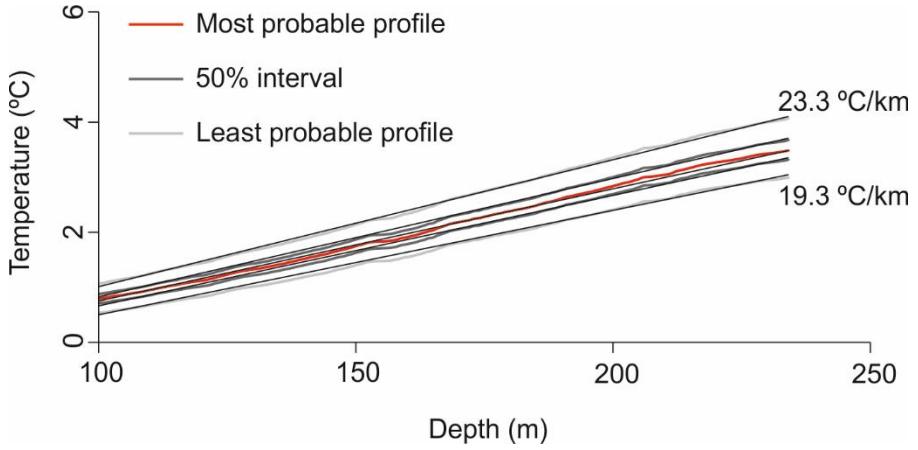

Figure 6.9. Geothermal gradient corrected for drilling- and paleoclimate-induced thermal disturbances.

Afterwards, a simple 1D form of Fourier's law was used to estimate the heat flux taking into account the geothermal gradient and the thermal conductivity of the geological materials:

$$q_0 = -\lambda \nabla T \quad (\mathbf{6.13})$$

where q_0 (W m^{-2}) is the surface heat flux, λ (W m^{-1} K^{-1}) is the thermal conductivity of the geological materials and ∇T (ºC km^{-1}) is the geothermal gradient. A Monte Carlo-based sensitivity analysis was carried out as well to consider the uncertainty of both thermal conductivity and geothermal gradient on the heat flux estimates (**Table 6.4**). A total of 1000 iterations were also running to evaluate the heat flux.

Table 6.4. Monte Carlo method input parameters and their uncertainty.

Parameter code	Parameter description	Variable type	Distribution
λ	Thermal conductivity	Continuous	Triang(min,median,max)
∇T	Geothermal gradient	Continuous	Triang(min,mean,max)

The thermal conductivity distribution took into account the values evaluated in the laboratory (section **5. Thermal conductivity**) and assuming a homogeneous subsurface made of paragneiss. As previously explained the thermal conductivity range of the core (calculated using the harmonic mean) is similar to the thermal conductivity range of the paragneiss (2.4-2.8 W m^{-1} K^{-1} and 2.5-2.9 W m^{-1} K^{-1}, respectively). Thus, the thermal conductivity values used in the triangular distribution were 2.5, 2.7, 2.9 W m^{-1} K^{-1} as minimum, mean and maximum, respectively. The geothermal gradient distribution considered the least probable values as the maximum (23.3 °C km^{-1}) and the minimum (19.3 °C km^{-1}) of the triangular distribution function and the most likely value (20.9 °C km^{-1}) as the mean of the distribution.

Additionally, and in order to quantify the surface heat flux misestimation if paleoclimate is not considered, surface heat flux was evaluated assuming the uncorrected geothermal gradient, i.e., 16.5 °C km^{-1}. The same thermal conductivity values were used in this calculation (i.e., 2.5, 2.7, 2.9 W m^{-1} K^{-1} as minimum, mean and maximum, respectively).

6.3.2 Results

The increase in the geothermal gradient leads to an increase in the heat flux of 16-27%. The uncorrected heat flux considering the thermal conductivity uncertainty (varying between 2.5 and 2.9 W m^{-1} K^{-1} with a median value of 2.7 W m^{-1} K^{-1}) and the 16.5 ºC km^{-1} geothermal gradient is found to vary between 43.6 and 45.5 mW m^{-2} within a 50% probability interval (**Figure 6.10a**). The most probable value is 44.6 mW m^{-2} (**Figure 6.10a**). The extreme minimum and maximum values are 41.4 and 47.8 mW m^{-2}, respectively, corresponding to the least probable values (**Figure 6.10a**). However, when paleoclimate-adjusted geothermal gradient values are used, the heat flux is found to vary between 55.2 and 59.0 mW m^{-2} within a 50% probability interval, with a most probable value of 57.2 mW m^{-2} (**Figure 6.10b**). The extreme minimum and maximum values are found to be 49.5 and 65.5 mW m^{-2}, respectively, and corresponding to the least probable heat flux values (**Figure 6.10b**). These values correspond to the surface heat flux.

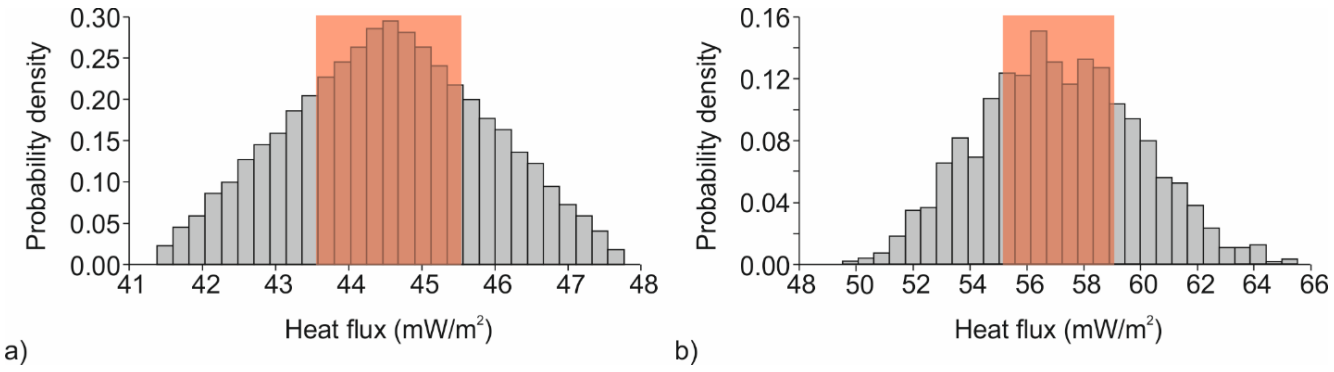

Figure 6.10. a) Uncorrected and b) corrected simulated surface heat flux. Red rectangle – 50% probability interval.

6.3.3 Discussion

The continuous temperature log measured in the Forum well permitted to re-evaluate the geothermal gradient and surface heat flux after carrying out corrections for drilling- and paleoclimate-induced thermal disturbances. The geothermal gradient corrected for the paleoclimate effects is 15-29% greater than the one evaluated from the uncorrected temperature profile. Such observation highlights the importance of correcting temperature profiles for paleoclimate-induced thermal disturbances. Neglecting

the effects of paleoclimate leads to important misestimations of the geothermal gradient and thus of the heat flux. The uncorrected geothermal gradient was 16.5 ºC km^{-1} while the corrected geothermal gradient increases to values ranging between 20.4 and 21.8 ºC km^{-1} (50% probability interval) with a most likely value of 20.9 ºC km^{-1}. These values agree with the base-case geothermal gradient scenario simulated by Miranda et al. (2020b), who suggested 20.4 and 22.6 ºC km^{-1}.

The increase in the geothermal gradient consequently leads to an increase in the heat flux of 16-27%. The uncorrected heat flux is found to vary between 43.6 and 45.5 mW m^{-2} (50% probability interval), with a most probable value of 44.6 mW m^{-2}. However, the corrected heat flux is found to vary between 55.2 and 59.0 mW m^{-2} (50% probability interval), with a most probable value of 57.2 mW m^{-2}. These values are greater than previous estimates for northern Quebec (40 ± 9 mW m^{-2}; Majorowicz and Minea, 2015) and for Raglan (32 mW m^{-2}; Comeau et al., 2017 and references therein), Asbestos Hill (38 mW m^{-2}; Comeau et al., 2017 and references therein) and Coulon (28 mW m^{-2}; Comeau et al., 2017 and references therein) – the only heat flow measurement points in Nunavik. This suggests that the geothermal potential of Kuujjuaq is greater than previously estimated. Furthermore, this new re-assessment of the surface heat flux in Kuujjuaq is fairly similar to the base-case heat flux scenario simulated by Miranda et al. (2021a) – 53 mW m^{-2}. However, it is also important to highlight the key role played by the ground surface temperature history uncertainty in these estimates. Further studies are envisioned to attempt to infer the ground surface temperature history from the measured temperature log and define more accurately the ground surface temperature history of at least the last hundred years. It is also important to mention that the fourfold glacial chronology may be outdated (e.g., Ehlers and Gibbard, 2011; Jennings et al., 2013). For example, Nebraskan glaciation perhaps occurred 720 ka ago rather than 300 ka. Also, the temperature during the interglacial periods may have been warmer than today's baseline. This may have an impact on the geothermal gradient that has not yet been fully assessed. The paleoclimate literature review initiated by Miranda (2021) can be further improved attempting to update the late-Pleistocene glacial periods.

7. GENERAL DISCUSSION

A preliminary evaluation of the deep geothermal energy potential of Kuujjuaq and the techno-economic feasibility of Enhanced Geothermal Systems (EGS) for both space heating and electricity generation permitted to draw some conclusions that were compiled in a SWOT analysis (Table 7.1).

Table 7.1. SWOT analysis based on Miranda (2021) research study.

SWOT	Conclusions
Strengths	• Estimated thermal energy in place can meet Kuujjuaq's estimated average heat demand (37 GWh) at a depth of 4 to 5 km • EGS may provide heating at lower cost than the oil furnaces
Weaknesses	• Large uncertainty associated with subsurface temperature • Large uncertainty associated with stress regime • Large uncertainty associated with subsurface behavior during hydraulic stimulation • Large uncertainty associated with recovery factor
Opportunities	• Electricity and cogeneration may be possible at a depth greater than 6 km • Electricity and cogeneration may be possible at shallower depth if the subsurface temperature is near its maximum estimated value (167 ºC at 4 km) • EGS may provide power at lower cost than the diesel power plant
Threats	• No deep geothermal potential if the worst-case temperature scenario simulated prevails (28 ºC at 4 km) • Greater fluid overpressure is needed for an effective stimulation treatment (> 20 MPa at 4 km) • Capital cost (38 to 122 M$)

Overall, geothermal energy seems a viable alternative for off-grid northern communities and further gathering of information and geothermal studies are worthwhile to reduce the uncertainties found. One of such important uncertainties was related to the subsurface temperature. This parameter plays a major role on the viability of a deep geothermal system. Therefore, the present work aimed at reducing the subsurface temperature uncertainty by re-evaluating the geothermal gradient and the surface heat flux in Kuujjuaq.

This new data acquired supports the work previously undertaken to assess the deep geothermal energy source potential of Kuujjuaq. The new heat flux data suggests that the base-case scenario evaluated by Miranda et al. (2021a) prevails in Kuujjuaq. Thus, the temperature of the reservoir is within the 50% percentile of Miranda et al. (2020b; **Figure 7.1-7.2**). This supports geothermal heat production as a low to medium risk application at a depth of 3-4 km, while geothermal electricity generation seems a high to medium risk application at a depth shallower than 7 km.

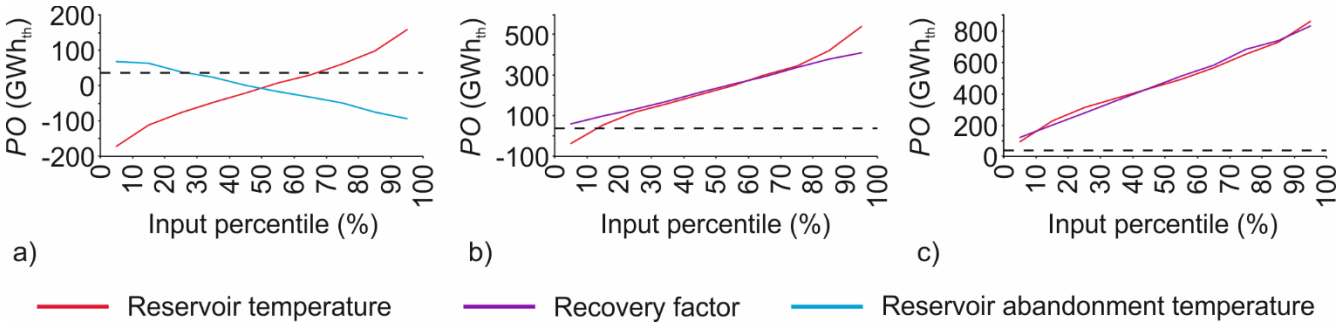

Figure 7.1. Annual geothermal heat output potential as a function of the uncertain parameters' percentile at a) 2 km depth, b) 3 km depth and c) 4 km depth (Miranda et al., 2020b). Dashed line – Kuujjuaq's estimated heating demand of 37 GWh.

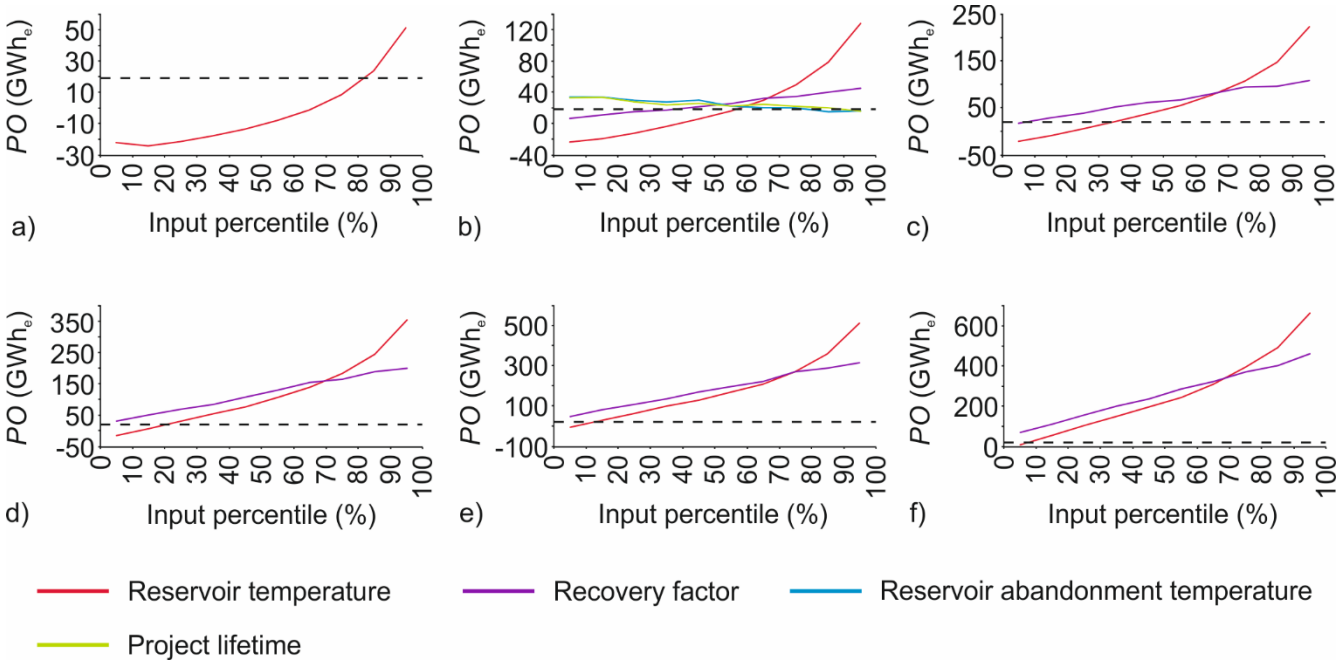

Figure 7.2. Annual geothermal power output potential as a function of the uncertain parameters' percentile at a) 5 km depth, b) 6 km depth, c) 7 km depth, d) 8 km depth, e) 9 km depth and f) 10 km depth (Miranda et al., 2020b). Dashed line – Kuujjuaq's estimated electricity demand of 18.9 GWh.

Given the estimated geothermal gradient, the technological and economic analysis undertaken by Miranda et al. (2021b) was narrowed. The simulated energy extracted with an EGS at 4 km depth is capable to fulfil the community's heating needs (**Figure 7.2**). The most likely levelized cost of energy of an EGS in Kuujjuaq can range between 83-91 and 178-205 \$ MWh^{-1}, depending on the necessary flow rate and thermal energy harvested to meet the community's needs (**Figure 7.3**). Such estimates suggest that EGS can have commercial interest for Kuujjuaq given the current heating energy cost of 190 \$ MWh^{-1} with oil furnaces. New numerical simulations and cost analysis are needed to evaluate the techno-economic feasibility of generating electricity with EGS at 7 km depth.

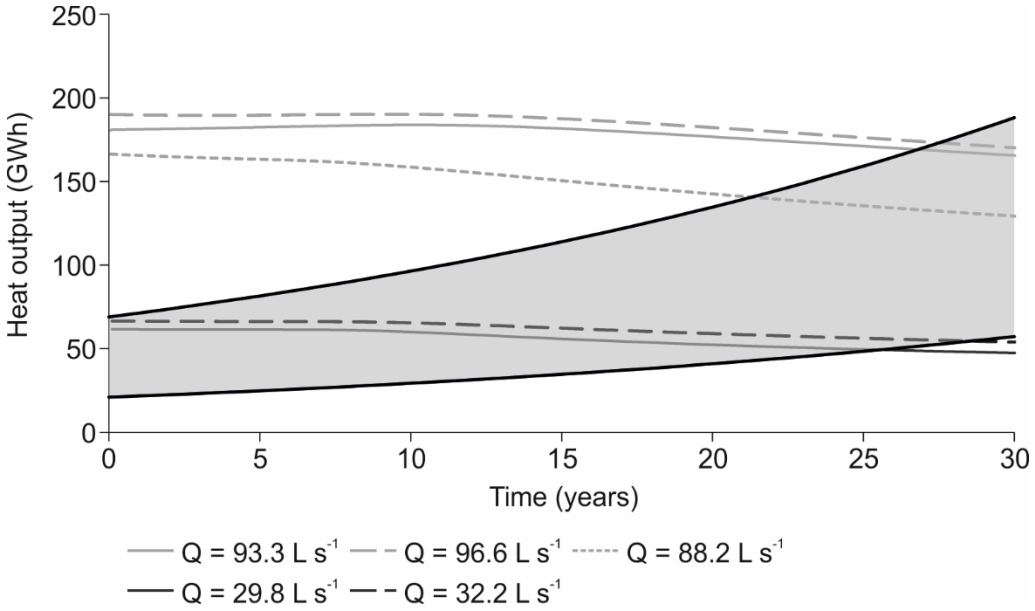

Figure 7.3. Heating energy produced (color lines) and projected demand (grey polygon) with an EGS in Kuujjuaq (Miranda et al., 2021b). Q = 93.3 L s^{-1}, 96.6 L s^{-1} and 88.2 L s^{-1} – scenario where wells are located parallel to the maximum horizontal principal stress and perpendicular to the fault trace, the fracture size is x10 longer than measured in the field and the fault aperture is 0.10 m (93.3 L s^{-1}), 0.01 m (96.6 L s^{-1}) and 0.001 m (88.2 L s^{-1}). Q = 29.8 L s^{-1} and 32.2 L s^{-1} – scenario where wells are located perpendicular to the maximum horizontal principal stress and parallel to the fault trace, the fracture size is x10 longer than measured in the field and the fault aperture is 0.10 m (29.8 L s^{-1}) and 0.01 m (32.2 L s^{-1}).

Table 7.2. Levelized cost of energy for each simulated design (Miranda et al., 2021b).

Design			Levelized cost of energy ($ MWh^{-1}) Heat		
			Optimistic	Likely	Pessimistic
Configuration A	Base-case	Q = 93.3	111	195	453
		Q = 96.6	114	205	475
		Q = 88.2	102	178	410
Configuration B	Base-case	Q = 29.8	54	83	170
		Q = 32.2	58	91	192

Configuration A – wells placed parallel to the maximum horizontal principal stress and perpendicular to the fault trace, configuration B – wells placed perpendicular to the maximum principal stress and parallel to the fault trace, base-case – base-case scenario for the properties of the medium.

Beyond the data presented in this report, other laboratory analyses are underway to evaluate the whole-rock geochemistry, the mineralogical composition, the radiogenic elements, the geomechanical properties and the magnetic susceptibility. Laboratory analyses with transient plane source and guarded heat flow meter are also planned and ongoing to evaluate thermal conductivity, thermal diffusivity and heat capacity at temperatures ranging from -10 to 180 ºC. All these laboratory analyses will be used to keep improving the estimate of Kuujjuaq deep geothermal potential and the techno-economic viability of EGS in Kuujjuaq. The development of an online database is also foreseen.

8. CONCLUDING REMARKS

Deep geothermal energy systems, such as EGS, can be a viable alternative to offset diesel consumption in off-grid communities. However, assessing the technical feasibility of such systems is intimately related with the subsurface geology and temperature and thermo-hydro-mechanical properties of the deep-seated rocks. Although still subject to uncertainty, the analysis and interpretation of the 234-m-deep well core provided important geological and thermal information that was lacking in previous studies:

- Paragneiss is the dominant lithology and is intersected by minor intrusions of mafic (diorite/gabbro) and felsic (tonalite/granite/granitoid) intrusive rocks.

- The average natural fractures intensity evaluated along the core is 0.96 fractures m^{-1} for a borehole that had a depth of 234 m.

- The presence of both inclined and horizontal natural fractures may suggest a reverse/strike-slip stress regime.

- The average thermal conductivity of the paragneiss samples is 2.5 – 2.9 W m^{-1} K^{-1}.

- The average thermal conductivity of the diorite/gabbro samples is 1.9 – 2.4 W m^{-1} K^{-1}.

- The geothermal gradient ranges between 20.4 and 21.8 ºC km^{-1} (50% probability interval) with a most likely value of 20.9 ºC km^{-1}.

- The heat flux varies between 55.2 and 59.0 mW m^{-2} (50% probability interval), with a most probable value of 57.2 mW m^{-2}.

The newly obtained results in this work are helping to improve and advance research on the deep geothermal energy potential of Kuujjuaq and on the feasibility of a deep geothermal energy system to offset diesel consumption in remote northern regions. In fact, the newly obtained results support geothermal heat production as a low to medium risk application at a depth of 4-5 km, while geothermal electricity generation seems a high to medium risk application at a depth shallower than 6 km. Furthermore, an EGS in Kujjuaq to provide space heating to the community seems to have commercial interest given the current heating energy cost of 190 \$ MWh^{-1} with oil furnaces. The most likely LCOE can range between 83 to 205 \$ MWh^{-1}.

Further envisioned work is the numerical re-evaluation of the heat flux to obtain more reliable heat flow estimates than the analytical method can provide. Furthermore, the fracture information collected together with new thermo-hydro-mechanical laboratory analyzes are helpful to re-assess the technical feasibility of EGS in Kuujjuaq and improve the estimates previously carried out. Magnetic susceptibility analyses are also planned to evaluate if magnetic geophysical methods can be applied to help define the subsurface geology at a larger scale and presence of faults.

If the community of Kuujjuaq decides to proceed with further exploration of its deep geothermal resources, we believe that drilling of a 1000-m-deep exploratory borehole is the next step to achieve.

This borehole should aim at collecting further information on the thermo-hydraulic state and properties of the underground but also on the structural and stress regime prevailing at depth.

REFERENCES

Agemar, T., 2022. Bottom hole temperature correction based on empirical correlation. Geothermics 99: 102296. https://doi.org/10.1016/j.geothermics.2021.102296

Allard, M., Seguin, M.K., 1987. Le pergélisol au Québec nordique : bilan et perspectives. Géographie physique et Quaternaire 41(1): 141-152.

Allis, R., Gwynn, M., Hardwick, C., Moore, J., 2018. The Challenge of Correcting Bottom-Hole Temperatures – An Example from FORGE 58-32, near Milford, Utah. Proceedings, 43rd Workshop on Geothermal Reservoir Engineering (Stanford, CA, US, February 12-14, 2018)

Andrews, B.J., Roberts, J.J., Shipton, Z.K., Bigi, S., Tartarello, M.C., Johnson, G., 2019. How do we see fractures? Quantifying subjective bias in fracture data collection. Solid Earth 10: 487-516. https://doi.org/10.5194/se-10-487-2019

Ascencio, F., Samaniego, F., Rivera, J., 2006. Application of a spherical-radial heat transfer model to calculate geothermal gradients from measurements in deep boreholes. Geothermics 35(1): 70-78. https://doi.org/10.1016/j.geothermics.2005.10.003

Bédard, K., Comeau, F.-A., Millet, E., Raymond, J., Malo, M., Gloaguen, E., 2016. Évaluation des ressources géothermiques du bassin des Basses-Terres du Saint-Laurent. Rapport de recherche 1659, Institut national de la recherche scientifique : Quebec (QC), Canada, 100 p.

Birch, A.F., 1948. The effects of Pleistocene climatic variations upon geothermal gradients. American Journal of Science 246(12): 729-760.

Carslaw, H.S., Jaeger, J.C., 1959. Conduction of Heat in Solids. Claredon Press, Oxford, 520 p.

Cermak, V., 1971. Underground temperature and inferred climatic temperature of the past millennium. Palaeogeography, Palaeoclimatology, Palaeoecology 10: 1-19. https://doi.org/10.1016/0031-0182(71)90043-5

Chang, S.-H., Lee, C.-I., Jeon, S., 2002. Measurement of rock fracture toughness under modes I and II and mixed-mode conditions by using disc-type specimens. Engineering Geology 66(1-2): 79-97. https://doi.org/10.1016/S0013-7952(02)00033-9

Chouinard, C., Fortier, R., Mareschal, J.-C., 2007. Recent climate variations in the subarctic inferred from three borehole temperature profiles in northern Québec, Canada. Earth and Planetary Science Letters 263: 355-369. https://doi.org/10.1016/j.epsl.2007.09.017

Chouinard, C., Mareschal, J.-C., 2009. Ground surface temperature history in southern Canada: temperatures at the base of the Laurentide ice sheet and during the Holocene. Earth and Planetary Science Letters 227(1-2): 280-289. https://doi.org/10.1016/j.epsl.2008.10.026

Climate Atlas of Canada (2019) Heating Degree Days. https://climateatlas.ca/map/canada/hdd_2060_85# (Accessed April 13, 2022).

Comeau, F.-A., Raymond, J., Malo, M., Dezayes, C., Carreau, M., 2017. Geothermal potential of northern Québec: a regional assessment. GRC Transactions 41: 1076-1094.

Dahl-Jensen, D., Mosegaard, K., Gundestrup, N., Clow, G.D., Johnsen, S.J., Hansen, A.W., Balling, N., 1998. Past temperatures directly from the Greenland Ice Sheet. Science 282(5387): 268-271.

Davis, D.W., Simard, M., Hammouche, H., Bandyayera, D., Goutier, J., Pilote, P., Leclerc, F., Dion, C., 2014. Datations U-Pb effectuées dans les provinces du Supérieur et de Churchill en 2011-2012. University of Toronto, RP 2014-05, Ministère des Ressources naturelles: Québec (QC), Canada, 62 p.

Davis, D.W., Moukhsil, A., Lafrance, I., Hammouche, H., Goutier, J., Pilote, P., Talla Takam, F., 2015. Datations U-Pb dans les provinces du Supérieur, de Churchill et de Grenville effectuées au JSGL en 2012-2013. RP 2014-07, Ministère des Ressources naturelles: Québec (QC), Canada, 56 pages.

Dezayes, C., Lerouge, C., Innocent, C., Lach, P., 2021. Structural control on fluid circulation in a graben system: Constraints from the Saint Pierre Bois quarry (Vosges, France). Journal of Structural Geology 146: 104323. https://doi.org/10.1016/j.jsg.2021.104323

ECCC - Environment and Climate Change Canada, 2022. Historical Climate Data. https://climate.weather.gc.ca/ (Accessed April 26, 2022)

Ehlers, J., Gibbard, P., 2011. Quaternary Glaciation. Singh VP, Singh P. & Haritashya UK (Eds.) Encyclopedia of Snow, Ice and Glaciers, Springer, Netherlands, pp. 873-882.

Emiliani, C., 1955. Pleistocene temperatures. The Journal of Geology 63(6): 538-578. https://doi.org/10.1126/science.282.5387.268

Flint, R.F., 1947. Glacial geology and the Pleistocene epoch. John Wiley & Sons, Inc., New York, 616 p.

Förster, A., 2001. Analysis of borehole temperature data in the Northeast German Basin: continuous logs versus bottom-hole temperatures. Petroleum Geoscience 7(3): 241-254. https://doi.org/10.1144/petgeo.7.3.241

Gajewski, K., 2015. Quantitative reconstruction of Holocene temperatures across the Canadian Arctic and Greenland. Global and Planetary Change 128: 14-23. https://doi.org/10.1016/j.gloplacha.2015.02.003 Giordano, N., Kanzari, I., Miranda, M.M., Dezayes, C., Raymond, J., 2018. Underground thermal energy storage in subarctic climates: a feasibility study conducted in Kuujjuaq (QC, Canada). IGSHPA. (Stockholm, Sweden, Sept 18-20, 2018).

Géotherma solutions inc, 2022. Thermal response test and assessment of the shallow geothermal potential at the Kuujjuaq Forum, Nunavik, QC. Deliverable 3 – Final report DRAFT, Géotherma solutions inc.: Quebec (QC), 29 p.

Girard, R., 1995. Géologie de la région du lac Deborah, Territoire-du-Nouveau-Québec. MB 95-20, Ministère des Ressources naturelles: Québec (QC), Canada, 186 p.

Godet, A., Guilmette, C., Labrousse, L., Smit, M.A., Davis, D.W., Raimondo, T., Vanier, M.-A., Charette, B., Lafrance, I., 2020. Contrasting P-T-t paths reveal a metamorphic discontinuity in the New Quebec Orogen: Insights into Paleoproterozoic orogenic processes. Precambrian Research, 342: 105675. https://doi.org/10.1016/j.precamres.2020.105675

Gold, D.P., 1962. Rapport préliminaire sur la région de la baie opes Advance, Nouveau-Québec. RP 442, Ministère des Ressources naturelles: Québec (QC), Canada, 13 pages, 1 plan.

Goutorbe, B, Lucazeau, F., Bonneville, A., 2007. Comparison of several BHT correction methods: a case study on an Australian data set. Geophysics Journal International 170(2): 913-922. https://doi.org/10.1111/j.1365-246X.2007.03403.x

Gunawan, E., Giordano, N., Jensson, P., Newson, J., Raymond, J., 2020. Alternative heating systems for northern remote communities: techno-economic analysis of ground-coupled heat pumps in Kuujjuaq, Nunavik, Canada. Renewable Energy 147(1): 1540-1553. https://doi.org/10.1016/j.renene.2019.09.039

Hydro Québec, 2019. Rate DN. http://www.hydroquebec.com/residential/customer-space/rates/rate-dn.html (Accessed March 3, 2021).

Jennings, C.E., Aber, J.S., Balco, G., Barendregt, R., Bierman, P.R., Rovey, C.W., Roy, M., Thorleifson, L.H., Mason, J.A., 2013: Mid-Quaternary in North America. Elias S & Mock C (Eds.) Encyclopedia of Quaternary Science, Elsevier Science, Netherlands, pp. 180-186.

Jessop, A.M., 1971. The distribution of glacial perturbation of heat flow in Canada. Canadian Journal of Earth Sciences 8: 162-166. https://doi.org/10.1139/e71-012

Jessop, A.M., 1990. Thermal Geophysics. Elsevier, Amsterdam, 304 p.

Karanasios, K., Parker, P., 2016. Recent developments in renewable energy in remote aboriginal communities, Québec, Canada. Paper in Canadian Economic Development 16: 98-108.

Kaufman, D.S., Ager, T.A., Anderson, N.J., Anderson, P.M., Andrews, J.T., Bartlein, P.J., Brubaker, L.B., Coats, L.L., Cwynar, L.C., Duvall, M.L., Dyke, A.S., Edwards, M.E., Eisner, W.R., Gajewski, K., Geirsdóttir, A., Hu, F.S., Jennings, A.E., Kaplan, M.R., Kerwin, M.W., Lozhkin, A.V., MacDonald, G.M., Miller, G.H., Mock, C.J., Oswald, W.W., Otto-Bliesner, B.L., Porinchu, D.F., Rühland, K., Smol, J.P., Steig, E.J., Wolfe, B.B., 2004. Holocene thermal maximum in the western Arctic (0-180 ºW). Quaternary Science Reviews 23(5-6): 529-560. https://doi.org/10.1016/j.quascirev.2003.09.007

KRG - Kativik Regional Government, 2021. Community Maps. https://www.krg.ca/en-CA/map/community-maps (Accessed April 26, 2022)

KRG - Kativik Regional Government & Makivik Corporation, 2010. Plan Nunavik. Avataq Cultural Institute, Québec, 469 p.

Kulander, B.R., Dean, S.L., Ward, Jr, B.J., 1990. Fractured Core Analysis: Interpretation, Logging, and Use of Natural and Induced Fractures in Core. American Association of Petroleum Geologists: Tulsa (OK), USA, 85 pp.

Kutasov, I.M., Eppelbaum, L.V., 2005. Determination of formation temperature from bottom-hole temperature logs – a generalized Horner method. Journal of Geophysics and Engineering 2: 90-96. https://doi.org/10.1088/1742-2132/2/2/002

Kutasov, I.M., Eppelbaum, L.V., 2010. A new method for determining the formation temperature from bottom-hole temperature logs. Journal of Petroleum and Gas Engineering 1(1): 001-008.

Lafrance, I., Simard, M., Bandyayera, D., 2014. Géologie de la région du lac Saffray (SNRC 24G-24F), RG 2014-02. Ministère des Ressources naturelles : Québec (QC), Canada, 49 p.

Lafrance, I., Vanier, M.-A., Charrette, B., 2020. Baleine lithotectonic domain, Southeastern Churchill Province, Nunavik, Quebec, Canada: Geological synthesis. BG 2020-07. https://gq.mines.gouv.qc.ca/bulletins-geologiques_en/churchill_en/baleine_en/ (Accessed March 3, 2022).

Leblanc, Y., Lam, H.L., Pascoe, J., Jones, F.W., 1982. A comparison of two methods of estimating static formation temperature from well logs. Geophysical Prospecting 30(3): 348-357. https://doi.org/10.1111/j.1365-2478.1982.tb01311.x

Lorenz, J.C., Cooper, S.P., 2018. Atlas of Natural and Induced Fractures in Core. John Wiley & Sons Ltd: Oxford, UK, 324 pp.

Majorowicz, J.A., Skinner, W.R., Safanda, J., 2005. Ground surface warming history in Northern Canada inferred from inversions of temperature logs and comparison with other proxy climate reconstructions. Pure and Applied Geophysics 162: 109-128. https://doi.org/10.1007/s00024-004-2582-6

Majorowicz, J., Gosnold, W., Gray, A.L., Safanda, J., Klenner, R., Unsworth, M., 2012. Implications of post-glacial warming for northern Alberta heat flow-correcting for the underestimate of the geothermal potential. GRC Transactions 36: 693-698.

Majorowicz, J., Safanda, J., 2015. Effect of postglacial warming seen in high precision temperature log deep into the granites in NE Alberta. International Journal of Earth Sciences 104: 1563-1571. https://doi.org/10.1007/s00531-014-1075-9

Majorowicz, J.A., Minea, V., 2015. Shallow and deep geothermal energy potential in low heat flow/cold climate environment: northern Québec, Canada, case study. Environmental Earth Sciences 74: 5233-5244. https://doi.org/10.1007/s12665-015-4533-1

Makivik Corporation, 2018. Rise in the Cost of Gasoline. https://www.makivik.org/rise-in-the-cost-of-gasoline/ (Accessed March 3, 2022).

Mareschal, J.-C., Rolandone, F., Bienfait, G., 1999. Heat flow variations in a deep borehole near Sept-Îles, Québec, Canada: paleoclimatic interpretation and implications for regional heat flow

estimates. Geophysical Research Letters 26(14): 2049-2052. https://doi.org/10.1029/1999GL900489

Mather, B., Farrell, T., Fullea, J., 2018. Probabilistic surface heat flow estimates assimilating paleoclimate history: new implications for the thermochemical structure of Ireland. Journal of Geophysical Research: Solid Earth 123: 10951-10967. https://doi.org/10.1029/2018JB016555

MERN, 2020. Systéme d'information géominière du Québec. https://sigeom.mines.gouv.qc.ca/signet/classes/I1108_afchCarteIntr (Accessed March 3, 2022)

Miranda, M.A.M., 2014. Propriedades termofisicas em rochas graniticas: o caso da sondagem profunda em Almeida (Guarda, Portugal central). Thesis, MSc in Geosciences, University of Coimbra, Portugal, 122 p.

Miranda, M.A.M., 2021. Assessment of the deep geothermal energy source potential in remote northern regions: A study undertaken in the subarctic off-grid community of Kuujjuaq, Nunavik, Canada. Thesis, PhD in Earth Sciences, Institut national de la recherche scientifique, Quebec, Canada, 438 p. https://espace.inrs.ca/id/eprint/12056

Miranda, M.M., Giordano, N., Raymond, J., Pereira, A.J.S.C., Dezayes, C., 2020a. Thermophysical properties of surficial rocks: a tool to characterize geothermal resources of remote northern regions. Geothermal Energy 8: 4. https://doi.org/10.1186/s40517-020-0159-y

Miranda, M.M., Raymond, J., Dezayes, C., 2020b. Uncertainty and risk evaluation of deep geothermal energy source for heat production and electricity generation in remote northern regions. Energies 13(16): 4221. https://doi.org/10.3390/en13164221

Miranda, M.M., Raymond, J., Willis-Richards, J., Dezayes, C., 2021b. Are engineered geothermal energy systems a viable solution for arctic off-grid communities? A techno-economic study. Water 13(24): 3526. https://doi.org/10.3390/w13243526

Miranda, M.M., Velez Marquez, M.I., Raymond, J., Dezayes, C., 2021a. A numerical approach to infer terrestrial heat flux from shallow temperature profiles in remote northern regions. Geothermics 93: 102064. https://doi.org/10.1016/j.geothermics.2021.102064

Miranda, M.M., Raymond, J., Dezayes, C. Estimating theoretical stress regime for engineered geothermal energy systems in an arctic community (Kuujjuaq, Canada). Submitted Comptes Rendus Geosciences.

Ouzzane, M., Eslami-Nejad, P., Badache, M., Aidoun, Z., 2015. New correlations for the prediction of the undisturbed ground temperature. Geothermics 53: 379-384. https://doi.org/10.1016/j.geothermics.2014.08.001

Palisade, 2019. @RISK. https://www.palisade.com/risk/default.asp (Accessed March 3, 2022).

Peltier, W.R., 2002. Global glacial isostatic adjustament: palaeogeodetic and space-geodetic tests of the ICE-4G (VM2) model. Journal of Quaternary Science 17(5-6): 491-510. https://doi.org/10.1002/jqs.713

Peltier, W.R., 2004. Global glacial isostasy and the surface of the ice-age Earth: The ICE-5G (VM2) model and GRACE. Annual Review of Earth and Planetary Sciences 32: 111-149. https://doi.org/10.1146/annurev.earth.32.082503.144359

Pickler, C., Beltrami, H., Mareschal, J.-C., 2016. Laurentide Ice Sheet basal temperatures during the last glacial cycle as inferred from borehole data. Climate of the Past 12: 1-13. https://doi.org/10.5194/cp-12-115-2016

Popov, Y.A., Pribnow, D.F.C., Sass, J.H., Williams, C.F., Burkhardt, H., 1999. Characterization of rock thermal conductivity by high-resolution optical scanning. Geothermics 28: 253-276. https://doi.org/10.1016/S0375-6505(99)00007-3

Popov, Y., Beardsmore, G., Clauser, C., Roy, S., 2016. ISRM suggested methods for determining thermal properties of rocks from laboratory tests at atmospheric pressure. Rock Mechanics and Rock Engineering 49: 4179-4207. https://doi.org/10.1007/s00603-016-1070-5

Renssen, H., Seppä, H., Crosta, X., Goose, H., Roche, D.M., 2012. Global characterization of the Holocene Thermal Maximum. Quaternary Science Reviews 48: 7-19. https://doi.org/10.1016/j.quascirev.2012.05.022

Richerol, T., Fréchette, B., Rochon, A., Pienitz, R., 2016. Holocene climate history of the Nunatsiavut (northern Labrador, Canada) established from pollen and dinoflagellate cyst assemblages covering the past 7000 years. The Holocene 26(1): 44-60. https://doi.org/10.1177/0959683615596823

Rodon, T., Nachet, L., Krolik, C., Palliser, T., 2021. Building energy sovereignty through community-based projects in Nunavik. Sustainability 13(16): 9061. https://doi.org/10.3390/su13169061

Rolandone, F., Jaupart, C., Mareschal, J.-C., Gariépy, C., Bienfait, G., Carbonne, C., Lapointe, R., 2002. Surface heat flow, crustal temperatures and mantle heat flow in the Proterozoic Trans-Hudson Orogen, Canadian Shield. Journal of Geophysical Research: Solid Earth 107(B12): ETG7-1-ETG7-19. https://doi.org/10.1029/2001JB000698

Sanderson, D.J., Peacock, D.C.P., 2019. Line sampling of fracture swarms and corridors. Journal of Structural Geology 122: 27-37. https://doi.org/10.1016/j.jsg.2019.02.006

Sass, J.H., Lachenbruch, A.H., Jessop, A.M., 1971. Uniform heat flow in a deep hole in the Canadian Shield and its paleoclimatic implications. Journal of Geophysical Research 76: 8586-8596. https://doi.org/10.1029/JB076i035p08586

Schmitt, D.R., Currie, C.A., Zhang, L., 2012. Crustal stress determination from boreholes and rock cores: Fundamental principles. Tectonophysics 580: 1-26. https://doi.org/10.1016/j.tecto.2012.08.029

Schumacher, S., Moeck, I., 2020. A new method for correcting temperature log profiles in low-enthalpy plays. Geothermal Energy 8: 27. https://doi.org/10.1186/s40517-020-00181-w

Simard, M., Lafrance, I., Hammouche, H., Legouix, C., 2013. Géologie de la région de Kuujjuaq et de la Baie d'Ungava (SNRC 24J et 24K), RG 2013-04. Ministère des Ressources naturelles: Québec (QC), Canada, 60 p.

Statistics Canada, 2021. Data products, 2016 Census. www12.statcan.gc.ca/census-recensement/2016/dp-pd/index-eng.cfm (Accessed March 3, 2022).

Sugden, D.E., 1977. Reconstruction of the morphology, dynamics, and thermal characteristics of the Laurentide ice sheet at its maximum. Arctic and Alpine Research 9(1): 21-47.

UNECE—United Nations Economic Commission for Europe, 2016. Specifications for the Application of the United Nations Framework Classification for Fossil Energy and Mineral Reserves and Resources 2009 (UNFC—2009) to Geothermal Energy Resources. UNECE, Geneva, Switzerland, 28p.

Vose, D., 2008. Risk Analysis: A Quantitative Guide. John Wiley & Sons, Ltd, Chichester, 729 p.

Waldron, J., Snyder, M., 2020. Geological Structures: A Practical Introduction. University of Alberta: Edmonton (AB), Canada. https://openeducationalberta.ca/introductorystructuralgeology/ (Accessed March 3, 2022).

Yan, C., Rousse, D., Glaus, M., 2019. Multi-criteria decision analysis ranking alternative heating systems for remote communities in Nunavik. Journal of Cleaner Production 208: 1488-1497. https://doi.org/10.1016/j.jclepro.2018.10.104

Zeeb, C., Gomez-Rivas, E., Bons, P.D., Blum, P., 2013. Evaluation of sampling methods for fracture network characterization using outcrops. AAPG Bulletin 97(9): 1545-1566. https://doi.org/10.1306/02131312042

Zehnder, A.T., 2013. Modes of Fracture. In: Wang Q.J., Chung YW. (eds) Encyclopedia of Tribology. Springer, Boston, MA. https://doi.org/10.1007/978-0-387-92897-5_258

Zschocke, A., 2005. Correction of non-equilibrated temperature logs and implications for geothermal investigations. Journal of Geophysics and Engineering 2: 364-371. https://doi.org/10.1088/1742-2132/2/4/S10

APPENDIX I – WELL LOG

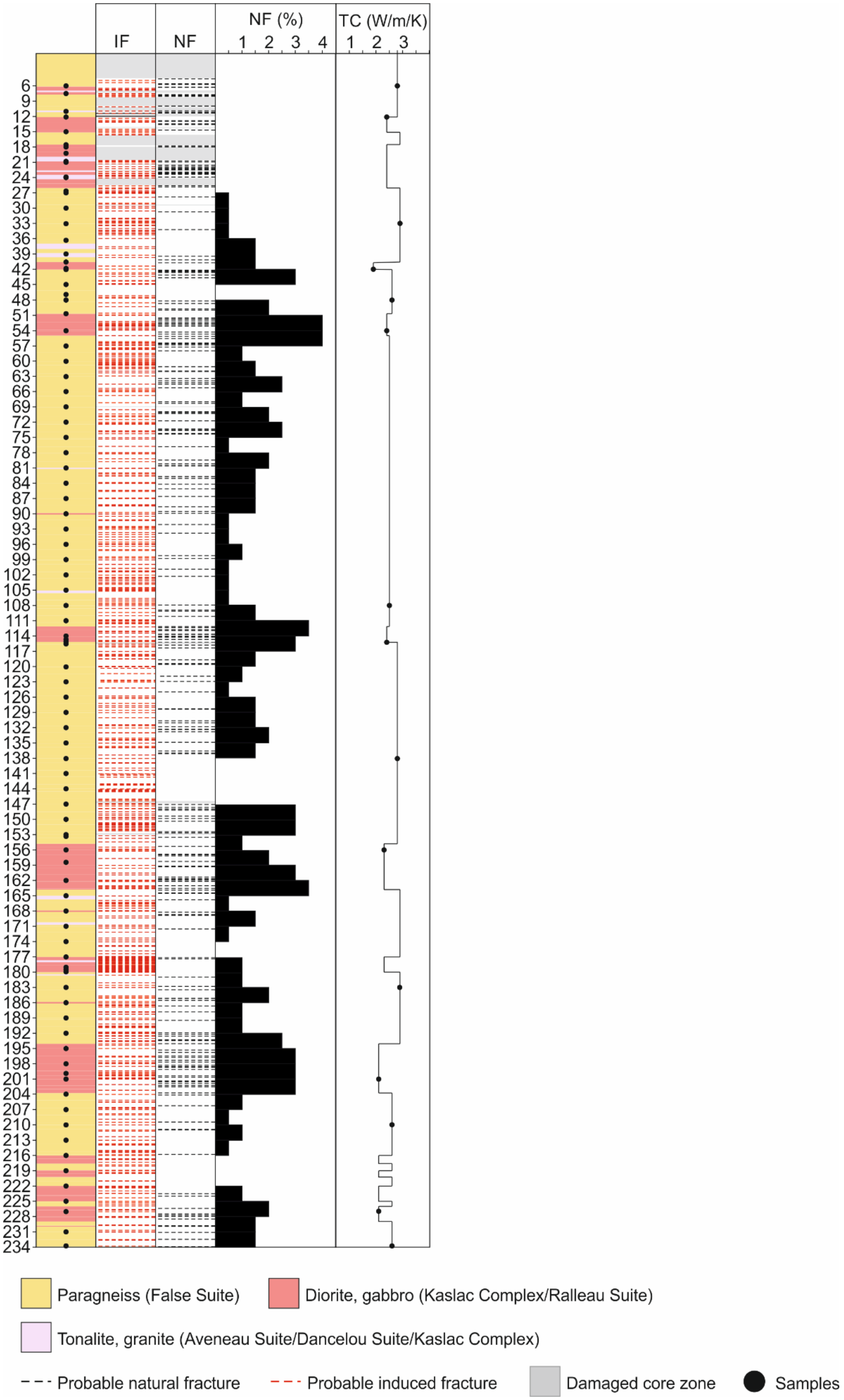

Figure A1.1. Graphical well log illustrating the lithologies observed, the stick plots produced for both induced (IF) and natural fractures (NF), the histogram displaying the natural fracture distribution (NF (%)) and the thermal conductivity profile (TC).

APPENDIX II – CORE

Figure A2.1. Core box #1 – drilling depth 6 m.

Figure A2.2. Core box #2 – drilling depth 9 m.

Figure A2.3. Core box #3.

Figure A2.4. Core box #4 – drilling depth 12 m.

Figure A2.5. Core box #5 – drilling depth 15 m.

Figure A2.6. Core box #6 – drilling depth 18 m.

Figure A2.7. Core box #7 – drilling depth 21 m.

Figure A2.8. Core box #8 – drilling depth 24 m.

Figure A2.9. Core box #9 – drilling depth 27 m.

Figure A2.10. Core box #10 – drilling depth 30 m and 33 m.

Figure A2.11. Core box #11 – drilling depth 36 m.

Figure A1.12. Core box #12 – drilling depth 39 m and 42 m.

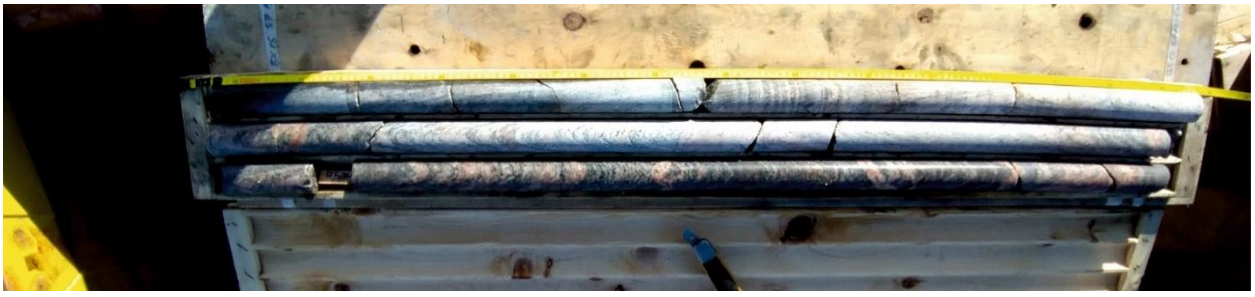

Figure A2.13. Core box #13 – drilling depth 45 m.

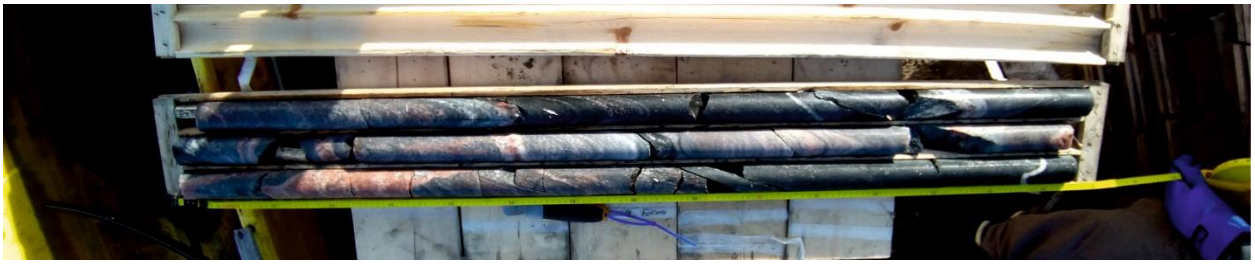

Figure A2.14. Core box #14 – drilling depth 48 m.

Figure A2.15. Core box #15 – drilling depth 54 m and 57 m.

Figure A2.16. Core box #16 – drilling depth 60 m.

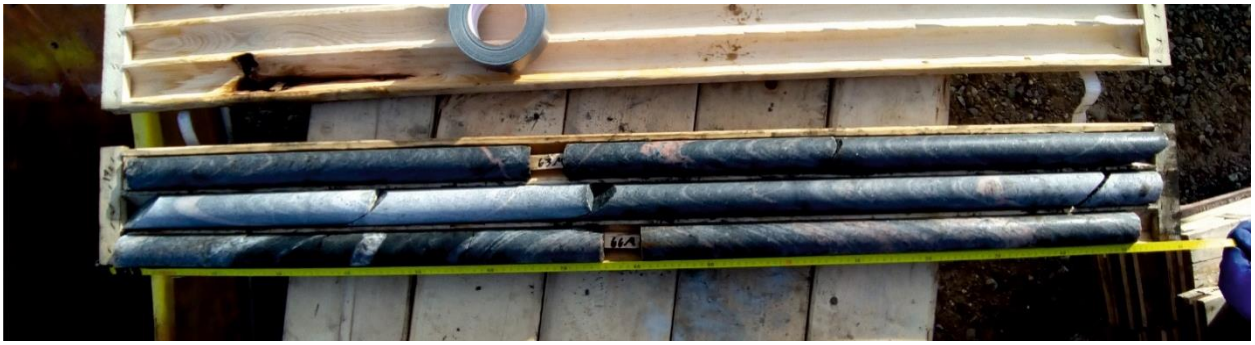

Figure A2.17. Core box #17 – drilling depth 63 m and 66 m.

Figure A2.18. Core box #18 – drilling depth 69 m.

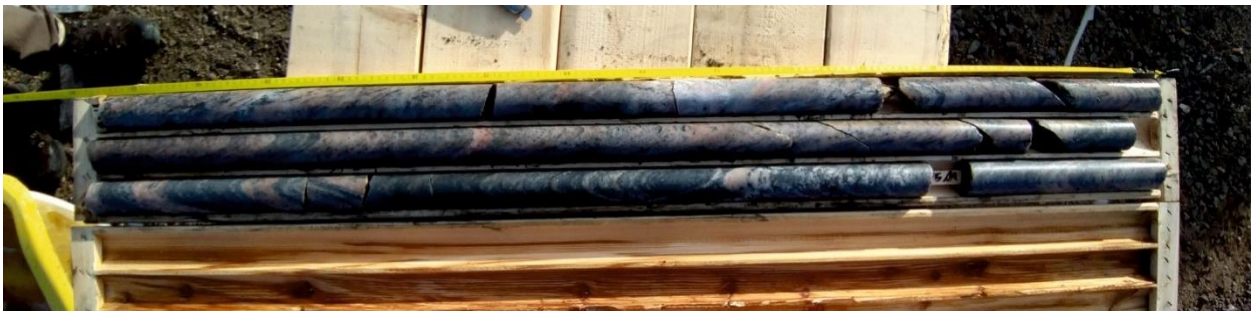

Figure A2.19. Core box #19 – drilling depth 72 m and 75 m.

Figure A2.20. Core box #20 – drilling depth 78 m.

Figure A2.21. Core box #21 – drilling depth 81 m and 84 m.

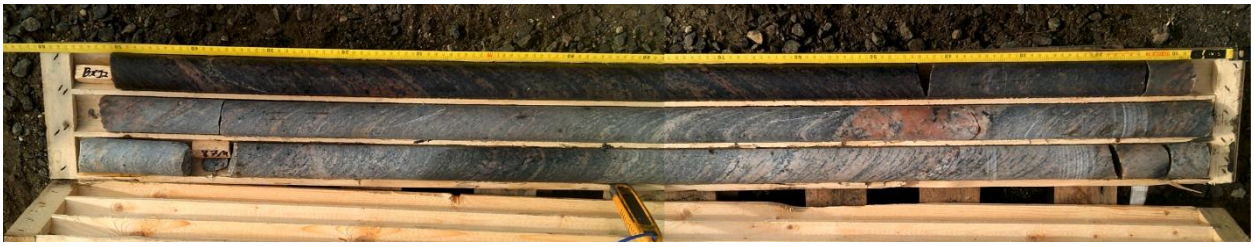

Figure A2.22. Core box #22 – drilling depth 87 m.

Figure A2.23. Core box #23 – drilling depth 90 m.

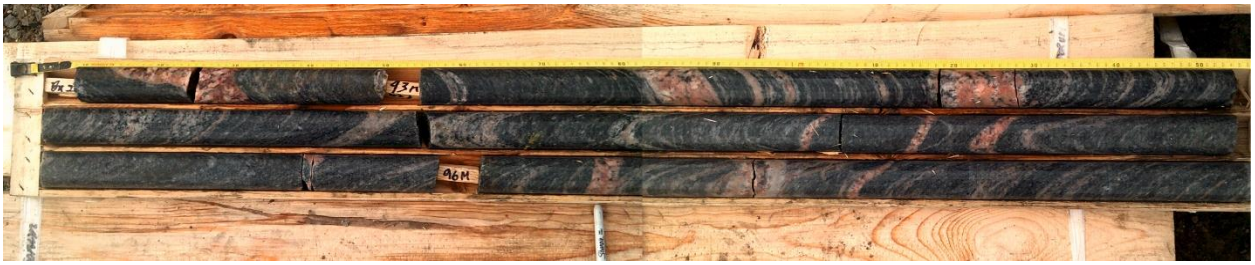

Figure A2.24. Core box #24 – drilling depth 93 m and 96 m.

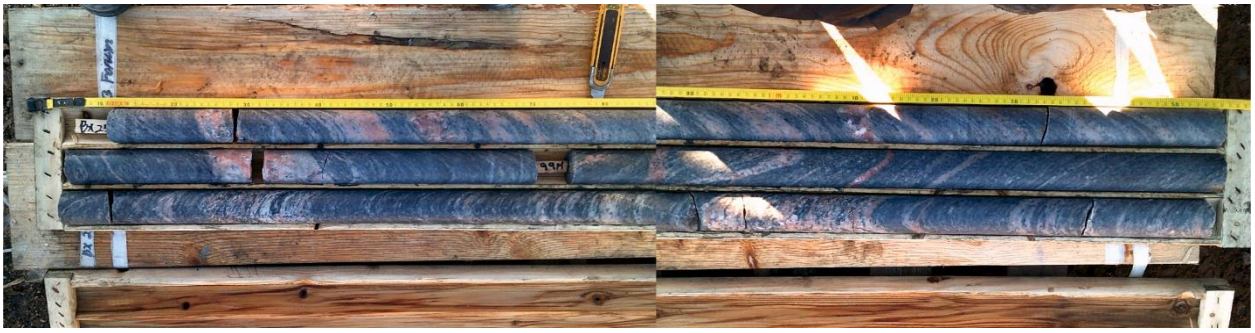

Figure A2.25. Core box #25 – drilling depth 99 m.

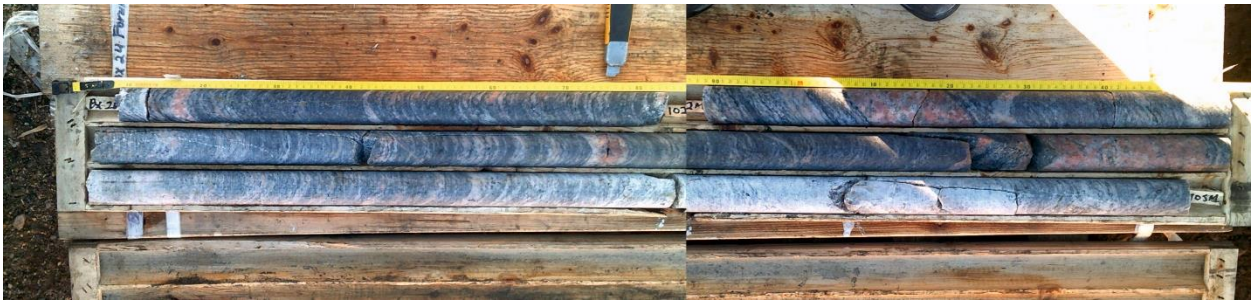

Figure A2.26. Core box #26 – drilling depth 102 m and 105 m.

Figure A2.27. Core box #27 – drilling depth 108 m.

Figure A2.28. Core box #28 – drilling depth 111 m and 114 m.

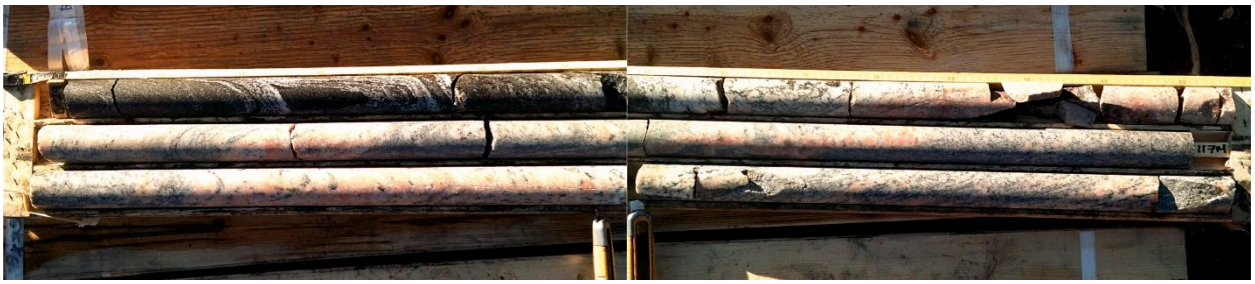

Figure A2.29. Core box #29 – drilling depth 117 m.

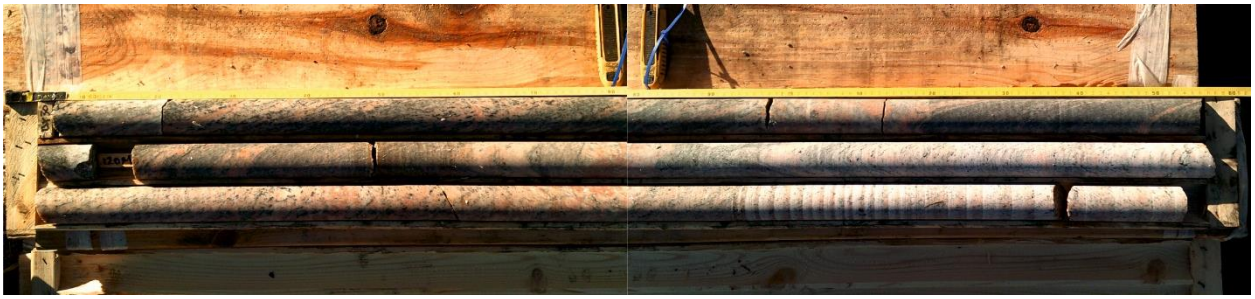

Figure A2.30. Core box #30 – drilling depth 120 m.

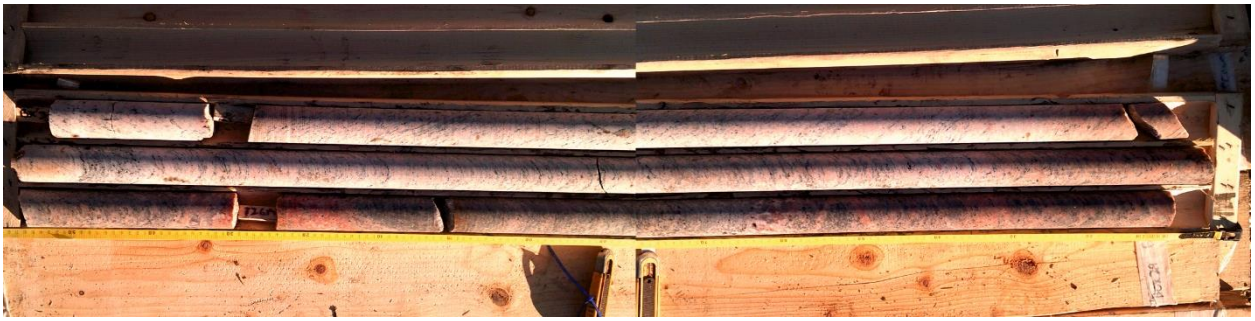

Figure A2.31. Core box #31 – drilling depth 123 m and 126 m.

Figure A2.32. Core box #32 – drilling depth 129 m.

Figure A2.33. Core box #33 – drilling depth 132 m and 135 m.

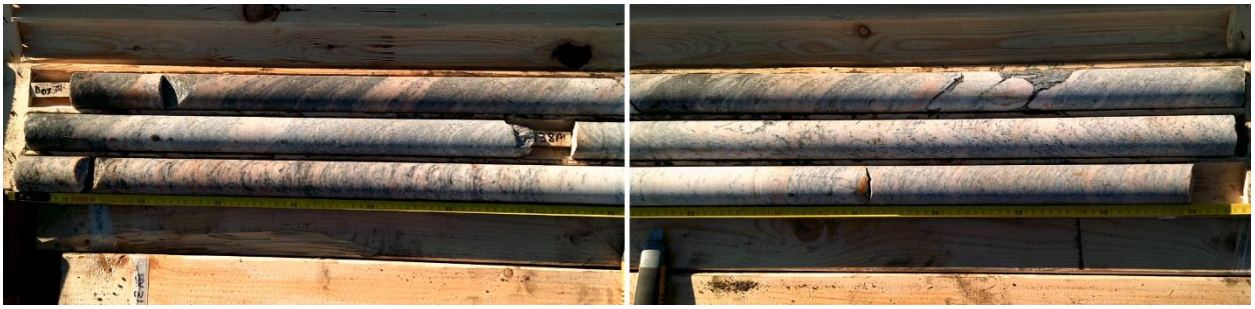

Figure A2.34. Core box #34 – drilling depth 138 m.

Figure A2.35. Core box #35 – drilling depth 141 m and 144 m.

Figure A2.36. Core box #36 – drilling depth 147 m.

Figure A2.37. Core box #37 – drilling depth 150 m.

Figure A2.38. Core box #38 – drilling depth 153 m and 156 m.

Figure A2.39. Core box #39 – drilling depth 159 m.

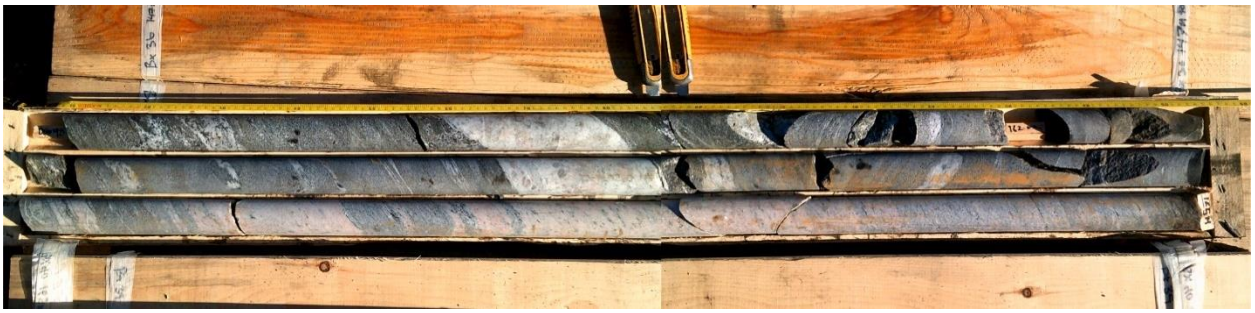

Figure A2.40. Core box #40 – drilling depth 162 m and 165 m.

Figure A2.41. Core box #41 – drilling depth 168 m.

Figure A2.42. Core box #42 – drilling depth 171 m.

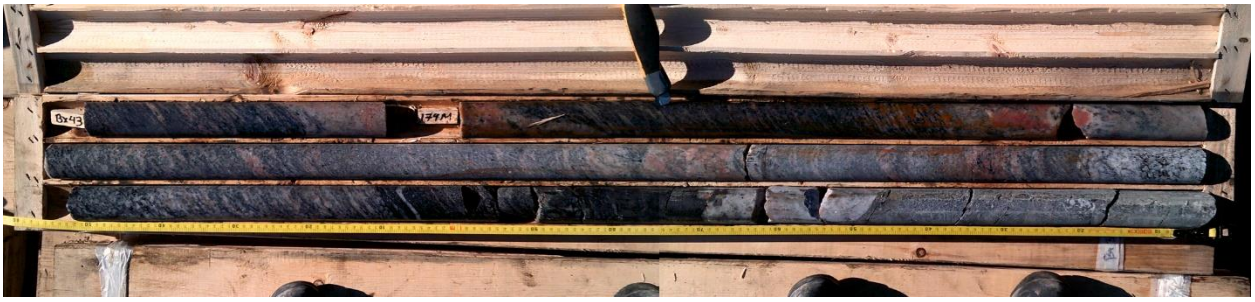

Figure A2.43. Core box #43 – drilling depth 174 m and 177 m.

Figure A2.44. Core box #44 – drilling depth 180 m.

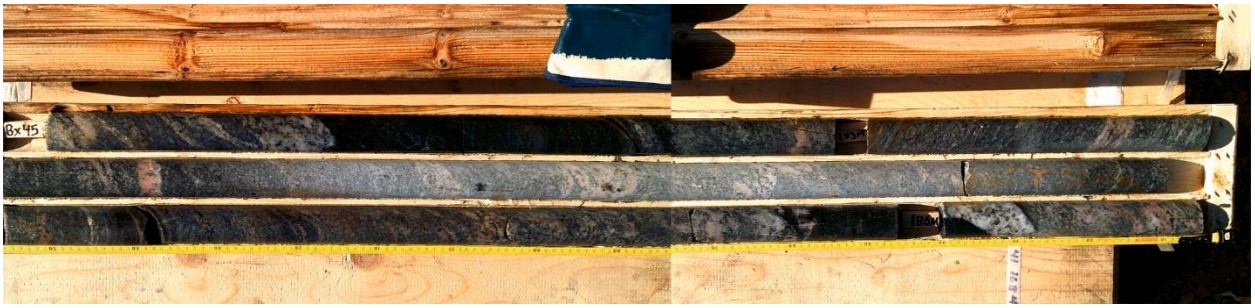

Figure A2.45. Core box #45 – drilling depth 183 m and 186 m.

Figure A2.46. Core box #46 – drilling depth 189 m.

Figure A2.47. Core box #47 – drilling depth 192 m and 195 m.

Figure A2.48. Core box #48 – drilling depth 198 m.

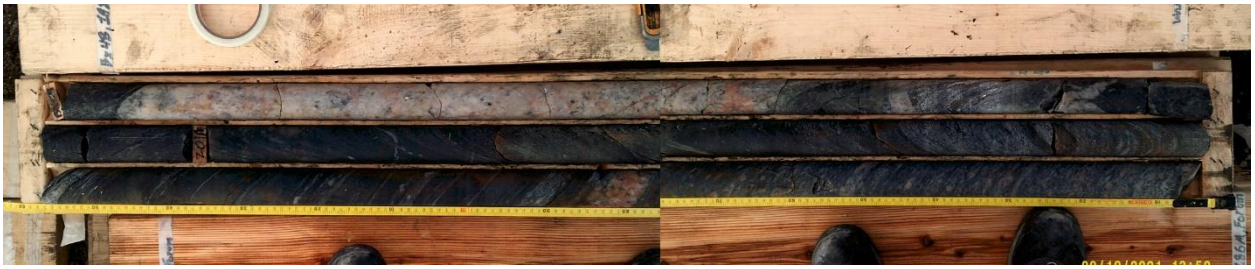

Figure A2.49. Core box #49 – drilling depth 201 m.

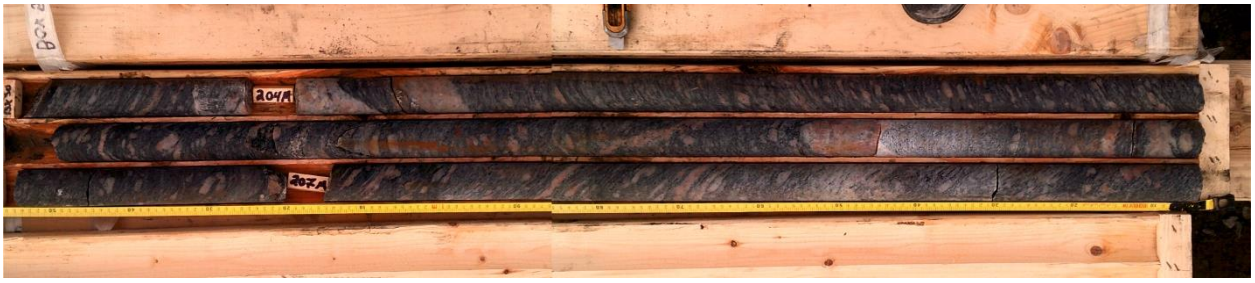

Figure A2.50. Core box #50 – drilling depth 204 m and 207 m.

Figure A2.51. Core box #51 – drilling depth 210 m.

Figure A2.52. Core box #52 – drilling depth 213 m and 216 m.

Figure A2.53. Core box #53 – drilling depth 219 m.

Figure A2.54. Core box #54 – drilling depth 222 m and 225 m.

Figure A2.55. Core box #55 – drilling depth 228 m.

Figure A2.56. Core box #56 – drilling depth 231 m and 234 m.

APPENDIX III – PARAGNEISS

Figure A3.1. Sample F6 - Paragneiss sample from 6 m depth – Core box #1.

Figure A3.2. Sample F27 – Paragneiss sample from 26.51 m depth – Core box #9.

Figure A3.3. Sample F27 – Paragneiss sample from 27 m depth – Core box #9.

Figure A3.4. Sample F30 – Paragneiss sample from 30 m depth with the contact with a pink pegmatitic granitic intrusion (probably Dancelou Suite) – Core box #10.

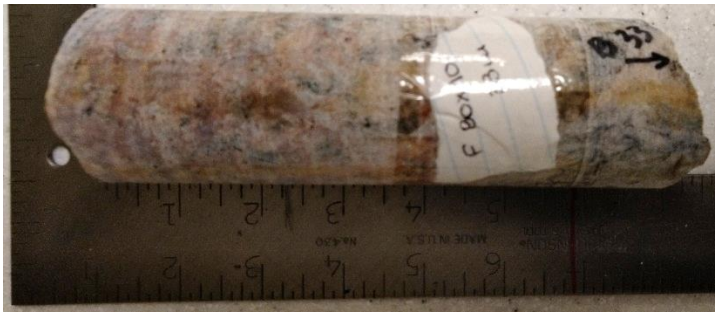

Figure A3.5. Sample F33 – Paragneiss sample from 33 m depth – core box #10.

Figure A3.6. Sample F33 – Paragneiss sample from 33 m depth – Core box #10.

Figure A3.7. Sample F36 – Paragneiss sample from 36.62 m depth – Core box #11.

Figure A3.8. Sample F45 – Paragneiss sample from 45 m depth – Core box #13.

Figure A3.9. Sample F48 - Paragneiss sample from 46.35 m depth – Core box #14.

Figure A3.10. Sample F57 - Paragneiss sample from 57 m depth – Core box #15.

Figure A3.11. Sample F60 – Paragneiss sample from 60 m depth – Core box #16.

Figure A3.12. Sample F60 - Paragneiss sample from 60 m depth – Core box #16.

Figure A3.13. Sample F63 - Paragneiss sample from 63 m depth – Core box #17.

Figure A3.14. Sample F66 - Paragneiss sample from 66 m depth – Core box #17.

Figure A3.15. Sample F69 - Paragneiss sample from 69 m depth – Core box #18.

Figure A3.16. Sample F72 - Paragneiss sample from 72 m depth – Core box #19.

Figure A3.17. Sample F72 - Paragneiss sample from 72 m depth – Core box #19.

Figure A3.18. Sample F75 - Paragneiss sample from 75 m depth – Core box #19.

Figure A3.19. Sample F78 – Paragneiss sample from 78 m depth – Core box #20.

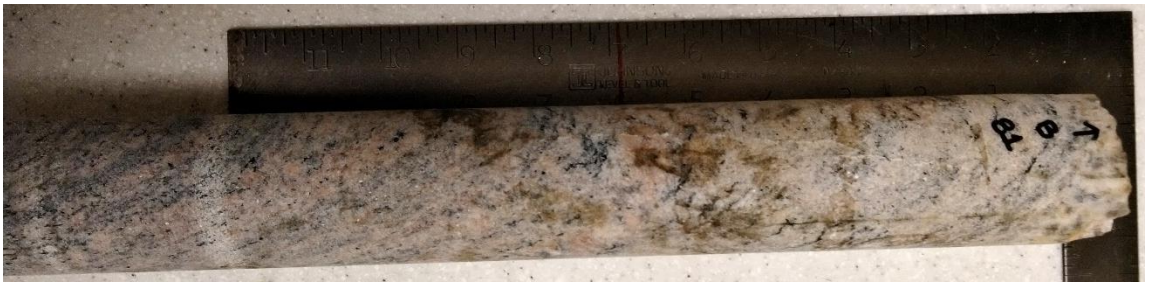

Figure A3.20. Sample F81 – Paragneiss sample from 81 m depth – Core box #21.

Figure A3.21. Sample F84 – Paragneiss sample from 84 m depth – Core box #21.

Figure A3.22. Sample F87 – Paragneiss sample from 87 m depth – Core box #22.

Figure A3.23. Sample F93 – Paragneiss sample from 93 m depth with contact with a pink pegmatitic granitic intrusion (probably Dancelou Suite) – Core box #24.

Figure A3.24. Sample F96 – Paragneiss sample from 96 m depth – Core box #24.

Figure A3.25. Sample F99 – Paragneiss sample from 99 m depth – Core box #25.

Figure A3.26. Sample F102 – Paragneiss sample from 102 m depth – Core box #26

Figure A3.27. Sample F105 – Paragneiss sample from 105 m depth – Core box #26.

Figure A3.28. Sample F108 – Paragneiss sample from 108 m depth – Core box #27.

Figure A3.29. Sample F111 – Paragneiss sample from 111 m depth – Core box #28.

Figure A3.30. Sample F117 – Paragneiss sample from 115.55 m depth – Core box #29.

Figure A3.31. Sample F120 – Paragneiss sample from 120 m depth – Core box #30.

Figure A3.32. Sample F123 – Paragneiss sample from 123 m depth – Core box #31.

Figure A3.33. Sample F126 – Paragneiss sample from 126 m depth with contact with a pink pegmatitic granitic intrusion (probably Dancelou Suite) – Core box #31.

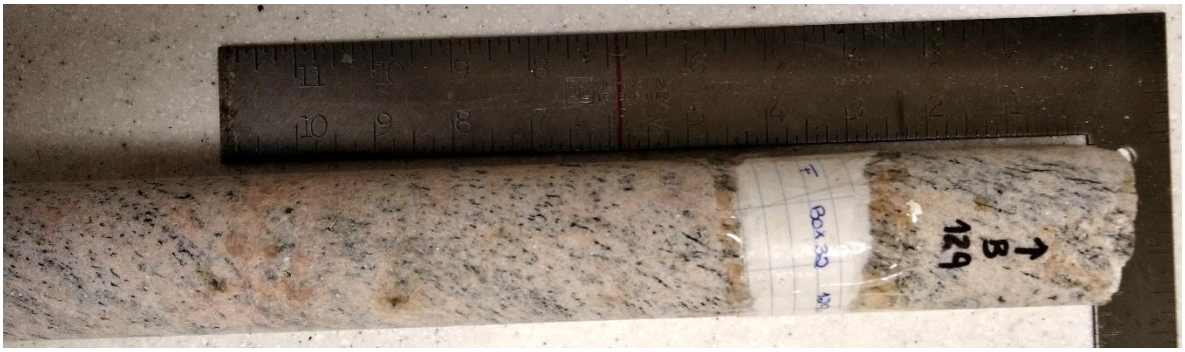

Figure A3.34. Sample F129 – Paragneiss sample from 129 m depth – Core box #32.

Figure A3.35. Sample F132 – Paragneiss sample from 132 m depth – Core box #33.

Figure A3.36. Sample F132 – Paragneiss sample from 132 m depth – Core box #33.

Figure A3.37. Sample F135 – Paragneiss sample from 135 m depth – Core box #33.

Figure A3.38. Sample F138 – Paragneiss sample from 138 m depth – Core box #34.

Figure A3.39. Sample F141 – Paragneiss sample from 141 m depth – Core box #35.

Figure A3.40. Sample F144 – Paragneiss sample from 144 m depth – Core box #35.

Figure A3.41. Sample F147 – Paragneiss sample from 147 m depth – Core box #36.

Figure A3.42. Sample F 150 – Paragneiss sample from 150 m depth – Core box #37.

Figure A3.43. Sample F153 – Paragneiss sample from 153 m depth with contact with a pink pegmatitic granitic intrusion (probably Dancelou Suite) – Core box #38.

Figure A3.44. Sample F165 – Paragneiss sample from 165 m depth – Core box #40.

Figure A3.45. Sample F171 – Paragneiss sample from 171 m depth – Core box #42.

Figure A3.46. Sample F174 – Paragneiss sample from 174 m depth with contact with a tonalitic/granitic intrusion (probably Aveneau or Dancelou suites) – Core box #43.

Figure A3.47. Sample F177 – Paragneiss sample from 177 m depth in contact with diorite (probably Kaslac Complex or Ralleau Suite) – Core box #43.

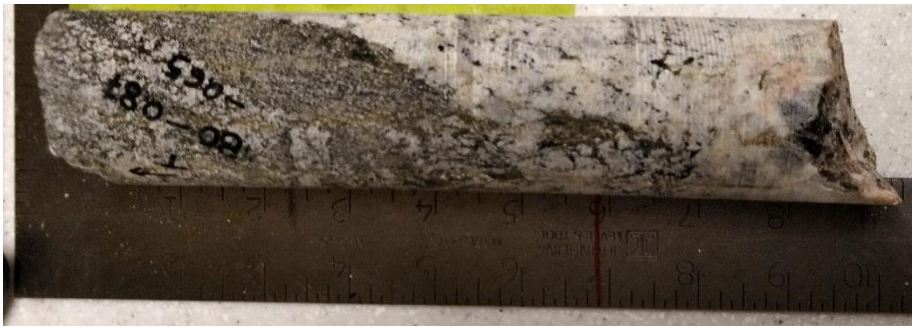

Figure A3.48. Sample F180 – Paragneiss sample from 178.48 m depth in contact with diorite (probably Kaslac Complex or Ralleau Suite) – Core box #44.

Figure A3.49. Sample F180 – Paragneiss sample from 180 m depth – Core box #44.

Figure A3.50. Sample F183 – Paragneiss sample from 183 m depth – Core box #45.

Figure A3.51. Sample F186 – Paragneiss sample from 186 m depth in contact with diorite (probably Kaslac Complex or Ralleau Suite) – Core box #45.

Figure A3.52. Sample F189 – Paragneiss sample from 189 m depth – Core box #46.

Figure A3.53. Sample F192 – Paragneiss sample from 192 m depth – Core box #47.

Figure A3.54. Sample F204 – Paragneiss sample from 204 m depth – Core box #50.

Figure A3.55. Sample F207 – Paragneiss sample from 207 m depth – Core box #50.

Figure A3.56. Sample F210 – Paragneiss sample from 210 m depth – Core box #51.

Figure A3.57. Sample F213 – Paragneiss sample from 213 m depth – Core box #52.

Figure A3.58. Sample F216 – Paragneiss sample from 216 m depth with contact with a pink pegmatitic granitic intrusion (probably Dancelou Suite) – Core box #52.

Figure A3.59. Sample F225 – Paragneiss sample from 225 m depth – Core box #54.

Figure A3.60. Sample F231 – Paragneiss sample from 231 m depth – Core box #56.

Figure A3.61. Sample F234 – Paragneiss sample from 233.85 m depth – Core box #56.

APPENDIX IV – DIORITE/GABBRO

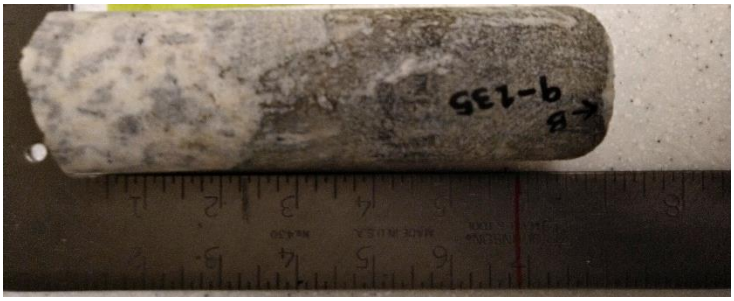

Figure A4.1. Sample F9 - Diorite sample from 7.65 m depth in contact with a tonalitic/granitic intrusion (probably Aveneau/Dancelou suites or Kaslac Complex subunit quartz-rich granitoid) – Core box #2.

Figure A4.2. Sample F12 - Gabbro sample from 12 m depth with garnet clusters – Core box #4.

Figure A4.3. Sample F15 – Gabbro sample from 15 m depth – Core box #5.

Figure A4.4. Sample F18 – Diorite sample from 18 m depth in contact with a tonalitic/granitic intrusion (probably Aveneau/Dancelou suites or Kaslac Complex subunit quartz-rich granitoid) – Core box #6.

Figure A4.5. Sample F18 - Diorite sample from 19.16 m depth – Core box #6.

Figure A4.6. Sample F21 – Diorite sample from 21 m depth – Core box #7.

Figure A4.7. Sample F42 – Gabbro sample from 40.55 m depth with garnet clusters – Core box #12.

Figure A4.8. Sample F45 - Diorite sample from 41.89 m depth with garnet clusters – Core box #13.

Figure A4.9. Sample F48 - Diorite sample from 48 m depth – Core box #14.

Figure A4.10. Sample F48 – Gabbro sample from 50.76 m depth with garnet clusters – Core box #14.

Figure A4.11. Sample F54 - Gabbro sample from 54 m depth with garnet clusters – Core box #15.

Figure A4.12. Sample F90 - Diorite sample from 90 m depth – Core box #23.

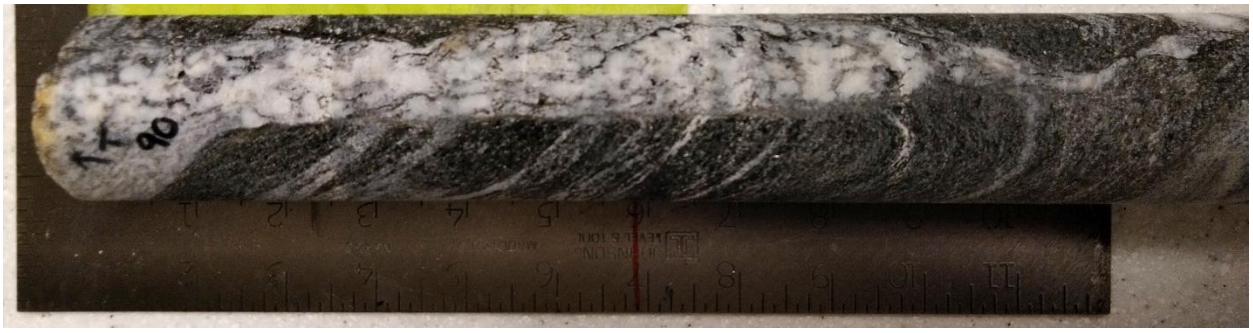

Figure A4.13. Sample F90 - Diorite sample from 90 m depth – Core box #23.

Figure A4.14. Sample F114 - Diorite sample from 114 m depth – Core box #28.

Figure A4.15. Sample F117 - Diorite sample from 114.88 m depth – Core box #29.

Figure A4.16. Sample F156 - Diorite sample from 156 m depth – Core box #38.

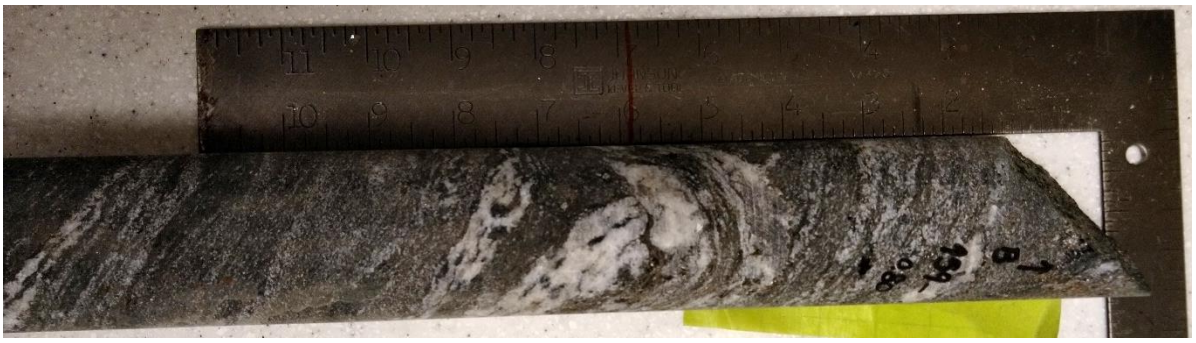

Figure A4.17. Sample F159 - Diorite sample from 158.20 m depth – Core box #39.

Figure A4.18. Sample F162 - Diorite sample from 162 m depth – Core box #40.

Figure A4.19. Sample F168 - Diorite sample from 168 m depth – Core box #41.

Figure A4.20. Sample F177 - Diorite sample from 177 m depth in contact with paragneiss (False Suite) – Core box #43.

Figure A4.21. Sample F180 - Diorite sample from 178.48 m depth in contact with paragneiss (False Suite) - Core box #44.

Figure A4.22. Sample F180 – Gabbro sample from 179.13 m depth – Core box #44.

Figure A4.23. Sample F186 - Diorite sample from 186 m depth in contact with paragneiss (False Suite) – Core box #45.

Figure A4.24. Sample F195 - Diorite sample from 195 m depth – Core box #47.

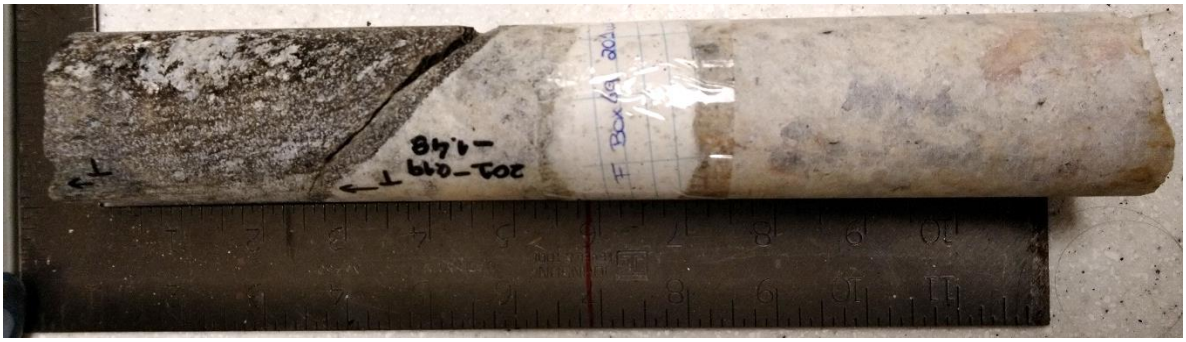

Figure A4.25. Sample 201 - Diorite sample from 199.33 m depth in contact with tonalitic/granitic intrusion – Core box #49.

Figure A4.26. Sample F201 – Diorite sample from 201 m depth – Core box #49.

Figure A4.27. Sample F219 - Diorite sample from 219 m depth with tonalitic/granitic intrusion – Core box #53.

Figure A4.28. Sample F222 - Diorite sample from 222 m depth – Core box #54.

Figure A4.29. Sample F228 - Diorite sample from 226 m depth – Core box #55.

APPENDIX V – TONALITE/GRANITE/GRANITOIDS

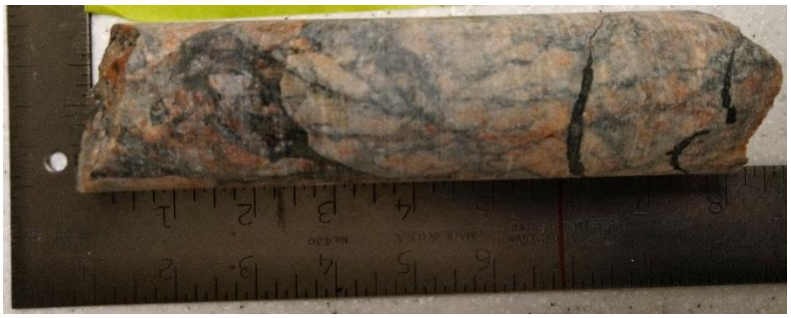

Figure A5.1. Sample F12 - Granitoid sample from 10.41 m depth – Core box #4.

Figure A5.2. Sample F21 - Granitoid sample from 20.20 m depth – Core box #7.

Figure A5.3. Sample F24 – Granitoid sample from 23.75 m depth – Core box #8.

Figure A5.4. Sample F24 - Granitoid sample from 24 m depth – Core box #8.

Figure A5.5. Sample F39 - Granitoid sample from 39 m depth – Core box #12.

Figure A5.6. Sample F42 - Granitoid sample from 40.54 m depth – Core box #12.

Figure A5.7. Sample F81 - Granitoid sample from 81 m depth – Core box #21.

Figure A5.8. Sample F117 - Granitoid sample from 115.08 m depth – Core box #29.

Figure A5.9. Sample F198 - Granitoid sample from 198 m depth – Core box #48.

Figure A5.10. Sample F222 - Granitoid sample from 222 m depth – Core box #54.

APPENDIX VI – THERMAL CONDUCTIVITY

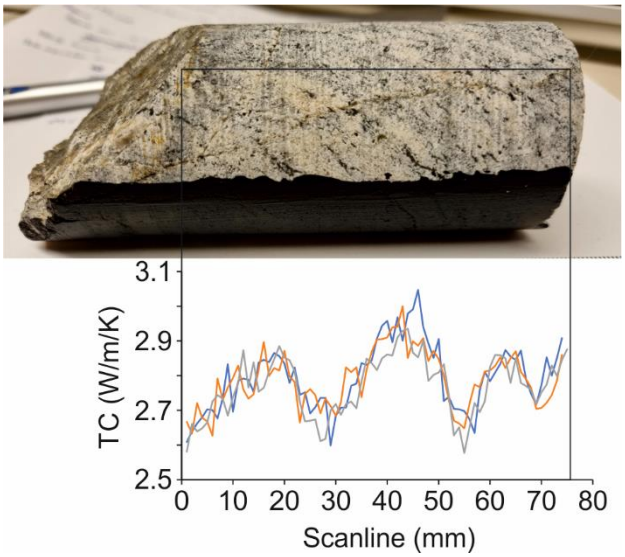

Figure A6.1. Thermal conductivity profile obtained for sample F6. The three profiles are related with the three scans carried out.

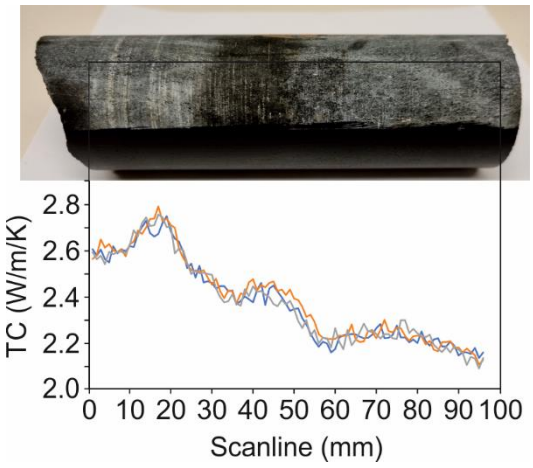

Figure A6.2. Thermal conductivity profile obtained for sample F12. The three profiles are related with the three scans carried out.

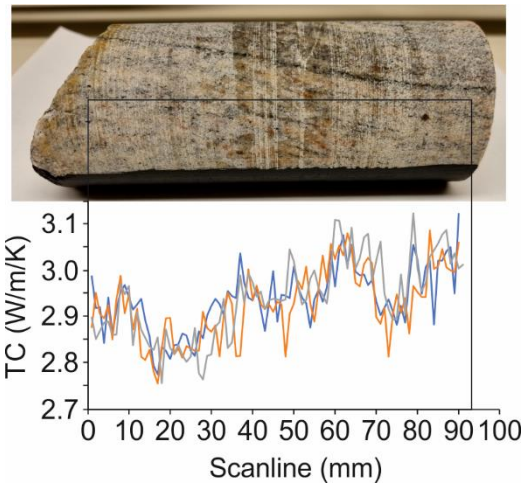

Figure A6.3. Thermal conductivity profile obtained for sample F33. The three profiles are related with the three scans carried out.

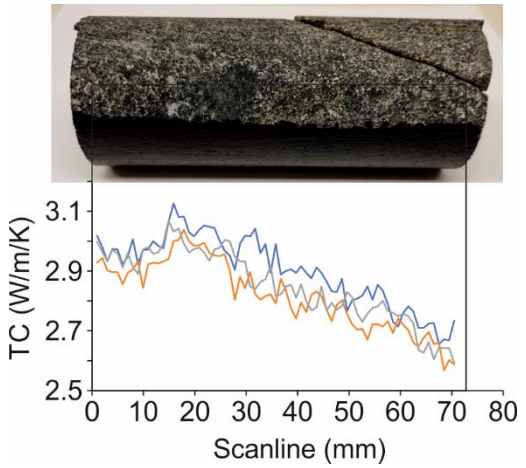

Figure A6.4. Thermal conductivity profile obtained for sample F42. The three profiles are related with the three scans carried out. The decrease in the thermal conductivity values on the last part of the profile is related with a probable natural fracture that broke during sample preparation.

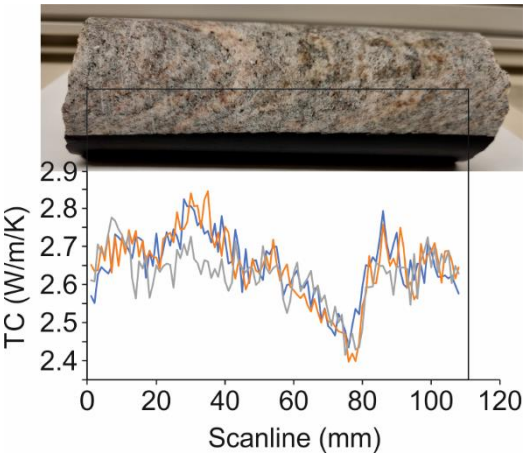

Figure A6.5. Thermal conductivity profile obtained for sample F48. The three profiles are related with the three scans carried out.

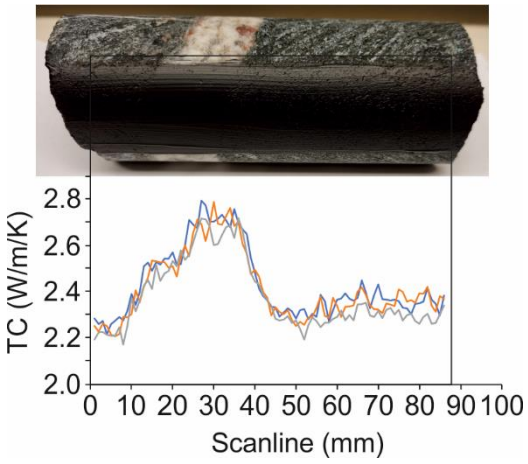

Figure A6.6. Thermal conductivity profile obtained for sample F54. The three profiles are related with the three scans carried out. The presence of the centimetric quartz band is clearly identified in the thermal conductivity profile.

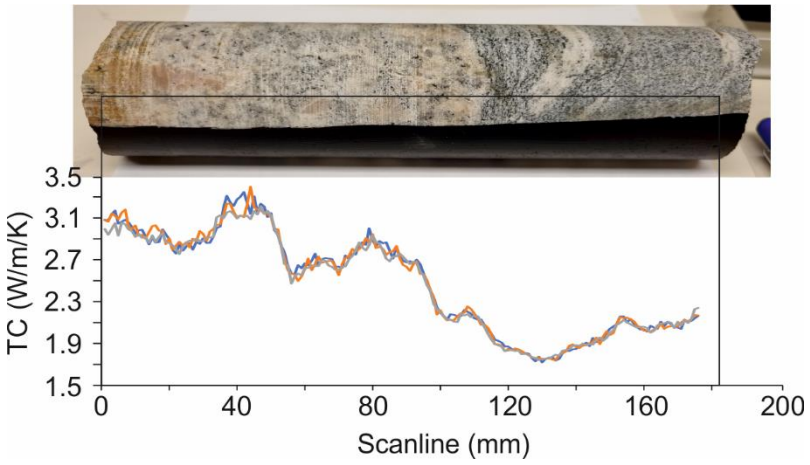

Figure A6.7. Thermal conductivity profile obtained for sample F108. The three profiles are related with the three scans carried out. The presence of a quartz- and a mafic-rich zones are clearly identified in the thermal conductivity profile.

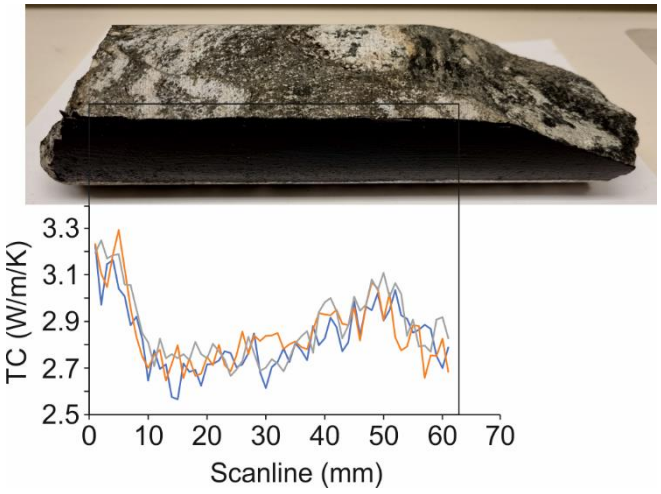

Figure A6.8. Thermal conductivity profile obtained for sample F117. The three profiles are related with the three scans carried out. The protomylonitic texture is clearly identified in the thermal conductivity profile.

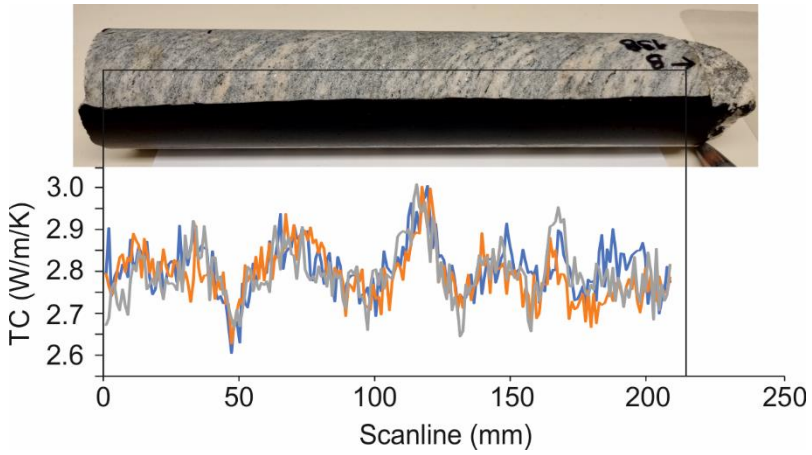

Figure A6.9. Thermal conductivity profile obtained for sample F138. The three profiles are related with the three scans carried out.

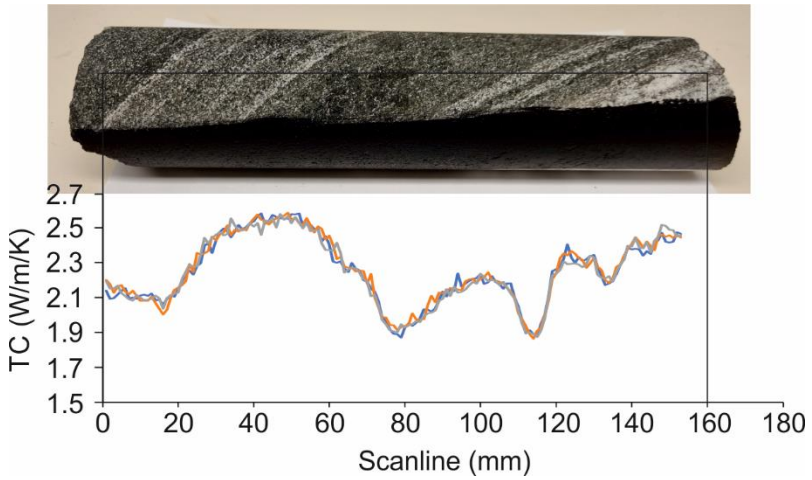

Figure A6.10. Thermal conductivity profile obtained for sample F156. The three profiles are related with the three scans carried out. The protomylonitic texture is clearly identified in the thermal conductivity profile.

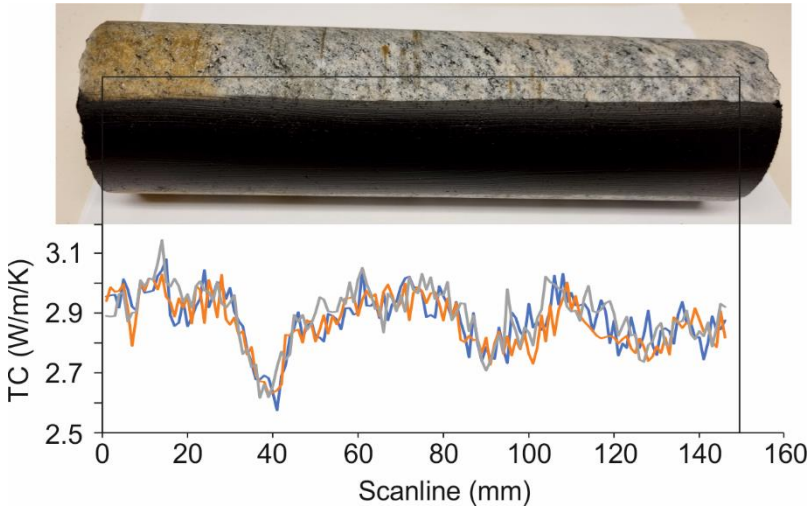

Figure A6.11. Thermal conductivity profile obtained for sample F183. The three profiles are related with the three scans carried out.

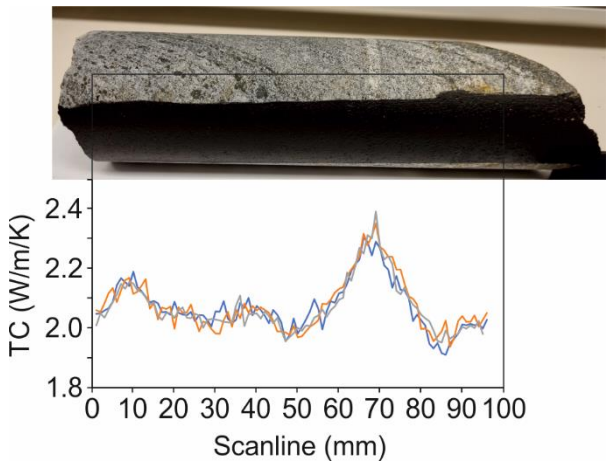

Figure A6.12. Thermal conductivity profile obtained for sample F201. The three profiles are related with the three scans carried out.

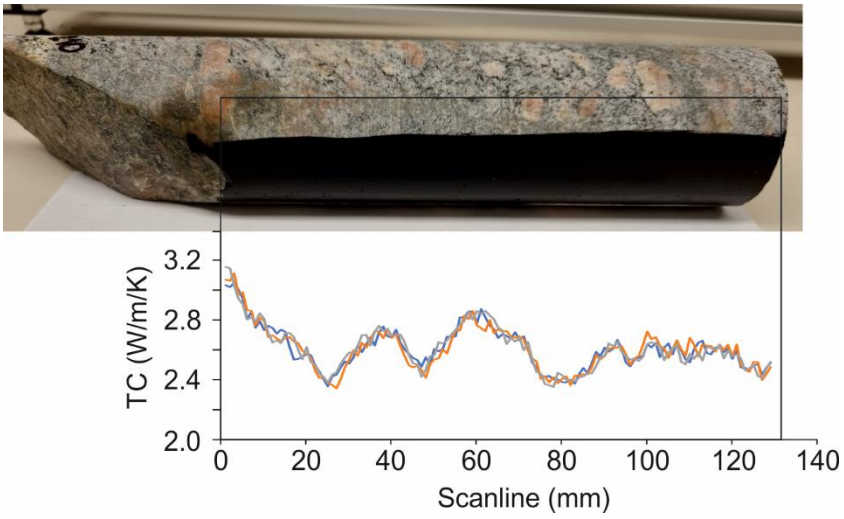

Figure A6.13. Thermal conductivity profile obtained for sample F210. The three profiles are related with the three scans carried out.

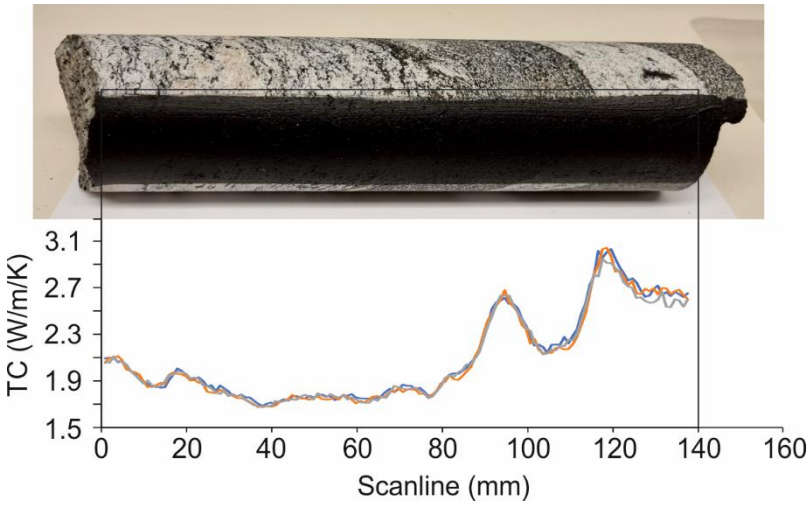

Figure A6.14. Thermal conductivity profile obtained for sample F228. The three profiles are related with the three scans carried out.

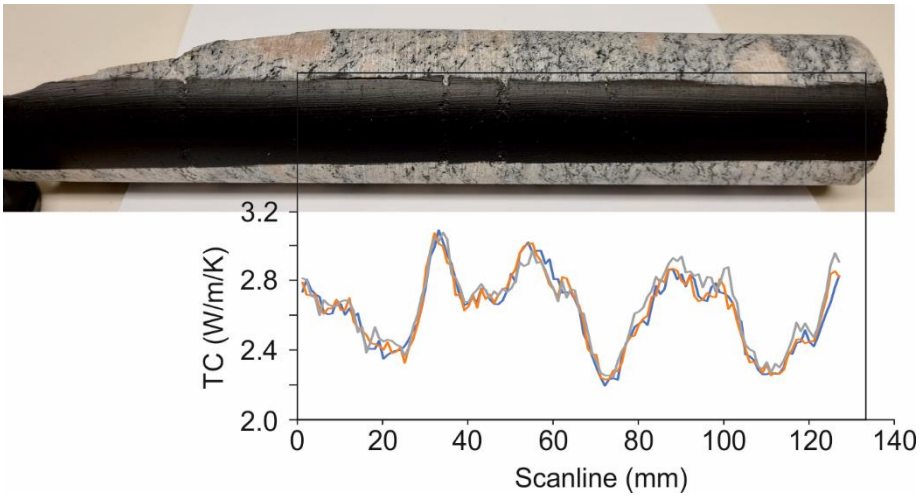

Figure A6.15. Thermal conductivity profile obtained for sample F234. The three profiles are related with the three scans carried out.